INVESTIGATION OF ANISOTROPIC TRANSVERSE RESONANCE IN THE DESIGN OF LOW PROFILE WIDEBAND ANTENNAS

by Gregory A. Mitchell

B.S. in Electrical Engineering, May 2005, University of Maryland College Park
M.S. in Electrical Engineering, December 2008, The Johns Hopkins University

A Dissertation submitted to

The Faculty of

The School of Engineering and Applied Sciences of
The George Washington University in partial satisfaction of
the requirement for the degree of Doctor of Philosophy

August 31, 2015

Dissertation directed by
Wasyl Wasylkiwskyj
Professor of Engineering and Applied Science

The School of Engineering and Applied Science of the George Washington University certifies that Gregory Mitchell has passed the Final Examination for the degree of Doctor of Philosophy as of April 16, 2015. This is the final and approved form of the dissertation.

Investigation of Anisotropic Transverse Resonance in the Design of Low Profile Wideband Antennas

Gregory A. Mitchell

Dissertation Research Committee:

Wasyl Wasykiwskyj, Professor of Electrical Engineering, Dissertation Director

Roger Lang, Professor of Electrical Engineering, Committee Member

Mona Zaghloul, Professor of Electrical Engineering, Committee Member

Abstract

Investigation of Anisotropic Transverse Resonance in the Design of Low Profile Wideband Antennas

We analyze the properties of anisotropic media as a means to reduce the cavity profile of an antenna at low UHF. Many applications in wireless communications and radar require antennas that conform to the surface of a supporting structure. Low profile antennas (LPA) are of special importance within the ultra-high frequency (UHF) band where they are used as communications antennas on military platforms.

We investigate a flush mounted rectangular cavity with a $\lambda_o/2$ aperture opening. We feed the antenna by a two-port matching network fed 180° out of phase at the inputs. The backshort defines the cavity profile, and should be as small as possible. Our approach loads the cavity with a high index, anisotropic medium to realize a reduction in profile by reducing the distance from the backshort and the matching network.

We derive an anisotropic transverse resonance for the design of a novel cavity geometry which maintains a constant resonance frequency in the face of high index anisotropic media. The final design produces a radiating rectangular cavity partially loaded with a magnetic uniaxial anisotropic medium. This design achieves a 1.2 octave bandwidth and a realized gain ranging from 3.5 dB – 8.2 dB with a profile of only $0.04\lambda_o$. The non-tapered anisotropic LPA outperforms other state of the art designs in terms of bandwidth and realized gain. Furthermore, it performs on par with a typical air-filled radiating cavity in terms of impedance match and realized gain, but with a 71.4% reduction in profile.

Table of Contents

Abstract iii

List of Figures vi

List of Tables xiv

List of Acronyms xv

Chapter 1. Introduction 1
1.1 Thesis Contributions 4

Chapter 2. Review of Prior Art 11
2.1 Coaxial Line to Waveguide Transition (CWT) 11
2.2 Propagation in Anisotropic Media 12
2.3 Review of Low Profile Wideband Antennas 15

Chapter 3. Radiating Rectangular Cavities 22
3.1 Semi-infinite Rectangular Waveguide 22
3.2 Air Filled Cavity Stimulated by a Flat Probe (FLPA) 28
3.3 Cavity Loaded with High Index Dielectric 37

Chapter 4. Low Profile Antenna (LPA) Design Incorporating an Isotropic Transverse Resonance Formulation 41
4.1 Isotropic Transverse Resonance of a Partially Loaded Parallel Plate Waveguide 41
4.2 Isotropic Tapered Cavity Design 48
4.3 LPA Design: Dielectric Medium ($\varepsilon_r = 10.2$) 41
4.4 Comparison of Isotropic LPA Designs to FLPA, and State of the Art 57

Chapter 5. LPA Design Incorporating an Anisotropic Transverse Resonance Formulation 61
5.1 Measured Parameters of the Anisotropic Permeability Tensors 61
5.1.1 *Validation of Measured Parameters via Simulation and Measurement* 63
5.2 Anisotropic Transverse Resonance of a Partially Loaded Parallel Plate Waveguide 68
5.2.1 *Electric and Magnetic Fields in the Free Space Region* 68
5.2.2 *Electric and Magnetic Fields in the Anisotropic Medium* 70
5.2.3 *Solving for the Characteristic Impedances of the Two Regions* 72
5.2.4 *Solving for the Transverse Resonance Condition* 74
5.3 Tapered LPA Design: Anisotropic Ferrite ($\mu_x = \mu_z = 15$) 77
5.4 Non-Tapered LPA Design: Anisotropic Ferrite ($\varepsilon_y = \mu_z = 1$, $\mu_x = 15$) 84
5.4.1 *Scaling the Design in Frequency* 88

5.4.2 *Introduction of Losses to the Model* 91
5.5 Comparison of Non-tapered Anisotropic LPA Designs to Isotropic LPA, FLPA and State of the Art 94

Chapter 6. Conclusions 99
6.1 Recommendations for Future Research 100

References 102

Appendix A. Anisotropic Magnetic Metamaterials 107
A.1 Advantages of Anisotropic Metamaterials 107
A.2 Description of the Manufacturing Process 108
A.3 Measured Parameters of Anisotropic P4 Metaferrite 109
A.4 Electromagnetic Models of P4 Metaferrite 114
A.4.1 *Model Verification* 116

Appendix B. Numerical Case Study of Linearly Tapered Low Profile Cavities 122
B.1 Definition of the Linearly Tapered Cavity Model 122
B.2 Linearly Tapered Cavity Partially Loaded with Isotropic Material 124
B.3 Linearly Tapered Cavity Partially Loaded with Anisotropic Material 127
B.4 Further Reduction of Cavity Profile 132
B.5 Reduction of Flange Size 134
B.6 Effect of Probe Dimensions on the Return Loss 136

Appendix C. Plane Wave Propagation in an Anisotropic Medium 139
C.1 Anisotropic Wave Equation 139
C.2 Dispersion Equation for H_z 142
C.3 Dispersion Equation for E_z 144
C.4 Suppression of Birefringence 145

Appendix D. Modal Decomposition Matrix for Determining the Fourier Transform of the Fields at the Aperture of a Radiating Semi-infinite Waveguide 149
D.1 Modal Decomposition of a Rectangular Waveguide 149
D.1.1 *Incident TE_{10} Mode* 150
D.2 Formulation of the MDM Method 156
D.2.1 *Derivation of the MDM Equation* 156
D.2.2 *Representation of k_x and k_y when $z \geq 0+$* 159
D.3 Calculation of Far Field and Comparison to Simulation 162
D.3.1 *Description of CST Model* 162
D.3.2 *Analysis* 164

Appendix E. Description of Simulation Details for CST Models in this Dissertation 168
E.1 Port Excitations 168
E.2 Mesh Cell Resolution and Symmetry Planes 170

List of Figures

Figure 1.1: Flush mounted radiating rectangular cavity 2

Figure 1.2: To-scale diagram of the antenna profile in both the transverse (x,y) and the normal (x,z) planes. (a) FLPA. (b) Radiating waveguide. 6

Figure 1.3: To-scale diagrams of the antenna profiles in the normal (x,z) plane. (a) FLPA. (b) Isotropic dielectric LPA. (c) Isotropic dielectric LPA. (d) Anisotropic LPA. 7

Figure 2.1: Geometry of a traditional CWT. 12

Figure 2.2: Design of the spiral antenna. Top view of the assembled antenna (left). Top view of the cavity (right). 16

Figure 2.3: Prototype of the inverted L antenna. 16

Figure 2.4: Three dimensional layered slotted bowtie. 17

Figure 2.5: Cavity backed discone antenna. 18

Figure 2.6: Monopole antenna above a HIS substrate. 19

Figure 2.7: Bowtie above the HIS structure. 19

Figure 2.8: Dipole antenna above the EBG patch. 20

Figure 3.1: Transverse (x,y) plane of a waveguide aperture surrounded by an infinite flange. 23

Figure 3.2: CST model of the waveguide excited by a matched waveguide port. 24

Figure 3.3: The cosine TE_{10} mode electric field distribution in the waveguide. 25

Figure 3.4: Polar plot of the normalized far field E_θ and E_ϕ radiation patterns. 27

Figure 3.5: Linear plot of the normalized far field E_θ and E_ϕ radiation patterns. 28

Figure 3.6: Geometry of a radiating waveguide based on Wade's CWT. 29

Figure 3.7: VSWR of a radiating waveguide with λ_o = 1.94 m. 30

Figure 3.8: Return loss of a radiating waveguide with λ_o = 1.94 m. 31

Figure 3.9: Realized gain of a radiating waveguide with λ_o = 1.94 m. 31

Figure 3.10: Radiation pattern at 280 MHz of the radiating waveguide with λ_o = 1.94 m. 32

Figure 3.11: To-scale diagram of the antenna profile in the normal direction. (a) FLPA. (b) Radiating waveguide 33

Figure 3.12: CST model of FLPA design with λ_o = 1.56 m. 34

Figure 3.13: VSWR of the radiating waveguide and the FLPA. 35

Figure 3.14: Return loss of the radiating waveguide and the FLPA. 35

Figure 3.15: Realized gain of the radiating waveguide and the FLPA. 36

Figure 3.16: Polar plots of the far field radiation patterns of the FLPA. (a) 200 MHz. (b) 359 MHz. (c) 500 MHz. 36

Figure 3.17: The geometry of the FLPA backshort loaded with a high index medium. 38

Figure 3.18: CST model of loaded FLPA. 38

Figure 3.19: VSWR of the loaded FLPA. 39

Figure 3.20: Realized gain of the loaded FLPA 40

Figure 4.1: Top view and side view of a symmetrically loaded, tapered radiating rectangular cavity. 42

Figure 4.2: Shorted transmission line model of a symmetrically loaded rectangular cavity. 43

Figure 4.3: Transformed transmission line model of figure 4.2. 45

Figure 4.4: Normalized L_g/λ_o vs. w/λ_o curves for different ratios of μ_r/ε_r. 47

Figure 4.5: Top view and side view of the geometry of the tapered cavity design when $\mu_r/\varepsilon_r > 1$. 49

Figure 4.6: Top view and side view of the geometry of the tapered cavity design when $\mu_r/\varepsilon_r < 1$. 49

Figure 4.7: Top view and side view of the geometry of the tapered cavity design when $\mu_r/\varepsilon_r = 1$. 50

Figure 4.8: (a) The fringing fields produced by an asymmetric single probe feed. (b) The continuous current path of a symmetric dual probe feed. 50

Figure 4.9: The CST model of the tapered isotropic dielectric LPA design when $\mu_r/\varepsilon_r = 0.098$. 52

Figure 4.10: VSWR of the tapered dielectric LPA and the loaded FLPA. 52

Figure 4.11: Return Loss of the tapered dielectric LPA and the loaded FLPA. 50

Figure 4.12: Realized gain of the tapered dielectric LPA and the loaded FLPA. 53

Figure 4.13: Radiation patterns of the tapered dielectric. (a) 285 MHz. (b) 350 MHz. (c) 435 MHz. 53

Figure 4.14: Far field directivity patterns of the tapered dielectric LPA at 400 MHz. (a) Fed in phase. (b) Fed 180° out of phase. 54

Figure 4.15: Far field directivity patterns of the tapered dielectric LPA at 440 MHz. (a) Fed in phase. (b) Fed 180° out of phase. 55

Figure 4.16: (a) Symmetric two port feed at aperture of LPA. (b) Asymmetric one-port feed at aperture of LPA. 57

Figure 4.17: VSWR of the balanced two-port feed and the unbalanced one-port feed. 57

Figure 4:18: VSWR of the tapered dielectric LPA and FLPA. 58

Figure 4.19: Return loss of the tapered dielectric LPA and FLPA. 58

Figure 4.20: Realized gain of the tapered dielectric LPA and FLPA. 59

Figure 5.1: Relative permeability and loss tangent of P4 metaferrite in the $\underline{\mathbf{x}}_o$-direction. 62

Figure 5.2: Relative permeability and loss tangent of P4 metaferrite in the $\underline{\mathbf{y}}_o$-direction. 62

Figure 5.3: Relative permeability and loss tangent of P4 metaferrite in the $\underline{\mathbf{z}}_o$-direction. 63

Figure 5.4: Test bed cavity dimensions. (a) Transverse (x,y) plane. (b) Normal (x,z) plane. 65

Figure 5.5: Metaferrite placement in the cavity. (a) Transverse (x,y) plane. 66

(b) Normal (x,z) plane.

Figure 5.6: Measured and simulated S-parameters of the cavity test bed with Metaferrite. 67

Figure 5.7: Measured and simulated realized gain of the cavity test bed with Metaferrite. 67

Figure 5.8: Symmetrically loaded transmission line model with a short at either end. 68

Figure 5.9: Plot of equation 5.27 for various ratios of μ_z/ε_y with an assumed 3.3 inch depth. 76

Figure 5.10: The geometry of the anisotropic tapered LPA when $\mu_z/\varepsilon_y = 15$. 78

Figure 5.11: The CST model of the anisotropic tapered LPA when $\mu_z/\varepsilon_y = 15$. 78

Figure 5.12: VSWR of the loaded FLPA and the tapered anisotropic LPA. 79

Figure 5.13: Return loss of the loaded FLPA and the tapered anisotropic LPA. 79

Figure 5.14: Realized gain of the loaded FLPA and the tapered anisotropic LPA. 80

Figure 5.15: Polar plots of the far field radiation patterns of the anisotropic LPA. (a) 230 MHz. (b) 365 MHz. (c) 500 MHz. 80

Figure 5.16: VSWR of the anisotropic LPA utilizing a single port and a dual port matching network. 81

Figure 5.17: Return loss of the anisotropic LPA utilizing a single port and a dual port matching network. 82

Figure 5.18: Realized gain of the anisotropic LPA utilizing a single port and a dual port matching network. 82

Figure 5.19: The geometry of the non-tapered anisotropic LPA when $\mu_z/\varepsilon_y = 1$. 85

Figure 5.20: The CST model of the non-tapered anisotropic LPA when $\mu_z/\varepsilon_y = 1$. 85

Figure 5.21: VSWR of the tapered and non-tapered anisotropic LPA designs. 86

Figure 5.22: Return loss of the tapered and non-tapered anisotropic LPA designs. 86

Figure 5.23: Realized gain of the tapered and non-tapered anisotropic LPA designs. 87

Figure 5.24: Polar plots of the far field radiation patterns of the non-tapered 87

anisotropic LPA. (a) 230 MHz. (b) 365 MHz. (c) 500 MHz.

Figure 5.25: VSWR of the non-tapered anisotropic LPA with $\lambda_o = 0.375$ m. 88

Figure 5.26: Return loss of the non-tapered anisotropic LPA with $\lambda_o = 0.375$ m. 89

Figure 5.27: Realized gain of the non-tapered anisotropic LPA with $\lambda_o = 0.375$ m. 89

Figure 5.28: Polar plots of the radiation patterns of the anisotropic LPA for $\lambda_o = 0.375$ m. (a) 1.2 GHz. (b) 1.95 GHz. (c) 2.7 GHz. 90

Figure 5.29: Comparison of VSWR for the lossy and lossless media in the non-tapered anisotropic LPA design. 92

Figure 5.30: Comparison of return loss for the lossy and lossless media in the non-tapered anisotropic LPA design. 92

Figure 5.31: Comparison of realized gain for the lossy and lossless media in the non-tapered anisotropic LPA design. 93

Figure 5.32: Comparison of antenna efficiency for the lossy and lossless media in the non-tapered anisotropic LPA design. 93

Figure 5.33: VSWR of the FLPA, tapered, dielectric LPA, and non-tapered anisotropic LPA. 95

Figure 5.34: Return loss of the FLPA, tapered, dielectric LPA, and non-tapered anisotropic LPA. 95

Figure 5.35: Realized gain of the FLPA, tapered, dielectric LPA, and non-tapered anisotropic LPA. 96

Figure A.1: Tile of P4 Metaferrite manufactured by Metamaterials Inc. 110

Figure A.2: Relative permeability and loss tangent of P4 Metaferrite in the $\underline{\boldsymbol{x}}_o$-direction. 110

Figure A.3: Relative permeability and loss tangent of P4 Metaferrite in the $\underline{\boldsymbol{y}}_o$-direction. 111

Figure A.4: Relative permeability and loss tangent of P4 Metaferrite in the $\underline{\boldsymbol{z}}_o$-direction. 111

Figure A.5: Relative permittivity and loss tangent of P4 Metaferrite in the $\underline{\boldsymbol{x}}_o$-direction. 112

Figure A.6: Relative permittivity and loss tangent of P4 Metaferrite in the 112

$\underline{y}_o$-direction.

Figure A.7: Relative permittivity and loss tangent of P4 Metaferrite in the $\underline{z}_o$-direction. 113

Figure A.8: Electromagnetic model of the P4 Metaferrite tile. 115

Figure A.9: Simplified P4 Metaferrite block model as developed by ARL. 116

Figure A.10: Test bed cavity dimensions. (a) Transverse (x,y) plane. (b) Normal (x,z) plane. 118

Figure A.11: Metaferrite placement in the cavity. (a) Transverse (x,y) plane. (b) Normal (x,z) plane. 119

Figure A.12: Measured and simulated S-parameters of the loaded cavity test bed. 120

Figure A.13: Measured and simulated realized gain of the loaded cavity test bed. 121

Figure B.1: Geometry of a linearly tapered cavity partially loaded with a high index medium. 123

Figure B.2: Realized gain of the linearly tapered cavity loaded with dielectric and magnetic media. 124

Figure B.3: Return loss of the linearly tapered cavity loaded with dielectric and magnetic media. 125

Figure B.4: Realized gain of the linearly tapered cavity loaded with a magneto-dielectric medium. 126

Figure B.5: Return loss of the linearly tapered cavity loaded with a magneto-dielectric medium. 127

Figure B.6: Realized gain of the linearly tapered cavity loaded with anisotropic dielectric media. 128

Figure B.7: Return loss of the linearly tapered cavity loaded with anisotropic dielectric media. 129

Figure B.8: Realized gain of the linearly tapered cavity loaded with anisotropic magnetic media. 130

Figure B.9: Return loss of the linearly tapered cavity loaded with anisotropic magnetic media. 131

Figure B.10: Realized gain of the linearly tapered cavity loaded with anisotropic magnetic media with varying μ_x. 133

Figure B.11: Return loss of the linearly tapered cavity loaded with anisotropic magnetic media with varying μ_x. 133

Figure B.12: Realized gain of the linearly tapered cavity loaded with anisotropic magnetic media with different flange sizes. 135

Figure B.13: Return loss of the linearly tapered cavity loaded with anisotropic magnetic media with different flange sizes 135

Figure B.14: Realized gain of the linearly tapered cavity loaded with anisotropic magnetic media with different probe widths. 137

Figure B.15: Return loss of the linearly tapered cavity loaded with anisotropic magnetic media with different flange sizes. 137

Figure C.1: A plane wave incident from free space on an anisotropic boundary. 146

Figure C.2: A plane wave incident from an anisotropic medium on a free space boundary. 146

Figure D.1: (a) Half space boundary between the waveguide aperture and free space. (b) Transverse (x,y) cross section of the waveguide. 150

Figure D.2: Plot of the values of k_x and k_y obtained for $\phi = 0$. 160

Figure D.3: Plot of the values of k_x and k_y obtained for $\phi = \pi/4$. 161

Figure D.4: Transverse (x,y) plane of a waveguide aperture surrounded by an infinite flange. 163

Figure D.5: CST model of the waveguide excited by a matched waveguide port. 163

Figure D.6: The cosine TE_{10} mode electric field distribution in the waveguide. 164

Figure D.7: Polar plot of the normalized far field E_θ and E_ϕ radiation patterns. 165

Figure D.8: Linear plot of the normalized far field E_θ and E_ϕ radiation patterns. 165

Figure D.9: Plot of the singular values of the MDM in descending order. 166

Figure E.1: Geometry of a commercial 50 Ω coaxial line. 168

Figure E.2: Field distribution of the TEM mode calculated by the waveguide port in the coaxial line. 169

Figure E.3: Mesh cell representation of the transverse (x,y) plane of the coaxial port geometry. 171

Figure E.4: PMC boundary condition across the symmetric vertical dimension of the LPA model. 172

List of Tables

Table 2.1: Comparison of state of the art wideband LPA designs. 20

Table 3.1: Normalized dimensions for the model shown in figure 3.6 scaled by λ_o. 29

Table 3.2: Normalized dimensions of the geometry in figure 3.11a scaled by λ_o. 34

Table 3.3: Comparison of FLPA to state of the art wideband LPA designs. 37

Table 3.4: Normalized dimensions for the simulations run for geometry in figure 3.17. 39

Table 4.1: Normalized dimensions for the tapered cavity models given in figure 4.6. 52

Table 4.2: Comparison of tapered LPAs to state of the art wideband LPA designs. 60

Table 5.1: Normalized dimensions for the tapered cavity models given in figure 5.10. 78

Table 5.2: Normalized dimensions for the non-tapered anisotropic LPA model in figure 5.19. 85

Table 5.3: Comparison of non-tapered anisotropic LPA to state of the art wideband LPA designs. 97

Table B.1: Normalized dimensions for the tapered cavity model of figure B.1. 123

Table B.2: Normalized dimensions for the linearly tapered cavity when $\mu_x = 15$. 133

List of Acronyms

CCWT	Commercial Coaxial Line to Waveguide Transition
CLPA	Cylindrical Low Profile Antenna
CST	Computer Simulation Technology
CWT	Coaxial Line to Waveguide Transition
DB	Decibel
DNG	Double Negative
FDTD	Finite Difference Time Domain
FLPA	Flat Low Profile Antenna
GHz	Gigahertz
LPA	Low Profile Antenna
MCLI	Microwave Communications Laboratories Inc.
MDM	Modal Decomposition Matrix
MHz	Megahertz
PEC	Perfect Electric Conductor
SMA	Sub-Miniature A
SVD	Singular Value Decomposition
TE	Transverse Electric
TM	Transverse Magnetic
UHF	Ultra-High Frequency
VSWR	Voltage Standing Wave Ratio

Chapter 1
Introduction

Many applications in wireless communications and radar require antennas that conform to the surface of a supporting structure. Whenever applicable, we approximate the antenna by a planar aperture that minimizes the dimension normal to the aperture, otherwise known as the profile of the antenna. Low profile antennas (LPA) are of special importance within the ultra-high frequency (UHF) band where they are used as communications antennas on military platforms. LPAs reduce platform visibility and decrease antenna weight which becomes critically important in airborne platforms.

The goal of this research is to analyze the properties of anisotropic metamaterials as an effective medium used to reduce the profile of a radiating rectangular cavity at low UHF. We compare techniques between anisotropic and isotropic media as well as other state of the art techniques involving exotic media from the literature. Traditionally, waveguides achieve broadband performance via a coaxial line-to-waveguide transition (CWT) which terminates in a matching network consisting of a conducting probe. When we terminate the waveguide in a shorted reflector, then the electrical height between the matching network and the backshort is approximately $\lambda_g/4$ at the center frequency where λ_g is the guide wavelength [1], [2]. This results in a large profile at low UHF frequencies because λ_g is very large.

In this research, the antenna under investigation is a flush mounted rectangular cavity with a $\lambda_o/2$ opening which serves as the radiating aperture. We show this configuration in figure 1.1. We feed the antenna by a two-port matching network fed 180° out of phase at the aperture. In this configuration, the backshort defines the entire profile of the cavity in the normal direction. Ideally, the backshort should be as small as

possible. Our approach loads the cavity with a high index, anisotropic medium to realize a reduction in the height of the LPA profile by effectively limiting the distance between the backshort and the matching network. We define a high index medium as the product of relative electrical permittivity (ε_r) and magnetic permeability (μ_r) being greater than 10. For anisotropic media we define high index as the product of the two largest elements from the $\underline{\underline{\varepsilon}}_r$ and $\underline{\underline{\mu}}_r$ tensors being greater than 10. However, this approach also serves to alter the resonance established by the $\lambda_o / 2$ separation of the cavity walls in the horizontal direction. We use a transverse resonance condition established between the walls of the cavity and the high index medium to suppress the introduction of high order resonances introduced by the high refractive [3]. We derive this transverse resonance condition for both the isotropic and anisotropic cases, and we compare the resulting LPA designs.

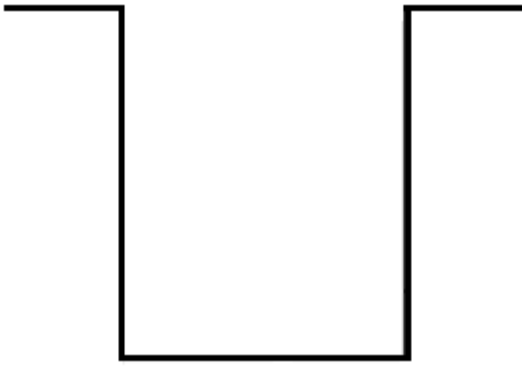

Figure 1.1: Flush mounted radiating rectangular cavity.

Of particular interest are positive index, anisotropic, and magnetic media exhibiting low loss in the UHF band [4], [5]. Much of the work in metamaterials focuses on the unique electromagnetic properties of double negative (DNG) media ($\varepsilon_r \leq 0$, $\mu_r \leq 0$). However, a class of engineered media exists that exhibits positive ε_r and μ_r with magnetic

loss tangents of $\tan\delta \leq 0.25$. While this may seem high in comparison to traditional dielectric loss tangents on the order of 0.02 or better, this research shows that positive index metamaterials are still effective in LPA design. Traditionally, magnetic media have high losses at frequencies above 100 MHz, which makes them unsuitable as substrates for UHF antennas [6]. Magnetic metamaterials are man-made materials comprised of a periodic structure using microscopic magnetic inclusions to produce effective magnetic properties. The availability of artificial magnetic metamaterials widens the range of LPA design approaches. Furthermore, the development of anisotropic media allows separate control of the values of the $\underline{\underline{\boldsymbol{\mu}}}_r$ and $\underline{\underline{\boldsymbol{\varepsilon}}}_r$ tensors in all three Cartesian directions. We describe the characteristics of a typical anisotropic magneto-dielectric metamaterial in detail in appendix A from manufacturing to modeling, tensor values of $\underline{\underline{\boldsymbol{\mu}}}_r$ and $\underline{\underline{\boldsymbol{\varepsilon}}}_r$, and loss tangents.

Anisotropic media provide unique properties not available using isotropic media. These include a high effective refractive index reducing wavelength in the medium, relatively low magnetic losses at MHz frequencies, and lower density and weight than traditional isotropic materials. Anisotropic media can be up to five times less dense than traditional ferrites while exhibiting magnetic properties with lower loss tangents. For this dissertation, we define a general anisotropic medium by the diagonal tensors [7]

$$\underline{\underline{\varepsilon}}_r = \begin{bmatrix} \varepsilon_x & 0 & 0 \\ 0 & \varepsilon_y & 0 \\ 0 & 0 & \varepsilon_z \end{bmatrix}, \tag{1.1a}$$

$$\underline{\underline{\mu_r}} = \begin{bmatrix} \mu_x & 0 & 0 \\ 0 & \mu_y & 0 \\ 0 & 0 & \mu_z \end{bmatrix}. \tag{1.1b}$$

Previous work includes plane wave solutions to propagation in anisotropic media [8]-[10]. Furthermore, modal decomposition of rectangular waveguides filled with anisotropic magneto-dielectrics has also been performed along with in depth analysis of cutoff wave numbers and field distribution in terms of the anisotropic tensors [11], [12]. However, these investigations tend to focus on the class of metamaterials known as DNG, and no application to realizable wideband antenna designs are applied.

1.1 Thesis Contributions

In this work, we show how positive index anisotropic media lend themselves to realizable wideband LPA designs. Our approach yields a radiating rectangular cavity partially loaded with anisotropic magnetic metamaterial fed by a two-port variation on a typical CWT. Our final design yields an antenna profile of $0.04\lambda_o$ with positive realized gain and 1.2 octaves of bandwidth, where λ_o is the free space wavelength at frequency of lowest resonance. We define an octave as two frequency values that satisfy the identity $(f_2 - f_1) / f_1 = 1$, where f_2 is the upper frequency and f_1 is the lower frequency of the octave. As our figures of merit we use realized gain, return loss, and VSWR to define our bandwidth.

The return loss represents the power not delivered to a load when there is an impedance mismatch between the generator and the load. A transmission line separates the generator from the load providing both a characteristic impedance and phase

difference dependent on the length of the line. We measure the return loss at the input to the transmission line and define the return loss in dB as

$$RL = 20*\log10(|\Gamma|), \tag{1.2}$$

where Γ is the reflection coefficient. As we can see from equation 1.2, the return loss is a transformation of the percentage of power reflected at the load into decibels.

The VSWR is the ratio of the maximum voltage to the minimum voltage on a transmission line and is a measure of the mismatch of a transmission line. At a mismatched load, the reflected wave causes standing waves along the line whose magnitude varies with position along the line. We define VSWR as

$$VSWR = V_{max} / V_{min} = [1+|\Gamma|] / [1-|\Gamma|], \tag{1.3}$$

The higher the VSWR, the worse the mismatch at the load. Similarly, the lower the VSWR the better the transmission line is matched to the load. A perfect match represents a reflection coefficient of zero and VSWR = 1.

The realized gain of the antenna is a measure of the directivity of the antenna taking into account the radiation efficiency of the antenna and the impedance match at the input to the antenna. For a perfectly matched antenna with no internal antenna losses, the realized gain would equal the directivity. However, this does not happen in practice, therefore the realized gain is the directivity multiplied by the radiation efficiency and the transmission coefficient at the antenna input

$$RG = \eta D[1-|\Gamma|^2], \tag{1.4}$$

where η is the radiation efficiency and D is the directivity.

In chapter 2, we evaluate the traditional CWT as the basis for our LPA matching network. Engineers use this method extensively to feed larger waveguides in antenna

applications, and many commercial products exist on the market with good performance. We also review anisotropic dielectric plane wave theory developed by Pozar [8] and Graham [10] as well as the full magneto-dielectric version as applied to rectangular waveguides as established by Meng, et. al [11], [12]. Lastly, chapter 2 gives an overview of other state of the art LPA designs, many of which take advantage of the unique properties of engineered metamaterials of various forms.

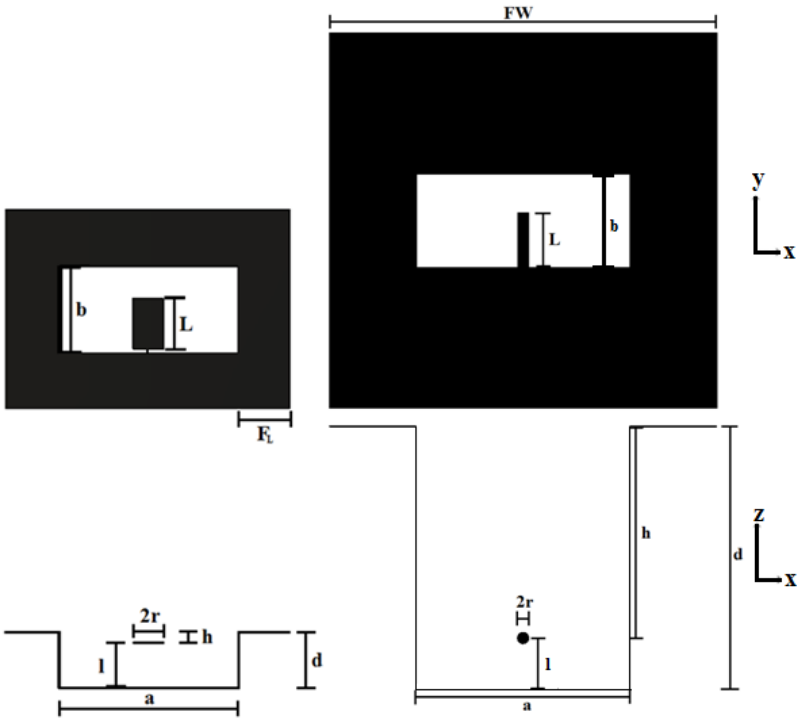

Figure 1.2: To-scale diagram of the antenna profile in both the transverse (*x*,*y*) and the normal (*x*,*z*) planes. (a) FLPA. (b) Radiating waveguide.

In chapter 3, we alter a traditional CWT into a flat rectangular probe, whose probe dimensions act as a tunable matching network. This establishes a wideband return loss of better than -10 dB over 1.5 octaves of bandwidth. This initial design of a LPA utilizing a flat rectangular probe (FLPA) reduces the profile of a radiating waveguide from $0.61\lambda_o$ to

$0.14\lambda_o$ or 77.0%. We show a scale comparison of the resulting FLPA to a radiating waveguide in figure 1.2a and figure 1.2b respectively. The end of chapter 3 investigates the effects of loading the backshort of the cavity to reduce λ_g. We find this introduces destructive high order resonances by lowering the frequency of lowest resonance established by the separation of the cavity walls.

Chapter 4 uses the concept of the transverse resonance of a partially loaded parallel plate waveguide to derive a novel relationship for L_g vs. w for the geometry of a tapered backshort loaded with a linearly varying isotropic medium. In this description, w is the width of the medium at any point z within the cavity, and L_g is the resulting distance from the medium to the metallic cavity boundary. We show this geometry in figure 1.3b for a cavity partially loaded with a dielectric medium. We achieve this result by using a shorted transmission line description of the waveguide in the transverse direction, and assuming higher order resonances decay exponentially to infinity [3]. We apply this geometric result to our design in figure 1.3a while loading the cavity with an isotropic medium.

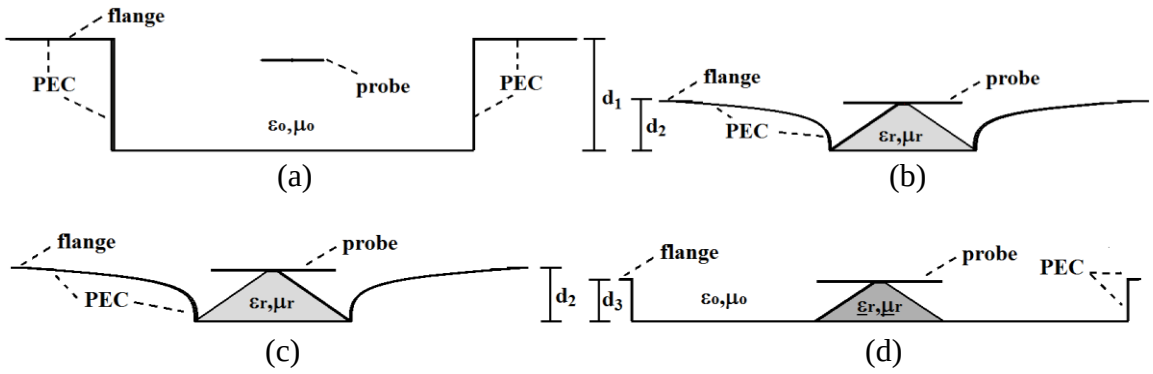

Figure 1.3: To-scale diagrams of the antenna profiles in the normal (x,z) plane.

(a) FLPA. (b) Isotropic dielectric LPA. (c) Isotropic dielectric LPA.

(d) Anisotropic LPA.

The novel design of figure 1.3b and figure 1.3c establishes a constant $\lambda_o/2$ resonance that suppresses the higher order resonances within the cavity. This approach achieves a return loss of better than -10 dB over 285 MHz to 435 MHz (0.53 octaves) with a profile of $0.05\lambda_o$. The realized gain at bore sight is positive from 200 MHz to 405 MHz (1.0 octaves) and peaks at 7.6 dB at 300 MHz. The realized gain drops precipitously above 375 MHz due to reduced cancellation of radiation to boresight when the dimensions of our matching network are odd multiples of $\lambda_o/4$. This design uses commercial ROGERS610 dielectric ($\varepsilon_r = 10.2$, $\mu_r = 1$, $\tan\delta = 0.002$) to load the backshort.

The design also uses an improved two-port, balanced feed where the two ports are driven 180° out of phase. An asymmetric probe feed produces fringing fields over the voltage potential difference between the probe and the grounded cavity walls. These fringing fields cause a reactance that produces a mismatch between the coaxial line and the impedance seen at the cavity aperture. We reduce this mismatch using a balanced feed structure. By feeding the two ports 180° out of phase, there is now a voltage potential difference between the two probes providing a continuous path for the current, which improves our match over a traditional one-port CWT.

Chapter 4 also investigates loading a cavity with isotropic lossless magnetic material. This investigation is purely theoretical as purely magnetic isotropic materials with low loss have not been realized in practice. However, it is important to note the differences in performance for the magnetic and dielectric cases, as this will form some basis for our findings for the anisotropic media we investigate in chapter 5. The magnetic cavity design achieves a return loss of -6 dB from 260 MHz to 460 MHz with a small resonance causing the voltage-to-standing wave ratio (VSWR) to climb to 4 at 315 MHz.

However the VSWR curve is relatively flat and stays below 4 from 200 MHz to 475 MHz, and we believe that we may improve the return loss and extend the bandwidth across this whole frequency range by further optimization of the probe dimensions. The realized gain remains positive from 155 MHz to 435 MHz (1.8 octaves) except at 315 MHz where the VSWR degrades, and peaks at 7.85 dB at 290 MHz. The realized gain performance indicates that the magnetic material may be capable of providing more gain and a wider bandwidth than the purely dielectric material.

In chapter 5, we derive the anisotropic transverse resonance condition for a parallel plate waveguide based on anisotropic adaption of Maxwell's equations [11], [12]. The concept of anisotropic transverse resonance is not established in the literature for partially loaded waveguides. We then apply this concept to derive the relationship of L_g vs. w for a tapered cavity loaded with a linearly varying anisotropic medium, similar to chapter 4. Based on our derivation of the characteristic impedance of the anisotropic medium, we show that its presence negates the need for a tapered cavity as long as $\varepsilon_y = 1$ and $\mu_z = 1$. We show this non-tapered geometry in figure 1.3d achieving a -6 dB return loss or better over 1.2 with a profile of $0.04\lambda_o$ using the following $\underline{\underline{\varepsilon_r}}$ and $\underline{\underline{\mu_r}}$ tensors

$$\underline{\underline{\varepsilon_r}} = \begin{bmatrix} 1 & 0 & 0 \\ 0 & 1 & 0 \\ 0 & 0 & 1 \end{bmatrix}, \tag{1.5a}$$

$$\underline{\underline{\mu_r}} = \begin{bmatrix} 15 & 0 & 0 \\ 0 & 1 & 0 \\ 0 & 0 & 1 \end{bmatrix}. \tag{1.5b}$$

The realized gain is positive from 165 MHz to 520 MHz peaking at 8.4 dB around 460 MHz.

This result shows a definite advantage in the use of anisotropic media over isotropic media both in return loss bandwidth, realized gain, and profile reduction. This also demonstrates comparable performance to the air-filled cavity of figure 1.2a and figure 1.3a with a profile of $0.14\lambda_o$. The anisotropic medium, coupled with our novel cavity design which suppresses destructive high order resonances, reduces the profile of our air filled cavity by 71.4% with minimal loss in performance. Figure 1.3a through figure1.3d shows a scale comparison of the resulting isotropic and anisotropic LPA designs to the FLPA design of figure 1.2a. Note that $d_2 = 0.48d_1$ and $d_3 = 0.73d_2$.

Chapter 2
Review of Prior Art

2.1 Coaxial Line to Waveguide Transition (CWT)

In practice, the CWT is used to great effect in providing a good impedance match between a 50 Ω coaxial cable and a rectangular waveguide of arbitrary dimension [1], [13]. Collin provides an analysis on this type of structure based on a theory of the coupling of small apertures [2]. The structure consists of a coaxial line terminated in the center of the broad face of a rectangular waveguide as shown in figure 2.1. The inner conductor of the waveguide extends a distance L into the waveguide, and a short circuit is placed a distance ℓ to the left of the probe [14]. By correctly tuning the values of L and ℓ, the input impedance seen at the location of the probe in the waveguide is equal to the characteristic impedance of the coaxial line over a broad range of frequencies [1], [2]. Therefore this probe acts as a matching network for the CWT. Our research takes advantage of the ability to tune this simple matching network to get an impedance match while attempting to reduce the dimension ℓ to less than $\lambda_o/20$ at low UHF frequencies. Therefore, we take an in depth look at how coaxial line-to-rectangular waveguide adapters expect to perform and for what dimensions they are optimized.

Paul Wade describes an approach to determine the dimensions of a CWT empirically [1]. For a WR90 waveguide with a = 22.86 mm and b = 10.16 mm, Wade determines optimum values of L = 5.89 mm, ℓ = 5.46 mm, and r = 0.635 mm at 10.368 GHz through iterative measurements. Wade's design based on a CWT to a WR90 waveguide at 10.368 GHz yields a $0.19\lambda_g$ backshort with a 0.79 octave bandwidth based on a 2:1 VSWR. A 2:1 VSWR corresponds to a -10 dB return loss.

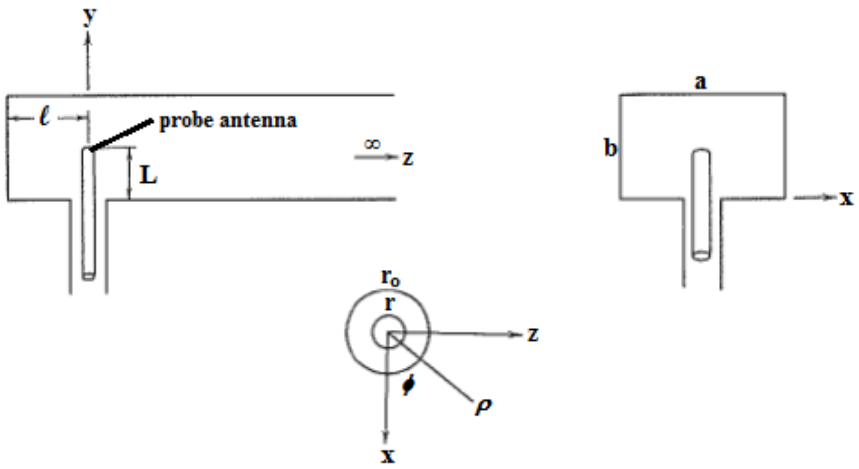

Figure 2.1: Geometry of a traditional CWT [2].

Unfortunately, Wade gives no information on the dimension *h*, which describes the distance from the probe to the flange. This is because Wade does not intend his design to be used as a standalone radiating element. He assumes that his adapter connects to a longer length of waveguide that terminates in a matched load. However, we will use his insights on tuning the backshort and the matching network to achieve a good impedance match in our low profile cavity design.

2.2 Propagation in Anisotropic Media

The electromagnetic wave propagation in homogeneous anisotropic dielectric media has been well understood in optical media since the 1950s. We define an anisotropy as a medium whose permittivity and permeability are the diagonal tensors [7]

$$\underline{\underline{\varepsilon_r}} = \begin{bmatrix} \varepsilon_x & 0 & 0 \\ 0 & \varepsilon_y & 0 \\ 0 & 0 & \varepsilon_z \end{bmatrix}, \tag{2.1a}$$

$$\underline{\underline{\mu_r}} = \begin{bmatrix} \mu_x & 0 & 0 \\ 0 & \mu_y & 0 \\ 0 & 0 & \mu_z \end{bmatrix}. \qquad (2.1b)$$

This differs from the definition of permittivity and permeability of an isotropic medium as ε_r and μ_r. In an anisotropic medium, $\underline{\underline{\boldsymbol{\varepsilon}}}_r$ and $\underline{\underline{\boldsymbol{\mu}}}_r$ can differ in any of the three Cartesian directions, whereas in an isotropic medium ε_r and μ_r are the same in all directions. In fact, an isotropic medium is simply a special case of anisotropy, and we can define $\underline{\underline{\boldsymbol{\varepsilon}}}_r = \varepsilon_r \underline{\boldsymbol{I}}$ and $\underline{\underline{\boldsymbol{\mu}}}_r = \mu_r \underline{\boldsymbol{I}}$, where $\underline{\boldsymbol{I}}$ is the identity matrix.

At optical frequencies, one has to rely on naturally occurring crystalline media with anisotropic properties. As early as 1958 Collin showed that at microwave frequencies, where the wavelength is much greater, it is possible to fabricate artificial dielectric media having anisotropic properties [14]. Furthermore, the effects of anisotropic dielectric media on a loaded patch antenna were demonstrated by David Pozar [8]. Many engineers have expanded on the principles developed by Pozar in this work, with the most comprehensive recent study performed by Jennifer Graham [10]. She determines the transmission line behavior of planar microstrip antennas loaded with anisotropic dielectric media. More specifically she shows how the birefringence of waves propagating in anisotropic media affect the reflection and transmission coefficients at a half space boundary between an anisotropic medium and free-space.

The development of low loss anisotropic magneto-dielectrics in the last fifteen years greatly expands the current antenna design space. Anisotropic media provide unique properties not available using conventional media. These include a high effective refractive index reducing wavelength in the medium, relatively low magnetic losses at

MHz frequencies, and lower density and weight than traditional isotropic materials. The ability to achieve high values of permeability with low loss tangents is the catalyst in the development of low profile and wideband antennas [16].

While Pozar and Graham's work focuses purely on anisotropic dielectric media, Ren, et. al and Meng, et. al have focused on plane wave solutions for anisotropic magneto-dielectric media [9], [11], [12]. Of special importance to our work are the solutions to the transverse electric and magnetic field components as well as the anisotropic wave equations. We reproduce these solutions here for convenience, but we present a rigorous derivation in appendix C

$$E_x = -\frac{j}{k_o^2 \mu_y \varepsilon_x - k_z^2}\left(\omega \mu_o \mu_y \frac{dH_z}{dy} + k_z \frac{dE_z}{dx}\right), \tag{2.2a}$$

$$E_y = \frac{j}{k_o^2 \mu_x \varepsilon_y - k_z^2}\left(\omega \mu_o \mu_x \frac{dH_z}{dx} - k_z \frac{dE_z}{dy}\right), \tag{2.2b}$$

$$H_x = \frac{j}{k_o^2 \mu_x \varepsilon_y - k_z^2}\left(\omega \varepsilon_o \varepsilon_y \frac{dE_z}{dy} - k_z \frac{dH_z}{dx}\right), \tag{2.2c}$$

$$H_y = -\frac{j}{k_o^2 \mu_y \varepsilon_x - k_z^2}\left(\omega \varepsilon_o \varepsilon_x \frac{dE_z}{dx} + k_z \frac{dH_z}{dy}\right), \tag{2.2d}$$

$$\frac{\varepsilon_x}{k_o^2 \mu_y \varepsilon_x - k_z^2}\frac{d^2 E_z}{dx^2} + \frac{\varepsilon_y}{k_o^2 \mu_x \varepsilon_y - k_z^2}\frac{d^2 E_z}{dy^2} + \varepsilon_z E_z = 0, \tag{2.3a}$$

$$\frac{\mu_x}{k_o^2 \mu_x \varepsilon_y - k_z^2}\frac{d^2 H_z}{dx^2} + \frac{\mu_y}{k_o^2 \mu_y \varepsilon_x - k_z^2}\frac{d^2 H_z}{dy^2} + \mu_z H_z = 0. \tag{2.3b}$$

Furthermore, modal decomposition of rectangular waveguides filled with anisotropic magneto-dielectrics has also been performed along with in depth analysis of cutoff wave numbers and field distribution in terms of the anisotropic tensors [11], [12].

However, these investigations tend to focus on DNG metamaterials, and do not usually apply to realizable low profile, wideband LPA designs at UHF.

2.3 Review of Low Profile Wideband Antennas

This section provides an overview of various state of the art wideband, reflector-backed LPA designs from the literature. Generally speaking these types of LPAs fall into three categories: 1) those employing traditional substrates, 2) those employing an engineered high impedance surface (HIS) that acts as an artificial magnetic conductor (AMC), and 3) those employing electromagnetic band-gap (EBG) reflectors which also acts like an AMC reflector with the added benefit of increasing radiation efficiency by cancelling surface waves. Since the focus of this dissertation is on minimizing the profile of cavity-backed antennas, all antennas in this review either employ a cavity or some sort of ground plane to act as a reflector. We rate these antennas based on the electrical height of their profile, their bandwidth, and their realized gain. For purposes of comparison, we assume all antennas are scalable in frequency.

The first class of antennas are those employing traditional substrates. For brevity's sake, we give only a few examples of a multitude of different LPA configurations, but these examples demonstrate the effectiveness and limitations of these types of designs. The main benefits of these antennas are low cost, low weight, and ease of production as they do not rely on any exotic or engineered materials.

The first LPA [17] takes advantage of the wideband characteristics of a traditional Archimedean spiral, and achieves 7.3 octaves of bandwidth with -2.6 dB to 6.9 dB for a profile of $0.03\lambda_o$. Figure 2.2 shows the assembly of this design. They pattern the spiral on Rogers 4003C and back the aperture with a rectangular cavity. The four spiral arms

are fed by four ports each 90° out of phase. This antenna achieves very good performance for an extremely thin cavity; however, it is based on an aperture that is limited to circular polarization and the need for three lossy splitters limits the gain especially at the lower frequencies.

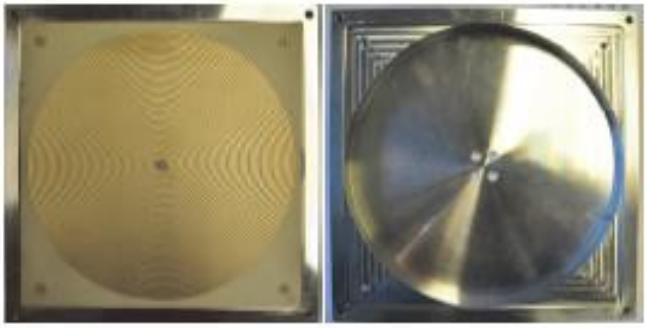

Figure 2.2: Design of the spiral antenna. Top view of the assembled antenna (left). Top view of the cavity (right) [17].

The second LPA [18] is a three dimensional inverted L type aperture placed above a grounded slab of FR-4 substrate. Figure 2.3 shows a prototype of the inverted L antenna. Although, this is a three dimensional aperture, the total profile of the entire structure is only $0.09\lambda_o$. This achieves a bandwidth of 0.59 octaves, however broadband realized gain measurements are not given.

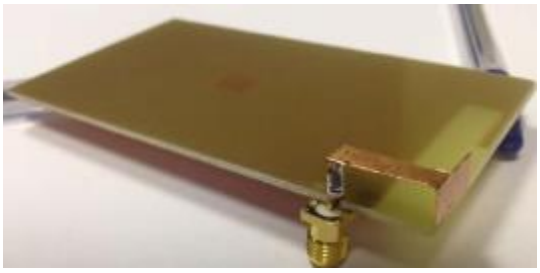

Figure 2.3: Prototype of the inverted L antenna [18].

The third LPA [19] is another three dimensional aperture which consists of a layered, slotted bowtie. Figure 2.4 shows the geometry of this design. The two arms of

the bowtie are separated by a layer of GIL GML 1032 substrate, and the bottom arm acts as a ground plane for the transmission line feed of the top arm. A $0.05\lambda_o$ air layer separates another grounded substrate layer, and common ground is maintained with the top layers by two parallel shorted copper plates. This configuration achieves a 0.77 octave bandwidth with a realized gain of 4.0 dB to 6.0 dB for a total profile of $0.064\lambda_o$.

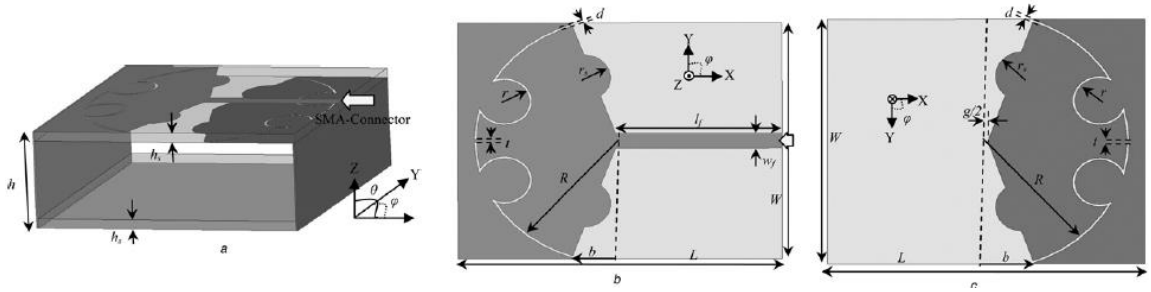

Figure 2.4: Three dimensional layered slotted bowtie [19].

The final LPA employing non-exotic substrates [20] is a variation on a traditional discone antenna. Figure 2.5 shows the geometry of the discone antenna design. No substrate is used, and in order to reduce the profile of a three dimensional discone, a large cone angle is used. This deteriorates the input match. By grounding the bottom disk aperture to the cavity and providing a short circuit between the top disk and bottom disk new resonances are produced at the bottom and top of the frequency band thereby improving the match. This unique matching network provides 0.92 octaves of bandwidth for a profile of $0.09\lambda_o$, but no realized gain measurements are given.

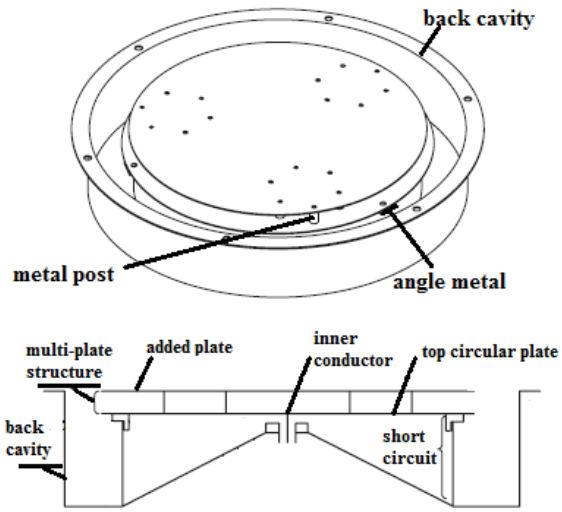

Figure 2.5: Cavity backed discone antenna [20].

The second class of antennas are those employing HIS or EBG reflectors. Again, we give only a few representative examples to demonstrate the effectiveness and limitations of these types of designs. The main benefit of these LPAs are that they allow the engineer to place the radiating element extremely close to the surface of the HIS without shorting out the electric fields because the surface acts as an AMC.

The first AMC LPA [21] combines a basic wideband planar monopole with a HIS substrate. Figure 2.6 shows this geometry. The HIS consists of a 3x4 grid of unit cells comprised of a square metallic ring etched on a foamed PVC dielectric substrate. The monopole is fed with a microstrip transmission line and a layer of air separates the monopole and the surface of the HIS. A second air gap separates the HIS substrate from the ground plane. No unit cells are placed beneath the length of transmission line. This LPA achieves 0.77 octaves of bandwidth and a realized gain of 7.0 dB to 10.25 dB with a profile of $0.1\lambda_o$.

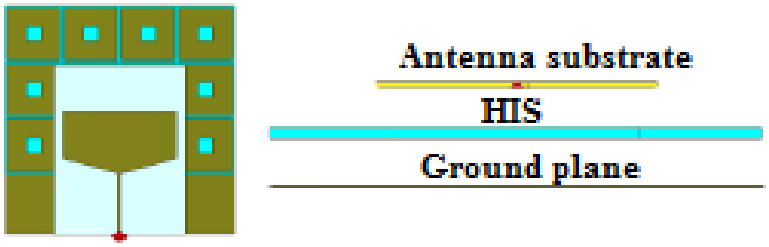

Figure 2.6: Monopole antenna above a HIS substrate [21].

The second AMC LPA [22] is a bowtie layered on top of a FR-4 substrate, a HIS surface, and a ground plane. Figure 2.7 shows the geometry of this design. The HIS is a simplified version of that described in [21] in that the unit cell is simply a square patch printed on FR-4 substrate. However, the bowtie is placed on a 14x14 grid of unit cells, and there is no air gap between the bowtie and HIS or the HIS and the ground plane. This LPA achieves 1.07 octaves of bandwidth with a realized gain of 3.3 dB to 9.35 dB for a profile of $0.05\lambda_o$.

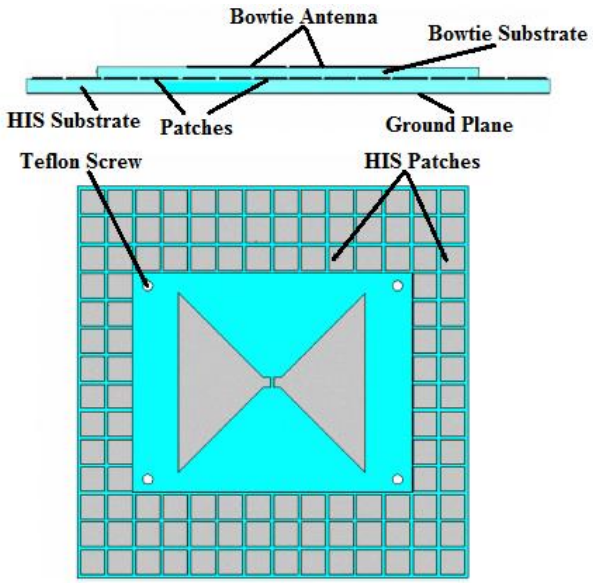

Figure 2.7: Bowtie above the HIS structure [22].

The final AMC LPA [23] is a center fed dipole suspended on top of an EBG reflector consisting of typical mushroom-like unit cells. Figure 2.8 shows the geometry

of this design. This is very similar to the LPA described in [22]. In this configuration one major drawback is that the dimensions of the EBG surface are 9.3 times larger than the dipole. The EBG unit cells are etched on a dielectric substrate with $\varepsilon_r = 2.3$ and $\tan\delta = 0.002$. An air gap separates the dipole from the EBG surface. This LPA achieves 0.41 octaves of bandwidth but no realized gain information is given. The profile of this LPA is $0.06\lambda_o$.

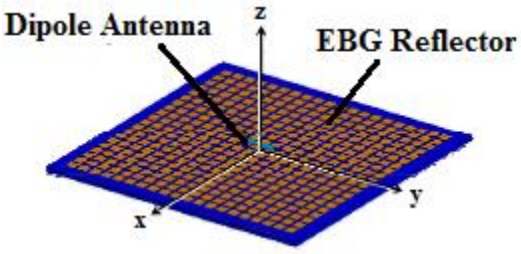

Figure 2.8: Dipole antenna above the EBG patch [23].

Table 2.1: Comparison of state of the art wideband LPA designs.

reference	Aperture	substrate	BW (octaves)	gain (dB)	profile (λ_o)
[17]	spiral	dielectric	7.3	-2.6 to 6.9	0.03
[18]	inverted L	dielectric	0.59	-	0.09
[19]	bowtie	dielectric	0.77	4.0 to 6.0	0.064
[20]	discone	none	0.92	-	0.09
[21]	monopole	HIS/EBG	0.77	7.0 to 10.25	0.1
[22]	bowtie	HIS/EBG	1.07	3.3 to 9.35	0.05
[23]	dipole	HIS/EBG	0.41	-	0.06

Table 2.1 lists the important characteristics of the LPA designs we outline in this section. Clearly the cavity-backed spiral is the best performer. With such a wide bandwidth, the poor performance at the very lowest frequencies is forgiven as even the upper 6 octaves far outstrips the bandwidth of any of the other antennas. However, this does not allow for linear polarization. The other antennas are linearly polarized, but lack bandwidth. We hope to achieve more than an octave of bandwidth utilizing anisotropic

media, and the only other linearly polarized LPA that achieves this is the bowtie backed by an AMC reflector. This also achieves high gain and a $0.05\lambda_o$ profile. These are all goals of our design, and we hope to outperform this antenna.

Chapter 3
Radiating Rectangular Cavities

This chapter investigates the performance of various designs for radiating rectangular cavities. First we show results for the semi-infinite flanged rectangular waveguide. This is a theoretical exercise, as a semi-infinite waveguide cannot exist in reality. However, this provides us with a fundamental understanding of how fields and modes behave inside a rectangular waveguide. A full description of the fields and modes inside the waveguide are given in appendix D. We compare the results of our numerical analysis to numerical calculations of the far field radiation pattern provided by CST Studio Suite 2014. Using the traditional CWT as a starting point, we design a wideband radiating rectangular cavity at UHF using a wide, flat rectangular probe as an improvement on the matching networks proposed by Wade [1] and Collin [2] . Our matching network yields a radiating cavity with a profile of $0.154\lambda_o$, a -10 dB bandwidth of the 1.44 octaves, and a realized gain between 4.8 dB and 8.2 dB. Finally, we show that we can achieve further profile reduction by loading the backshort with a high index medium; however, this also introduces destructive higher order resonances that make it impossible to achieve a good impedance match at the input.

3.1 Semi-infinite Rectangular Waveguide

This section analyzes the behavior of a semi-infinite rectangular waveguide whose aperture is surrounded by an infinite flange. Figure 3.1 gives the transverse dimensions of the waveguide where $a = \lambda_o / 2$ and $b = \lambda_o / 4.5$. The rectangular dimensions are defined by the existence of a PEC boundary with the dimensions a x b. Figure 3.2 shows a 3D model of the waveguide where the aperture is surrounded by a PEC flange. The waveguide is meant to extend infinitely in the $-\underline{\hat{z}}_o$ direction. Placing a waveguide port at

the end of the waveguide mimics this setup as shown in figure 3.2. Because CST calculates the characteristic impedance of the waveguide across frequency, the waveguide port is perfectly matched to the impedance of the waveguide. This means there will be zero reflection from the waveguide port making it act like an absorber. This is equivalent to saying that the mode travels down the infinite dimension of the waveguide with no reflections.

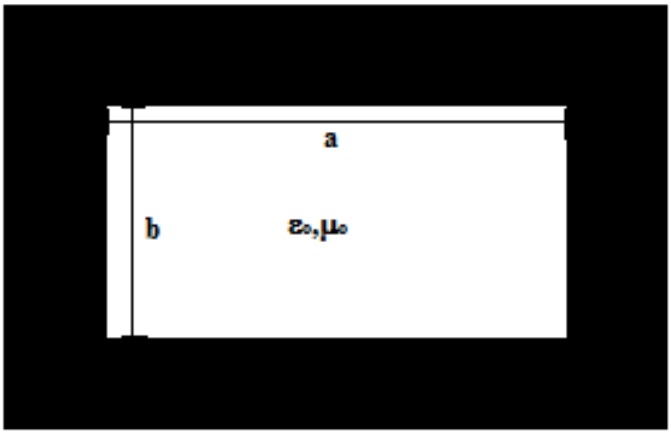

Figure 3.1: Transverse (x,y) plane of a waveguide aperture surrounded by an infinite flange.

As long as $a \geq 2b$, the dominant mode in the waveguide will be the TE_{10} mode [1], [3], [24]. The frequency of resonance (f_r) represents the lowest frequency which allows the TE_{10} mode to propagate [3], [25]. We establish a resonance in the horizontal direction when $a = \lambda_o / 2$. In this case, the equation for f_r is

$$f_r = \frac{c_o}{\lambda_o \sqrt{\varepsilon_r \mu_r}}. \tag{3.1}$$

For frequencies below f_r, no modes will propagate in the waveguide, and for frequencies above $2f_r$ more than one mode will propagate in the waveguide. The waveguide port

will absorb any reflections of higher order modes from the aperture to ensure that only the propagating TE_{10} mode will be incident on the aperture. The direction of the arrow in figure 3.2 shows the direction of propagation for the TE_{10} mode.

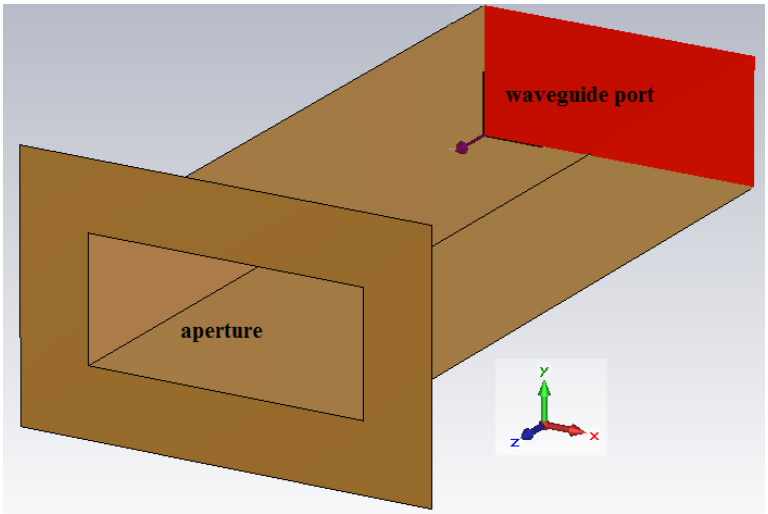

Figure 3.2: CST model of the waveguide excited by a matched waveguide port.

Figure 3.3 shows the distribution of the mode generated by the waveguide port as a cosine distribution across the horizontal dimension of the waveguide aperture in volts/meter (V/m). This is the expected mode distribution for the TE_{10} mode [25]. The mode distribution peaks and is symmetric about $x = 0$ and $y = 0$. The mode distribution does not vary in the $\underline{\mathbf{z}}_o$ direction because it is a propagating mode and not an evanescent (attenuating) mode.

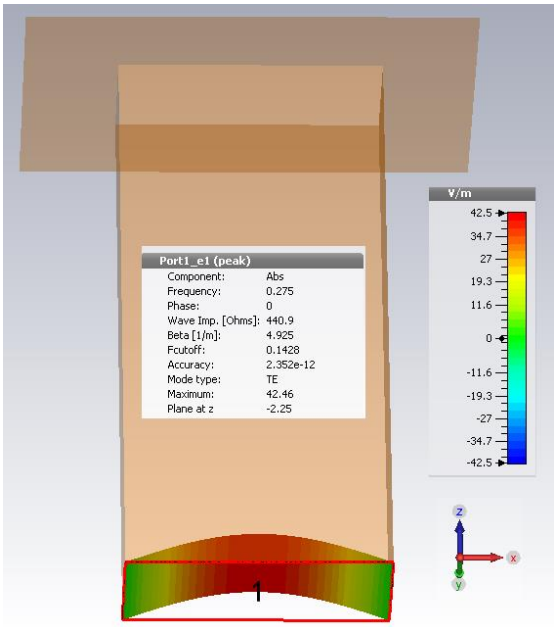

Figure 3.3: The cosine TE_{10} mode electric field distribution in the waveguide.

We show a novel method in appendix D to determine the Fourier transform of the electric field at the aperture for a TE_{10} mode incident on that aperture. We achieve this via what we call the modal decomposition matrix (MDM) method, which numerically solves the following system of equations in matrix form

$$(1+\Gamma''_N)\underline{e}''_N(x,y)+\sum_{M\neq N}\left[\Gamma''_M\,\underline{e}''_M(x,y)+\Gamma'_M\,\underline{e}'_M(x,y)\right]= \frac{1}{(2\pi)^2}\int_{-\infty}^{+\infty}\int_{-\infty}^{+\infty}\underline{\tilde{E}}(k_x,k_y)e^{-j\underline{k}_T\bullet\underline{\rho}}dk_xdk_y \quad , \tag{3.2a}$$

$$(1-\Gamma''_N)\frac{\underline{h}''_N(x,y)}{Z''_N}-\sum_{M\neq N}\left[\Gamma''_M\frac{\underline{h}''_M(x,y)}{Z''_M}+\Gamma'_N\frac{\underline{h}'_M(x,y)}{Z'_M}\Gamma'_M\right]= \frac{1}{(2\pi)^2}\int_{+\infty}^{+\infty}\int_{+\infty}^{+\infty}\underline{\tilde{H}}(k_x,k_y)e^{-j\underline{k}_T\bullet\underline{\rho}}dk_xdk_y \quad , \tag{3.2b}$$

where $\underline{e}'_N$ and $\underline{h}'_N$ are the TM mode functions of the electric and magnetic fields in the rectangular waveguide respectively, while $\underline{e}''_M$ and $\underline{h}''_M$ are the TE mode functions. N

denotes the incident mode number, M denotes all non-incident mode numbers, $\underline{k}_T = k_x \cdot \underline{x}_o + k_y \cdot \underline{y}_o$, $\underline{\rho} = x \cdot \underline{x}_o + y \cdot \underline{y}_o$, Γ is the reflection coefficient at the aperture, Z' is the TM mode guide impedance, and Z'' is the TE guide impedance. The non-incident modes are generated by the reflection of the incident mode at the aperture. We fully drive and define the mode functions in appendix D as equations D.2a through D.2d, and we also define the equations for the guide impedances as equations D.6a and D.6b. We simplify equations 3.2a and3.2b by introducing the following identities

$$\iint_S \underline{\chi}_k(x,y) \bullet \underline{\chi}_l(x,y)\,dxdy = \delta_{kl}\,, \tag{3.3a}$$

$$\hat{\underline{\tau}}_\upsilon(\underline{k}_T) = \iint_S \frac{e^{-j\underline{k}_T \bullet \underline{\rho}}}{(2\pi)^2} \underline{\tau}_\upsilon(x,y)\,dxdy\,, \tag{3.3b}$$

$$\left(\hat{\underline{\tau}}_\upsilon(k_x,k_y),\, \tilde{\underline{r}}_T(k_x,k_y)\right) = \int_{+\infty}^{+\infty}\int_{+\infty}^{+\infty} \hat{\underline{\tau}}_\upsilon(k_x,k_y) \bullet \tilde{\underline{r}}_T(k_x,k_y) e^{-j\underline{k}_T \bullet \underline{\rho}}\,dk_x dk_y\,. \tag{3.3c}$$

Using the identities defined by equations 3.3a through 3.3c we rewrite equations 3.2a and 3.2b as a system of equations

$$\left(\hat{\underline{e}}''_\upsilon(k_x,k_y),\, \tilde{\underline{E}}_T(k_x,k_y)\right) + Z''_\upsilon\left(\underline{h}''_\upsilon(k_x,k_y),\, \tilde{\underline{H}}_T(k_x,k_y)\right) = 2\delta_{\upsilon N}\,, \tag{3.4a}$$

$$\left(\hat{\underline{e}}'_\upsilon(k_x,k_y),\, \tilde{\underline{E}}_T(k_x,k_y)\right) + Z'_\upsilon\left(\underline{h}'_\upsilon(k_x,k_y),\, \tilde{\underline{H}}_T(k_x,k_y)\right) = 2\delta_{\upsilon N}\,. \tag{3.4b}$$

We present a full derivation of these equations and the behavior of the modal fields in appendix D. The solution to the system of equations in equations 3.4a and 3.4b assumes an incident TE_{10} mode at the aperture, and a $\lambda_o/2$ resonance established by equation 3.1. Figure 3.4 and figure 3.5 show comparisons between the radiation patterns at 300 MHz. The red curve represents the MDM calculation, and the blue curve

represents the simulation of the model in figure 3.2 using CST Studio Suite 2014. These results show excellent agreement between the MDM method and simulation.

We can explain the small differences between calculation and simulation in figure 3.4 and figure 3.5 by the resolution of the MDM. We generated these results using the first 20 mode indices to populate the MDM. The number of modes used in the MDM directly affects the resolution in the far field radiation pattern. For example, if we only use the first 3 modes then we would only have 3 points in our radiation pattern which would yield a very poor discretization of the true radiation pattern. If we continue to increase the number of modes we use in the calculation, then the calculated radiation pattern asymptotically converges to that of the simulation. The results in figure 3.4 and figure 3.5 use 20 modes in the MDM method. If the reader desires a more in depth understanding of the MDM method, we encourage them to reference appendix D as we will not go into further discussion here.

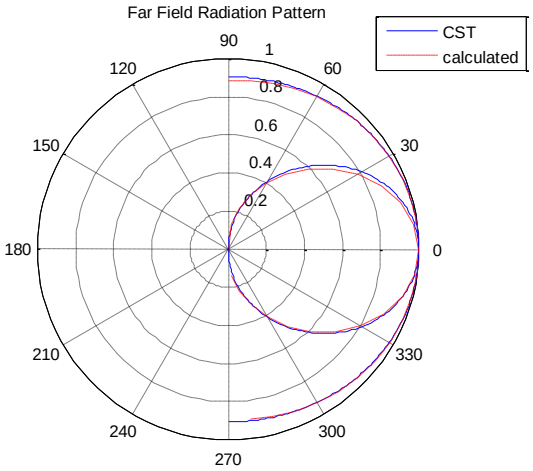

Figure 3.4: Polar plot of the normalized far field E_θ and E_ϕ radiation patterns.

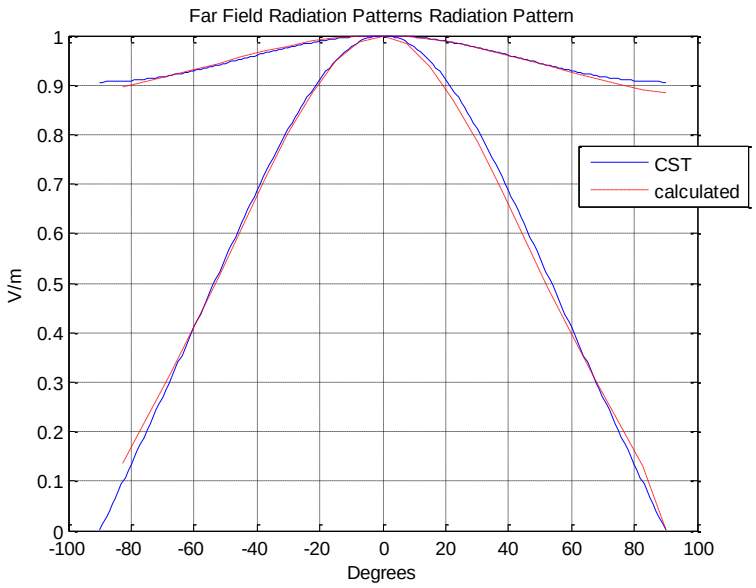

Figure 3.5: Linear plot of the normalized far field E_θ and E_ϕ radiation patterns.

3.2 Air Filled Cavity Stimulated by a Flat Rectangular Probe

Traditional air-filled rectangular waveguides achieve broadband performance via a CWT which terminates in a matching network. This CWT has been widely studied, and many successful methods have been developed. Generally a coaxial input is terminated in the middle of the PEC boundary of the widest transverse waveguide dimension. A length of the coaxial line's inner conductor extends into the waveguide to stimulate the dominant mode and tune the impedance of the waveguide to the characteristic impedance of the coaxial cable input [2].

When the waveguide is terminated in a shorted reflector, then the electrical height between the matching network and the short is approximately $\lambda_g/4$ at the center frequency, where λ_g is

$$\lambda_g = \frac{\lambda_{o,cf}}{\sqrt{\mu_r \varepsilon_r - \left(\frac{\lambda_{o,cf}}{2a}\right)^2}}, \tag{3.5}$$

and $\lambda_{o,cf}$ is λ_o at the center frequency of the band [1], [2], [17].

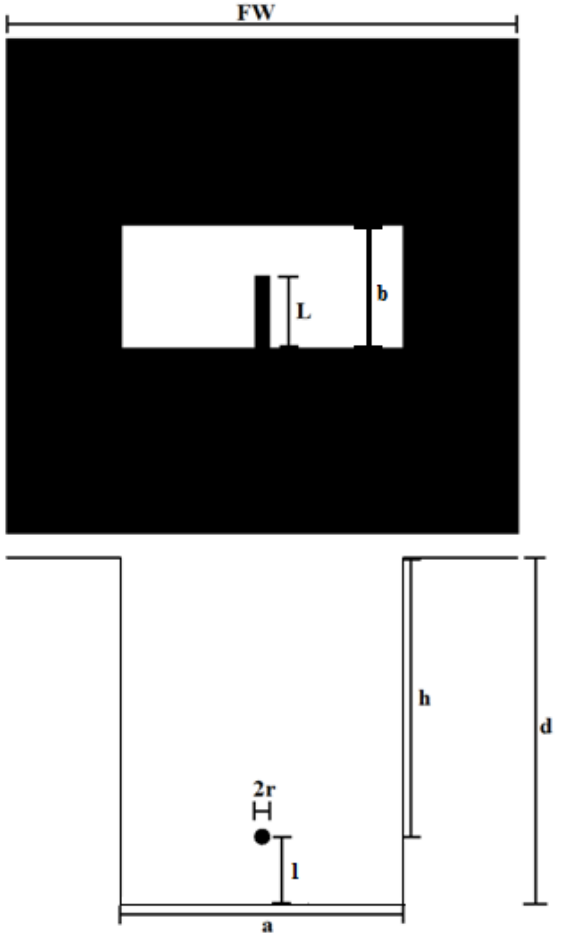

Figure 3.6: Geometry of a radiating waveguide based on Wade's CWT [1].

Table 3.1: Normalized dimensions for the model shown in figure 3.6 scaled by λ_o.

a	***b***	***l***	***h***	***d***	***r***	***L***	***FW***
$0.5\lambda_o$	$0.22\lambda_o$	$0.12\lambda_o$	$0.49\lambda_o$	$0.61\lambda_o$	$0.014\lambda_o$	$0.13\lambda_o$	$0.91\lambda_o$

The placement of the short at z = $\lambda_g/4$ produces a reflection phase at the aperture such that the reflected wave and radiated wave add constructively at the radiation

boundary. This should double the amount of radiated power to boresight ($\phi = 90^o$), but this creates a narrowband solution since λ_g varies with frequency. This technique also has the disadvantage of increasing the profile of the antenna in the direction perpendicular to the aperture by $\lambda_g/4$.

In section 2.1, we review traditional CWTs as determined by Collin and Wade; however, none of these CWTs give us an intuition as to how they would act as a standalone radiating element. By scaling the dimensions of the Wade study for a WR90 type adapter to a frequency of 200 MHz, and using a $0.61\lambda_o$ length of waveguide with a large flange, we arrive at the model shown in figure 3.6 with dimensions listed in table 3.1.

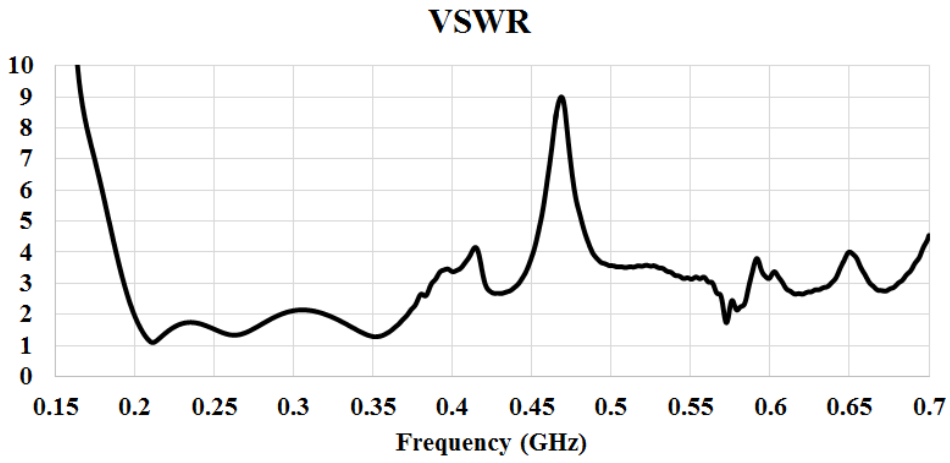

Figure 3.7: VSWR of a radiating waveguide with $\lambda_o = 1.94$ m.

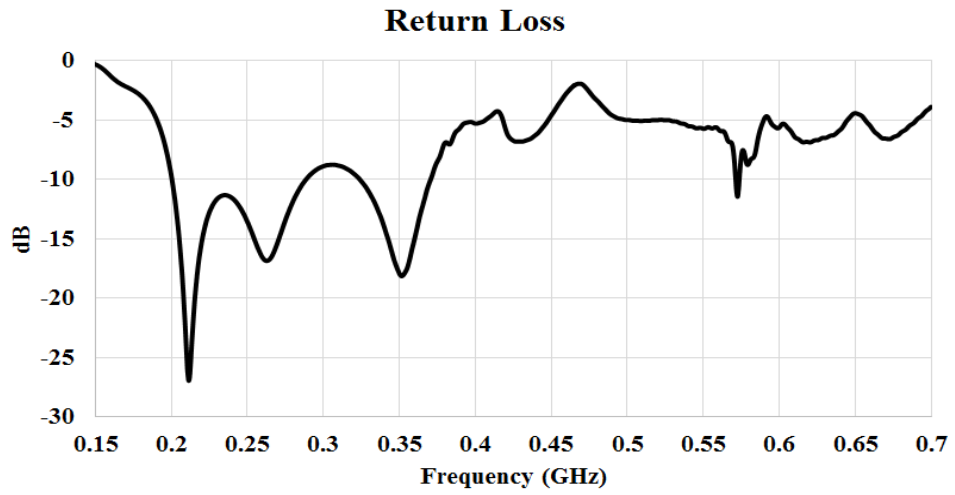

Figure 3.8: Return loss of a radiating waveguide with λ_o = 1.94 m.

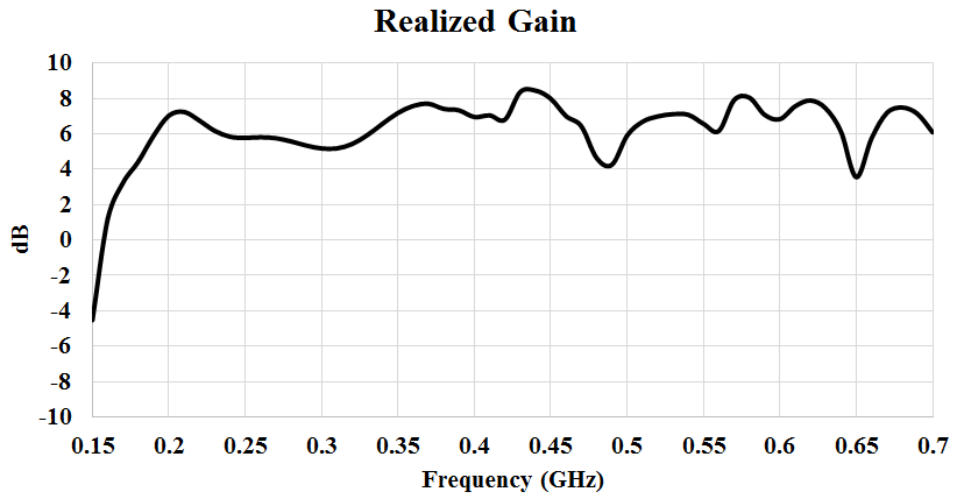

Figure 3.9: Realized gain of the radiating waveguide with λ_o = 1.94 m.

Figure 3.7 and figure 3.8 show that for λ_o=1.94 m, we see an impedance match with a VSWR of better than 2:1 and a return loss of better than -10 dB over 0.46 octaves of bandwidth. Furthermore, we see a VSWR of better than 2.2 over 0.86 octaves of bandwidth. This bandwidth resembles the 0.79 octave bandwidth Wade describes for his CWT terminating in a matched load [1]. Figure 3.9 shows a very good realized gain of 4.0 dB to 7.75 dB over this bandwidth, and figure 3.10 shows the radiation pattern of the

antenna at the center frequency of 280 MHz. This radiation pattern shows a typical dipole pattern as expected for the cosine distribution of the electric field at the aperture. The peak realized gain of the radiation pattern is 5.8 dB at bore sight.

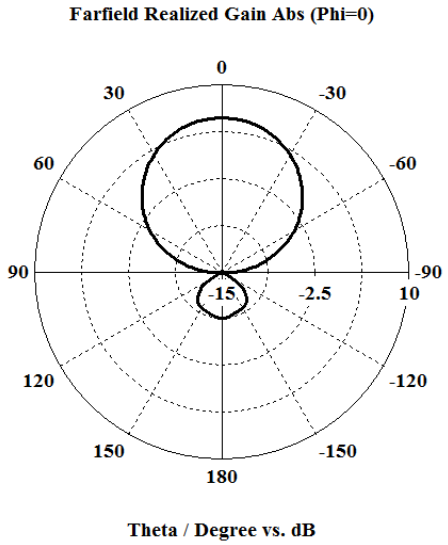

Figure 3.10: Radiation pattern at 280 MHz of the radiating waveguide with λ_o = 1.94 m.

These results show that using a traditional CWT serves as a good feed and matching network for a radiating waveguide. However, a profile of $d = 0.61\lambda_o$ is more than 10 times larger than our goal of $d = 0.05\lambda_o$. The large profile is mainly due to the large *h* dimension from the right of the probe to the aperture; however our backshort is still contributing 20% of the profile height. This design also requires a very large flange defined by *FW*, which makes this an impractical design at low UHF frequencies.

Now we wish to reduce the profile *d* while maintaining or improving the 0.86 octave bandwidth of the radiating waveguide in figure 3.6. We accomplish the reduction in *d* by placing the probe matching network as close to the aperture as possible while still maintaining a good impedance match. We also replace the standard cylindrical probe matching network with a thin rectangular probe using a probe height in the normal

direction of T = 2 mm. Figure 3.11a and figure 3.11b show to-scale diagrams of the new flat probe LPA (FLPA) design versus the radiating waveguide of figure 3.6. We give the normalized dimensions of the FLPA in table 3.2.

The new placement of the thin rectangular probe allows further reduction of h to $0.015\lambda_o$. This is a 96.3% reduction compared to the radiating waveguide utilizing the standard cylindrical CWT matching network. This reduction results in an antenna with a total profile of $d = 0.14\lambda_o$. This is still roughly 3 times larger than our goal of $d = 0.05\lambda_o$, but we achieve a significant profile reduction of 77.0% over a typical radiating waveguide.

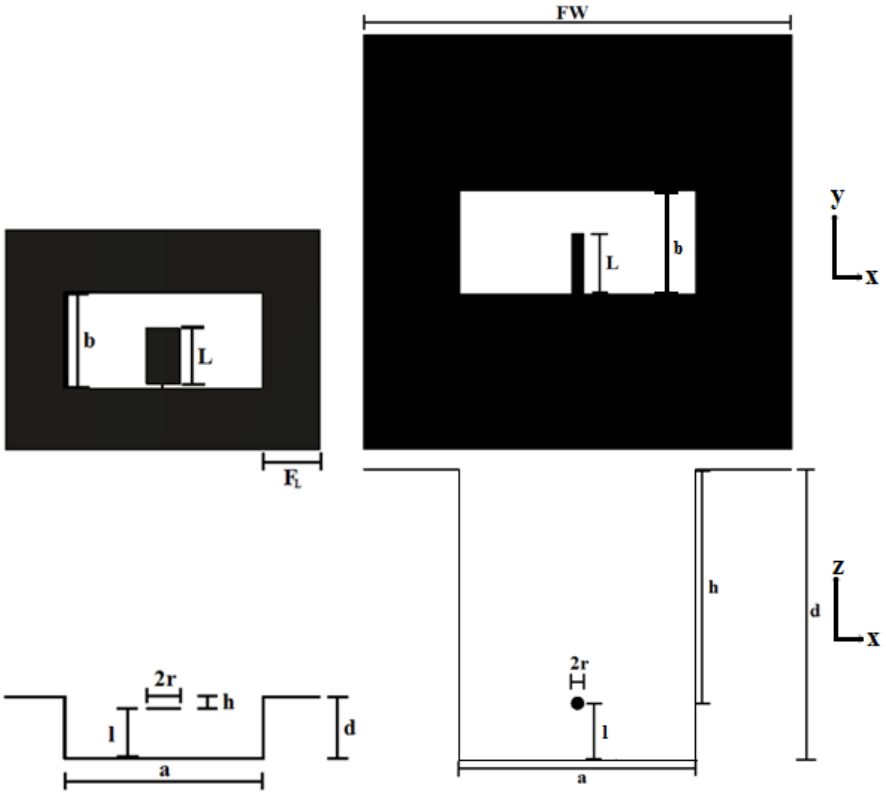

Figure 3.11: To-scale diagram of the antenna profile in the normal direction. (a) FLPA. (b) Radiating waveguide.

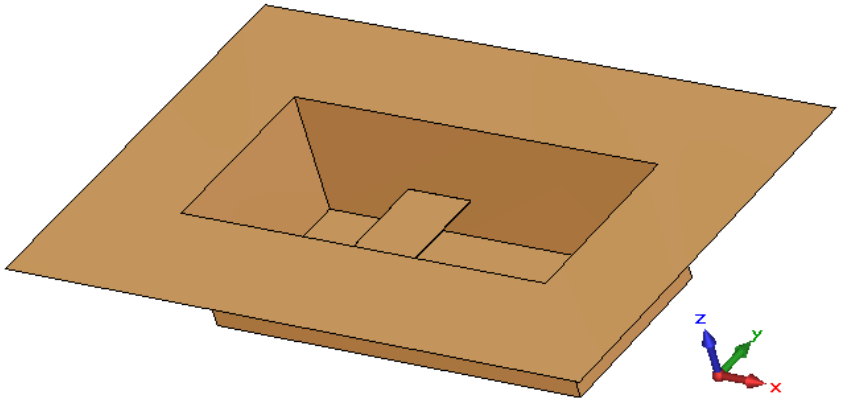

Figure 3.12: CST model of FLPA design with λ_o = 1.56 m.

Table 3.2: Normalized dimensions of the geometry in figure 3.11a scaled to λ_o.

l	***a***	***b***	***r***	***L***	***h***	***d***	F_L
$0.122\lambda_o$	$0.5\lambda_o$	$0.22\lambda_o$	$0.043\lambda_o$	$0.133\lambda_o$	$0.015\lambda_o$	$0.14\lambda_o$	$0.143\lambda_o$

Figure 3.12 shows the CST model we use in the simulation of our FLPA design. This model uses λ_o = 1.56 m following the normalized dimensions given in table 3.2. We do not normalize T to λ_o because the thickness of the probe will not scale with frequency. We re-optimize L and r to provide the best impedance match at the coaxial input.

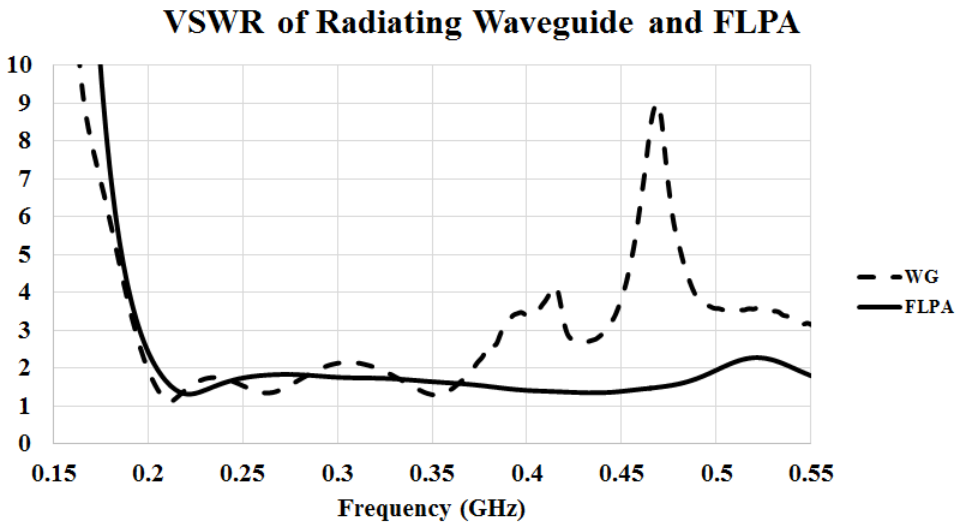

Figure 3.13: VSWR of the radiating waveguide and the FLPA.

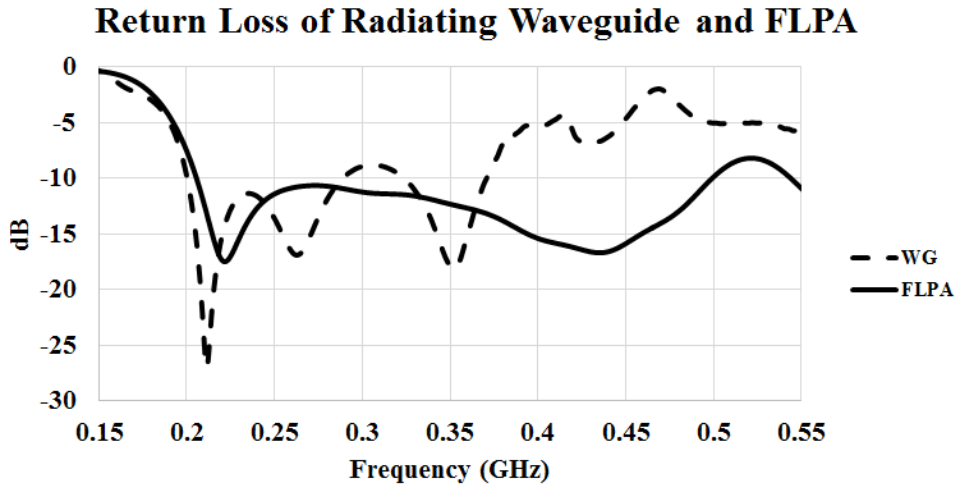

Figure 3.14: Return loss of the radiating waveguide and the FLPA.

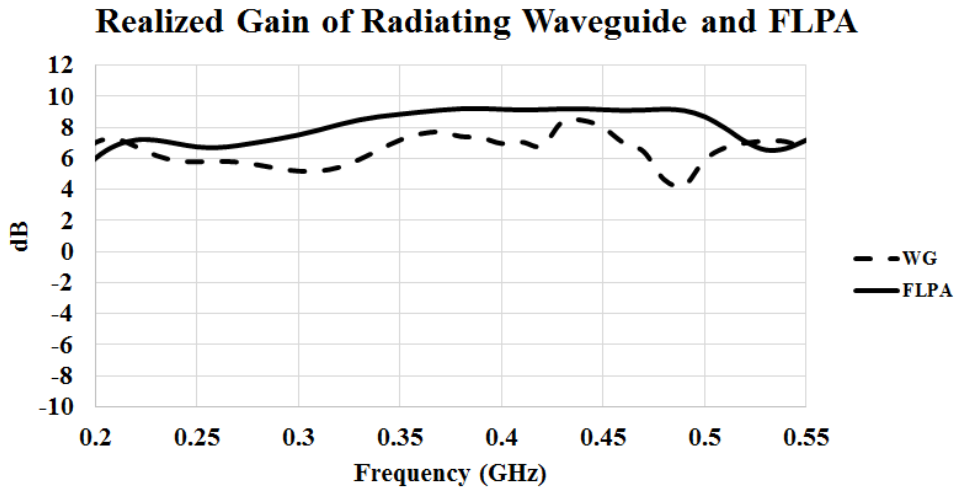

Figure 3.15: Realized gain of the radiating waveguide and the FLPA.

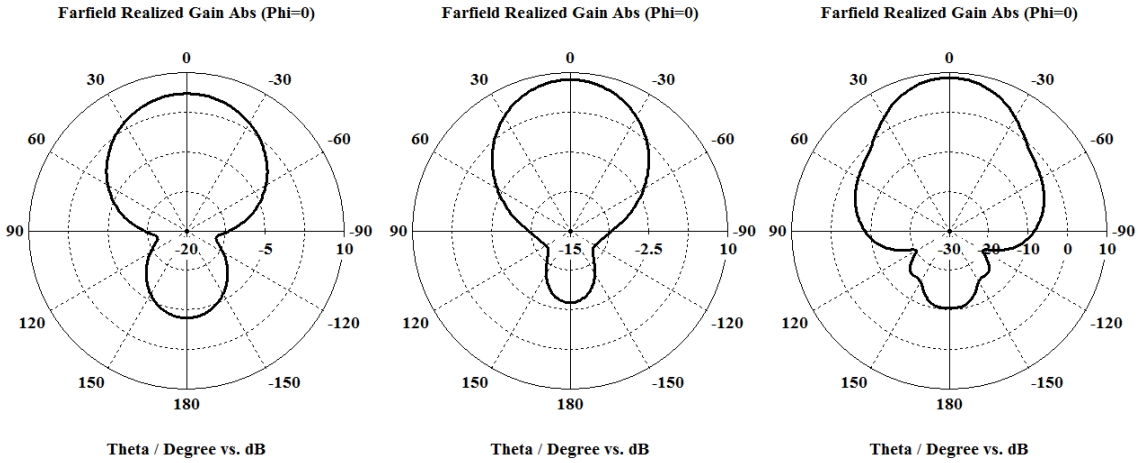

(a) (b) (c)

Figure 3.16: Polar plots of the far field radiation patterns of the FLPA. (a) 200 MHz. (b) 350 MHz. (c) 500 MHz.

Figure 3.13 through figure 3.15 show that for λ_o = 1.5 m, the dimensions given in table 3.2 achieve a VSWR of less than 2:1 over 1.44 octaves of bandwidth with a realized gain ranging from 6.0 dB to 9.0 dB. The return loss is better than -10 dB over this entire bandwidth. The total profile of this design is $d = 0.14\lambda_o$ which is a 77.0% reduction from the profile of the radiating waveguide. Figure 3.16a through figure 3.16c show the

radiation plots at $\phi = 0^o$ across the bandwidth at 200 MHz, 350 MHz, and 500 MHz. These plots achieve peak realized gain values at bore sight of 6.02 dB, 8.86 dB, and 8.69 dB respectively.

These results demonstrate that using a wide, rectangular probe as the matching network provides better impedance match than the traditional CWT while significantly reducing the cavity profile over a radiating waveguide. Table 3.3 shows that the FLPA performs better than any of the other state of the art antennas except for the cavity backed spiral. However, since this design still uses an air-filled cavity, the cavity profile *d* remains too large. We want to investigate how loading the cavity with a high index medium to reduce λ_o affects the performance of the FLPA.

Table 3.3: Comparison of FLPA to state of the art wideband LPA designs.

reference	Aperture	substrate	BW (octaves)	gain (dB)	profile (λ_o)
[17]	spiral	dielectric	7.3	-2.6 - 6.9	0.03
[18]	Inverted L	dielectric	0.59	-	0.09
[19]	Bowtie	dielectric	0.77	4.0 - 6.0	0.064
[20]	Discone	none	0.92	-	0.09
[21]	Monopole	HIS/EBG	0.77	7.0 - 10.25	0.1
[22]	Bowtie	HIS/EBG	1.07	3.3 - 9.35	0.05
[23]	dipole	HIS/EBG	0.41	-	0.06
-	FLPA	none	1.44	4.8 - 8.2	0.14

3.3 Cavity Loaded with High Index Dielectric

Since λ_o scales not only with frequency but also with the refractive index of the medium, this indicates that increasing ε_r and/or μ_r reduces the value of λ_o. Reducing λ_o serves to reduce the largest factor in the determination of the cavity profile for the model of figure 3.11a. Replacing the air-filled cavity with a high index dielectric, ferrite, or magneto-dielectric medium reduces *d* by a factor on the order of $n = (\mu_r\varepsilon_r)^{0.5}$, where *n* is

the index of refraction of the medium. However, equation 3.1 tells us that increasing ε_r and/or μ_r also reduces the frequency at which multiple resonances will exist inside the cavity. Generally speaking, many resonances will make obtaining an impedance match at the coaxial input very difficult. To demonstrate this effect, we use CST Studio Suite to show the degradation in the performance of the antenna due to these high order resonances.

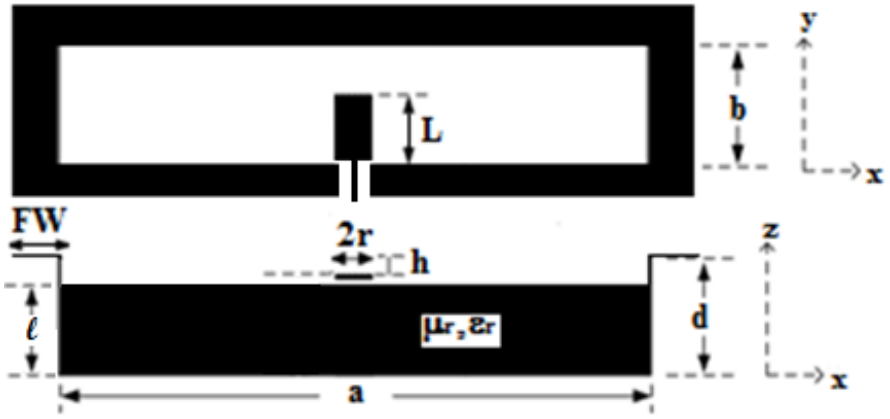

Figure 3.17: The geometry of the FLPA backshort loaded with a high index medium.

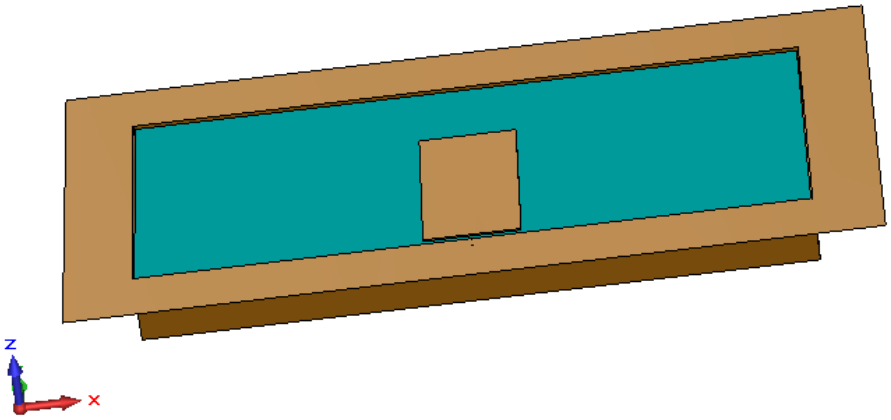

Figure 3.18: CST model of loaded FLPA.

Figure 3.17 shows a rectangular cavity loaded with a high index dielectric material with $\mu_r = 1$ and $\varepsilon_r = 10$. Table 3.4 shows the normalized dimensions of this design. The

introduction of the dielectric material has reduced the total profile of the design to $d = 0.053\lambda_o$. We eliminate the distance of the probe to the aperture, *h*, by placing the probe directly at the aperture of the open cavity. The dimension *h* is now defined by the radius of the outer conductor of our coaxial line. We do this to minimize the profile of the antenna as much as possible.

Table 3.4: Normalized dimensions for the simulations run for geometry in figure 3.17.

l	***a***	***b***	***r***	***L***	***h***	***d***
$0.05\lambda_o$	$\lambda_o/2$	$\lambda_o/4.5$	$0.036\lambda_o$	$0.144\lambda_o$	$0.002\lambda_o$	$0.053\lambda_o$

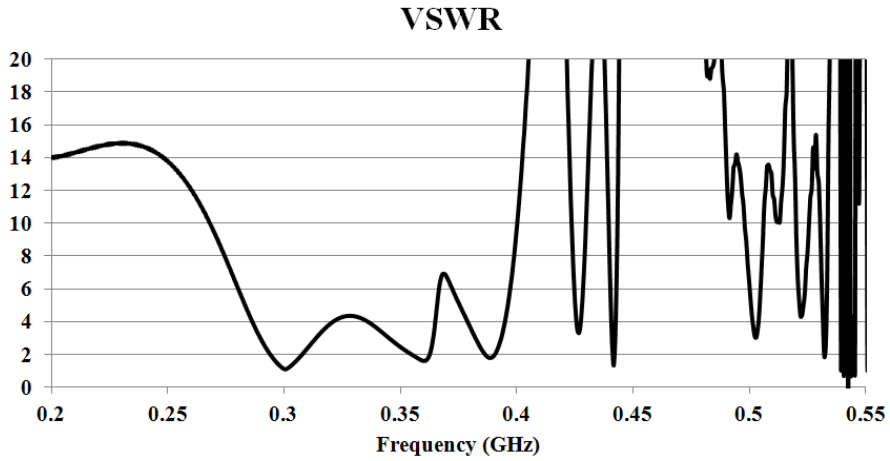

Figure 3.19: VSWR of the loaded FLPA.

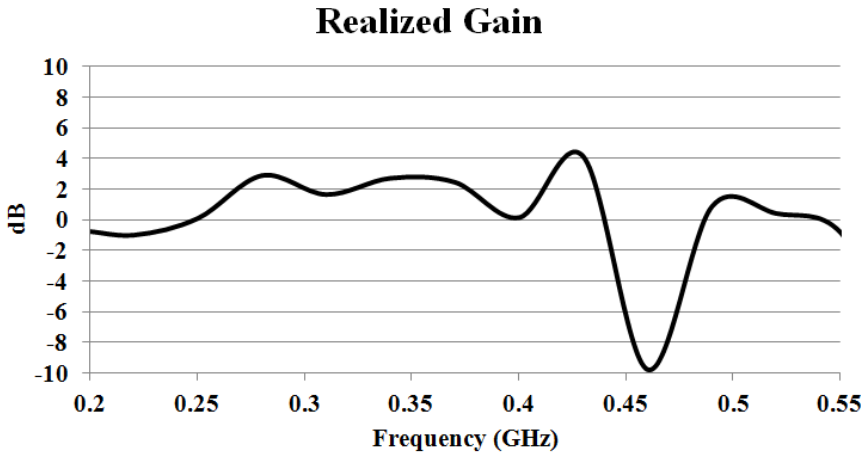

Figure 3.20: Realized gain of the loaded FLPA.

Figure 3.18 shows the CST model we use to generate the results of figure 3.19 and figure 3.20. Figure 3.19 and figure 3.20 show that for λ_o = 1.5 m, the dimensions given in table 3.4 achieve an unusable VSWR over much of the 200 MHz to 500 MHz bandwidth due to destructive interference from multiple resonances existing in the cavity. This destructive interference also shows itself in the realized gain which regularly drops well below 0 dB. The total profile of this design is $d = 0.053\lambda_o$ which is a 71.8% reduction from the design using flat rectangular probe. This demonstrates the ability to significantly reduce the profile of the antenna by loading the rectangular cavity with a high index material. The nature of the VSWR indicates that there are multiple resonances interfering destructively. Since new resonances appear at intervals of $2f_r$, this means that every 63.25 MHz a new resonance appears in the cavity. Therefore, at 200 MHz up to 3 resonances coexist inside the rectangular cavity and at 500 MHz there are as many as 7 resonances coexisting.

Chapter 4
Low Profile Antenna (LPA) Design Incorporating an Isotropic Transverse Resonance Formulation

This chapter investigates the performance of a partially loaded radiating rectangular cavities. First, we derive the isotropic transverse resonance condition for a partially loaded rectangular cavity with a high index medium. The high index medium incorporates a novel linear taper that provides a smooth transition from free space impedance to that of a fully loaded rectangular cavity. We derive a novel cavity shape tailored to the taper in the medium which maintains a constant resonant frequency within the cavity. Then we detail a symmetric, balanced two-port feed which provides a flat wideband impedance match for our radiating cavity. We show that this tapered cavity design results in a dielectric LPA model achieving 0.53 octaves of bandwidth with positive realized gain with a 67.5% reduction in electrical height over the FLPA of chapter 3. Finally we present a brief investigation of how partially loading the cavity with lossless ferrite material affects the performance of the LPA and the shape of the tapered cavity. This investigation is purely theoretical as no such material currently exists.

4.1 Isotropic Transverse Resonance of a Partially Loaded Parallel Plate Waveguide

We wish to determine the exact geometry of a partially loaded rectangular cavity with the goal to maintain a constant resonance frequency. To do this, we will maintain a $\lambda_{eff}/2$ separation between the walls of the cavity, where is the effective wavelength in the horizontal cavity dimension. We believe this will alleviate the multiple resonances that degrade our VSWR in figure 3.19. For our design the dimensions of the cavity at the

aperture will be $\lambda_o/2$ in free space because our cavity is radiating into free space. To maintain a constant transition in impedance, we will assume utilize a linear taper in the width of the high index medium we use to load the cavity. We show an approximation to this geometry in figure 4.1. Here $a_0 = \lambda_o/2$, $a_1 = a_0/(\varepsilon_r\mu_r)^{0.5}$, and $a(z) = \lambda_{eff}(z)/2 = L_g(z) + w(z)$. Therefore, a_0 represents a half wavelength in free space and a_1 represents a half wavelength in a fully loaded cavity. The linear taper in the width of the material, $w(z)$, ensures a smooth impedance transition from $z = 0$ to $z = -d$, where d is the depth of the cavity. Therefore, $w(z) = 0$ at the aperture and $w(z) = a_1$ at the backshort. The vertical dimension, b, remains constant with z. Since all dimensions apart from $L_g(z)$ are known based on the index of the medium and the desired frequency of resonance, the goal of this section is to determine the relationship between L_g and w that maintains a $\lambda_{eff}/2$ separation between the cavity walls in the horizontal direction.

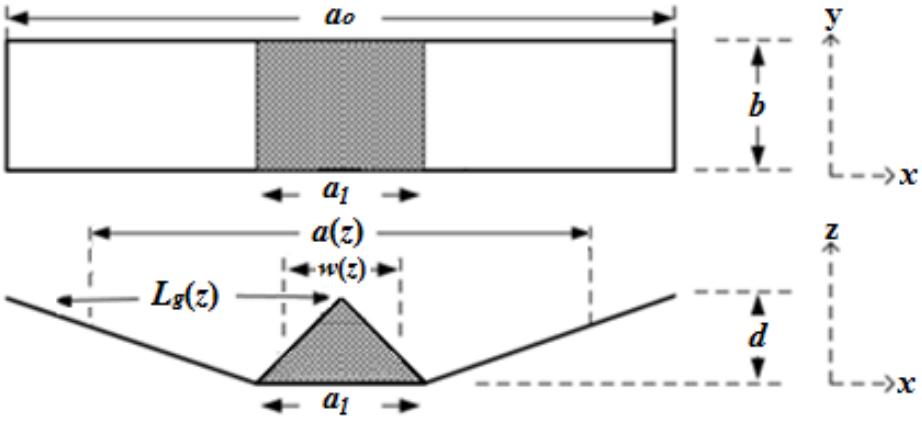

Figure 4.1: Top view and side view of a symmetrically loaded, tapered radiating rectangular cavity.

If we assume a linear taper in the width of the high index medium, $w(z)$, then at any depth z in the cavity, we can represent the horizontal distance in the cavity as a

partially filled parallel plate transmission line as in figure 4.1. We determine the shape of the rectangular cavity by determining the value of $L_g(z)$ for a given width of material *w(z)*, which changes linearly as the rectangular cavity depth increases as in figure 4.1. We calculate $L_g(z)$ as the unknown distance between the edge of the high index medium and the cavity wall based on a transverse resonance condition in the $\underline{\boldsymbol{x}}_o$-direction. We know that $a(z)$ will also change with $w(z)$, and the transverse resonance also determines the shape of the taper in $a(z)$.

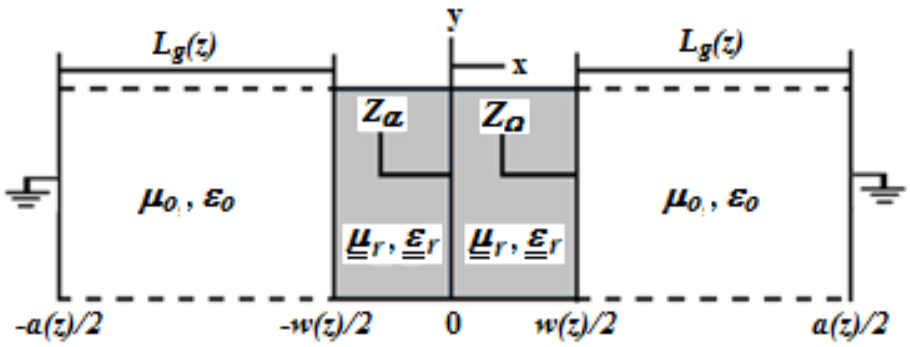

Figure 4.2: Shorted transmission line model of a symmetrically loaded rectangular cavity.

We can suppress propagation in the vertical dimension of the cavity at resonance if $a_0 > 2b$ [3]. If we assume a linear taper in $w(z)$, then at any depth z in the cavity, we can represent the horizontal distance in the cavity as a partially filled parallel plate transmission line as in figure 4.2. We calculate $L_g(z)$ as the unknown distance between the edge of the high index medium and the cavity wall based on a transverse resonance condition in the $\underline{\boldsymbol{x}}_o$-direction. The transverse resonance condition is [3]

$$\vec{Z}_{in} + \bar{Z}_{in} = 0\,, \tag{4.1}$$

where $\vec{Z}_{in}$ is the input impedance looking in from the left and $\overleftarrow{Z}_{in}$ is the input impedance looking from the right. To maintain a constant resonance in the horizontal direction, equation 4.1 must hold at every point x across the cavity. However, if we define the transverse resonance at $x = 0$ in figure 4.2, the condition simplifies to

$$2\vec{Z}_{in} = 0, \tag{4.2}$$

because the symmetry of figure 4.2 ensures that $\vec{Z}_{in} = \overleftarrow{Z}_{in}$ at $x = 0$.

Since we suppress propagation in the vertical dimension based on the relationship between a_0 and b, we set $k_y = 0$ m^{-1}. Similarly, we know at resonance that the following about the fields in the normal dimension $E_z = 0$ V/m, $k_z = 0$ m^{-1} based on waveguide theory [3]. Here E_z is the electric field in the normal direction while k_z and k_y are the propagation constants in the $\underline{\boldsymbol{z}}_o$- or $\underline{\boldsymbol{y}}_o$-directions respectively. With this in mind, we can begin our calculation of $L_g(z)$ versus $w(z)$.

We begin with the time harmonic Maxwell's equations in a source free medium

$$\nabla x\underline{E} = -j\omega\mu_o\mu_r\underline{H}, \tag{4.3a}$$

$$\nabla x\underline{H} = j\omega\varepsilon_o\varepsilon_r\underline{E}, \tag{4.3b}$$

where $\underline{E}$ and $\underline{H}$ are the electric and magnetic fields respectively. Taking the curl of both sides of equation 4.3a and substituting the right hand side of equation 4.3b yields the following differential equation for $\underline{E}$

$$\nabla^2\underline{E} + \omega^2\varepsilon\mu\underline{E} = 0. \tag{4.4}$$

This is known as the wave equation for $\underline{E}$. Similarly, taking the curl of equation 4.3b and substituting the right hand side of equation 4.3a yields the wave equation for $\underline{H}$ as

$$\nabla^2 \underline{H} + \omega^2 \varepsilon \mu \underline{H} = 0 . \tag{4.5}$$

Looking only at the $\underline{\mathbf{z}}_o$ component of equations 4.4 and 4.5, and keeping in mind that we set $E_z = 0$ at first resonance we arrive at a single equation for H_z

$$\nabla^2 H_z + \omega^2 \varepsilon \mu H_z = 0 . \tag{4.6}$$

Furthermore, with $k_y = 0$ and $k_z = 0$, there is no variation in the $\underline{\mathbf{y}}_o$- or $\underline{\mathbf{z}}_o$-direction. This simplifies equation 4.6 to the wave equation for H_z in the two regions

$$\left(d^2/dx^2 + k_o^2\right) H_{z0} = 0, \quad \begin{cases} -a/2 \le x \le -w/2 \\ w/2 \le x \le a/2 \end{cases}, \tag{4.7a}$$

$$\left(d^2/dx^2 + k_o^2 \varepsilon_r \mu_r\right) H_{z1} = 0, \quad -w/2 \le x \le w/2 , \tag{4.7b}$$

$$k_o = \omega \sqrt{\varepsilon_o \mu_o} \tag{4.8}$$

where k_o is the wave number in free space, and H_{z0} and H_{z1} are the $\underline{\mathbf{z}}_o$-component of the magnetic field in the free space and isotropic regions respectively.

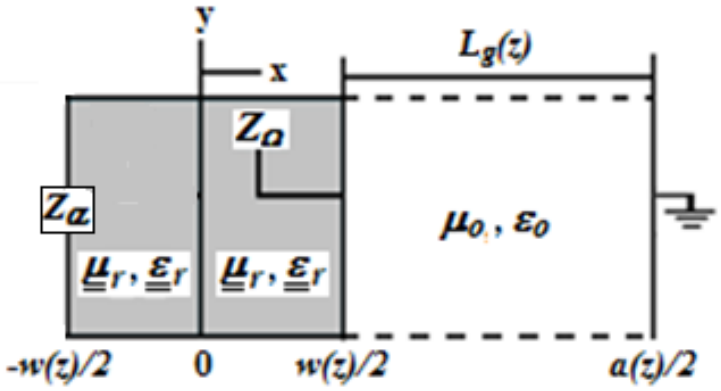

Figure 4.3: Transformed transmission line model of figure 4.2.

We know from transmission line theory, we know that we can transform the input impedance from the short in figure 4.2 at $x = a/2$ to the boundary at $x = -w/2$ by the following equation [3]

$$Z_{in}^{\alpha}\left(x=-w/2\right)=jZ_o\tan\left(\beta_o L_g\right), \tag{4.9}$$

where $Z_o=\sqrt{\mu_o/\varepsilon_o}$ is the characteristic impedance of the transmission line in region 0 and $\beta_o = k_o$ comes directly from equation 4.7a. This simplifies figure 4.2 to the transmission line model of figure 4.3. We now need to transform the load impedance from at $x = -w/2$ to $x = 0$ using the following equation for input impedance from Pozar [3]

$$Z_{in}=Z_c\frac{Z_L+jZ_c\tan\left(\beta l\right)}{Z_c+jZ_L\tan\left(\beta l\right)}, \tag{4.10}$$

where Z_c is the characteristic impedance of the line, Z_L is the load impedance, β is the propagation constant in the direction of propagation, and l is the distance between Z_c and Z_L. Substituting the appropriate values from figure 4.3 into equation 4.10 yields

$$Z_{in}^{\Omega}\left(x=0\right)=Z_1\frac{Z_{in}^{\alpha}+jZ_1\tan\left[\beta_1\left(w/2\right)\right]}{Z_1+jZ_{in}^{\alpha}\tan\left[\beta_1\left(w/2\right)\right]}, \tag{4.11}$$

where $Z_1=Z_o\sqrt{\mu_r/\varepsilon_r}$ is the characteristic impedance of the high index medium and $\beta_1 = k_o\sqrt{\varepsilon_r\mu_r}$ comes directly from equation 4.7b.

By the symmetry that exists around $x = 0$, the transverse resonance condition of equation 4.2 can be written equivalently as $2Y_{in}^{\Omega}=0$ where $Y_{in}^{\Omega}=1/Z_{in}^{\Omega}$ is the input admittance at $x = 0$. At this point, we plug equation 4.9 into equation 4.11, and we solve for the $L_g(z)$ that satisfies $2Y_{in}^{\Omega}=0$ by setting the denominator of equation 4.11 to zero

$$0=Z_o\sqrt{\mu_r/\varepsilon_r}+jjZ_o\tan\left(\beta_o L_g\right)\tan\left[k_o\sqrt{\mu_r\varepsilon_r}\left(w/2\right)\right],$$

which simplifies to

$$0 = \sqrt{\mu_r/\varepsilon_r} - \tan\left(k_o L_g\right)\tan\left[k_o\sqrt{\mu_r\varepsilon_r}\,(w/2)\right]. \tag{4.12}$$

Substituting $k_o = 2\pi / \lambda_o$ yields

$$\sqrt{\mu_r/\varepsilon_r} = \tan\left(\frac{2\pi}{\lambda_o}L_g\right)\tan\left[\frac{\pi w}{\lambda_o}\sqrt{\mu_r\varepsilon_r}\right]. \tag{4.13}$$

Finally, taking the inverse tangent of both sides of equation 4.13 and solving for L_g / λ_o yields the final equation for L_g versus w normalized by λ_o

$$\frac{L_g(z)}{\lambda_o} = \frac{1}{2\pi}\tan^{-1}\left[\frac{\sqrt{\mu_r/\varepsilon_r}}{\tan\left(\pi\sqrt{\mu_r\varepsilon_r}\,w/\lambda_o\right)}\right]. \tag{4.14}$$

Equation 4.14 is the unique equation that gives us the shape of our tapered cavity. A cavity based on this equation will guarantee the suppression of high order resonances within the cavity over an octave of bandwidth.

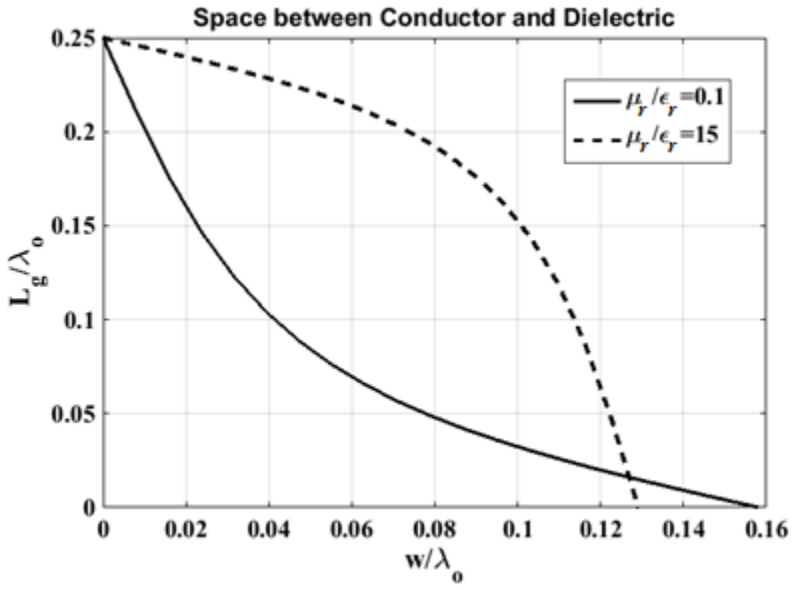

Figure 4.4: Normalized L_g/λ_o vs. w/λ_o curves for different ratios of μ_r/ε_r.

Figure 4.4 plots the relationship of L_g/λ_o versus w/λ_o for different ratios of μ_r/ε_r. The cavity taper has an inverse-like relationship for when the ratio is positive versus

when the ratio is negative. This stems directly from the numerator of equation 4.14. Furthermore, if the ratio is unity then the cavity taper is linear. If both $\mu_r = 1$ and $\varepsilon_r = 1$, then the model resembles figure 3.11a, and this represents a free-space medium. Furthermore, figure 4.4 shows that at the aperture of the cavity when $w(z) = 0$, then $L_g(z) = \lambda_o / 4$, which makes sense because $L_g(z)$ represents the distance from $x = 0$ to $x = a_0 / 2$ in figure 4.1, and we want $a_0 = \lambda_o / 2$. Similarly, when $z = -d$ and $L_g(z) = 0$, then $w(z) = a_1$, which is exactly the relationship we described between $L_g(z)$ and $w(z)$ for the linearly tapered medium in figure 4.1. Section 4.2 will detail how different relationships between $L_g(z)$ and $w(z)$ yield different cavity geometries based on the characteristic impedance of the high index medium in the cavity.

4.2 Isotropic Tapered Cavity Design

We propose a novel idea for a partially loaded and tapered rectangular cavity to suppress the high order resonances in the VSWR and the realized gain of figure 3.19 and figure 3.20. These multiple resonances may be removed by employing the shape of a tapered cavity implementing equation 4.14.

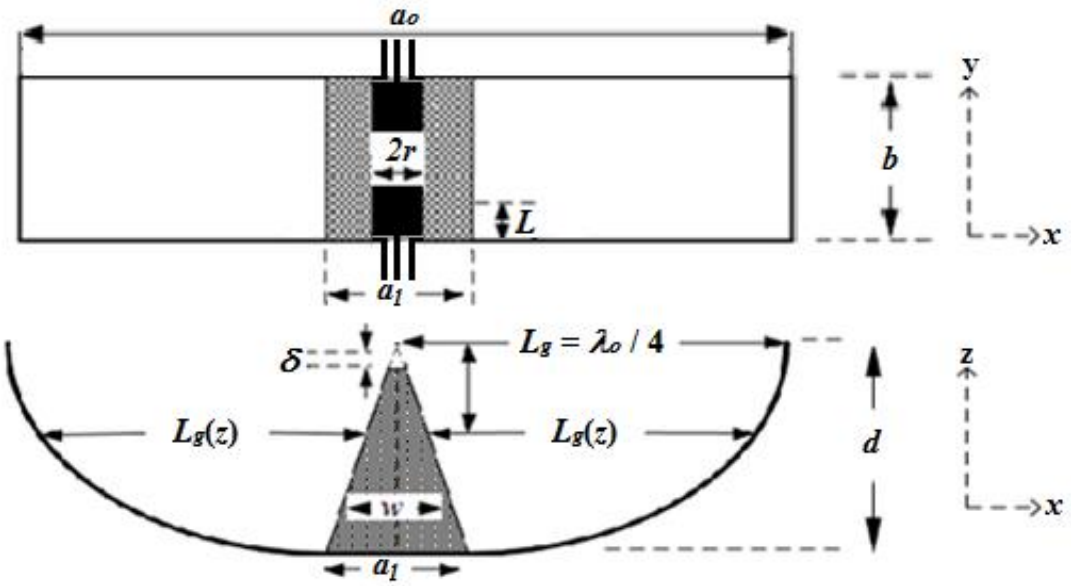

Figure 4.5: Top view and side view of the geometry of the tapered cavity design when $\mu_r/\varepsilon_r > 1$.

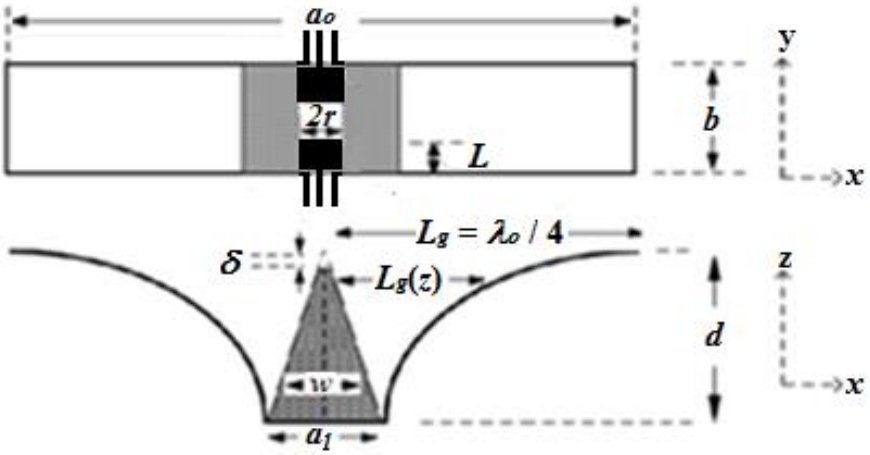

Figure 4.6: Top view and side view of the geometry of the tapered cavity design when $\mu_r/\varepsilon_r < 1$.

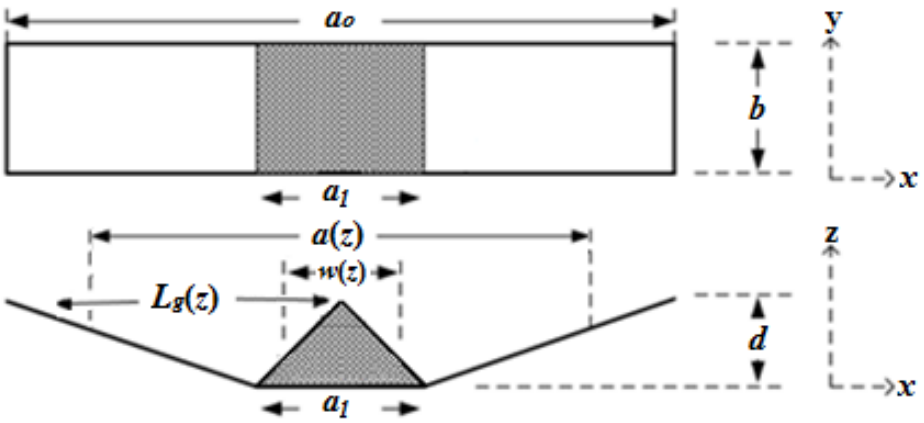

Figure 4.7: Top view and side view of the geometry of the tapered cavity design when $\mu_r/\varepsilon_r = 1$.

Figure 4.5 through figure 4.7 shows the geometries of three different tapered cavity designs based on equation 4.14. Figure 4.5 shows a tapered cavity for the case when $\mu_r/\varepsilon_r > 1$ while figure 4.6 shows the case when $\mu_r/\varepsilon_r > 1$. The reader should note that if $\mu_r/\varepsilon_r = 1$ but $\mu_r > 1$ and $\varepsilon_r > 1$, then the taper will be perfectly linear as in figure 4.7. Furthermore, if both $\mu_r = 1$ and $\varepsilon_r = 1$ then we will have a standard rectangular cavity because this is equivalent to the air-filled cavity depicted in figure 3.11a.

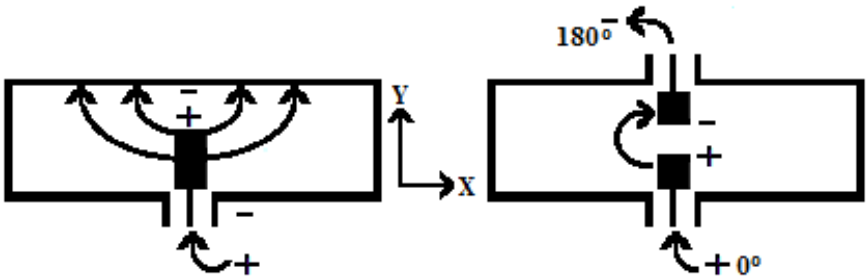

Figure 4.8: (a) The fringing fields produced by an asymmetric single probe feed. (b) The continuous current path of a symmetric dual probe feed.

We feed the LPAs in figure 4.5 through figure 4.7 with two symmetric rectangular probes of thickness $T = 2$ mm located at $z = -\delta$. We short the two probes to the inner

conductors of two 50 Ω coaxial lines which are fed 180° out of phase. We show the advantage of a symmetric feed over an asymmetric feed in figure 4.8a and figure 4.8b.

A single asymmetric probe produces fringing fields over the voltage drop between the probe and cavity walls as in figure 4.8a. An unbalanced feed causes this voltage drop as a result of the 180° phase shift between the inner and outer conductors of a coaxial line. These fringing fields cause a reactance that produces a mismatch between the coaxial line and the impedance seen at the cavity aperture. We reduce this mismatch using the balanced feed structure shown in figure 4.8b. By feeding the two symmetric probes 180° out of phase, there is now a voltage drop between the two probes providing a continuous path for the current. This manifests itself as a +/- voltage drop across the two input ports as shown in figure 4.8a. This is accomplished via the 180° phase difference because e^{j*0} = + 1 and $e^{j*\pi}$ = -1.

4.3 LPA Design: Dielectric Medium (ε_r = 10.2)

This section describes the numerical simulation of the LPA design shown in figure 4.6 using CST Microwave Studio 2014. We partially load the tapered cavity with ROGERS6010 dielectric material exhibiting ε_r = 10.2, μ_r = 1, and tanδ = 0.02. We feed the LPA using a symmetric two-port feed. The phase difference between the two excitation ports is 180°. We explained previously this two-port adaption of our FLPA design in greater detail in section 4.2. We show the CST model of figure 4.6 in figure 4.9. This antenna model represents an antenna that would be cheap to implement due to the fact that it uses a readily available and cheap dielectric material exhibiting low loss. Table 4.1 gives the normalized dimensions of this antenna design in terms of λ_o.

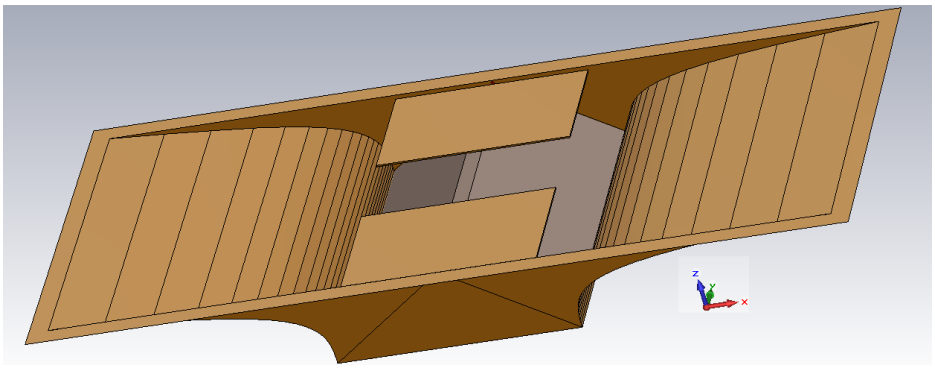

Figure 4.9: The CST model of the tapered isotropic dielectric LPA design when μ_z/ε_y = 0.098.

Table 4.1: Normalized dimensions for the tapered cavity models given in figure 4.6.

a_0	a_1	b	r	L	d	T	δ	F_L
$\lambda_o/2$	$a_o/(\mu_r\varepsilon_r)^{0.5}$	$\lambda_o/4.5$	$0.125\lambda_o$	$0.1\lambda_o$	$0.05\lambda_o$	2 mm	6.8 mm	$0.01\lambda_o$

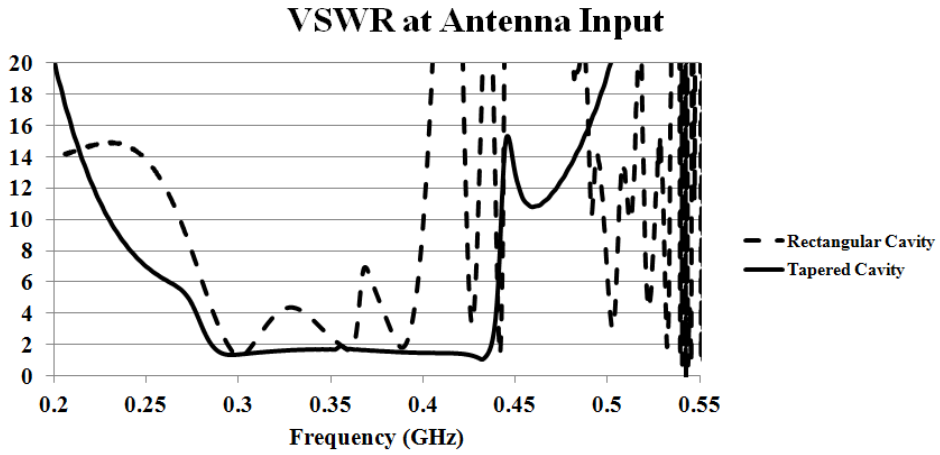

Figure 4.10: VSWR of the tapered dielectric LPA and the loaded FLPA.

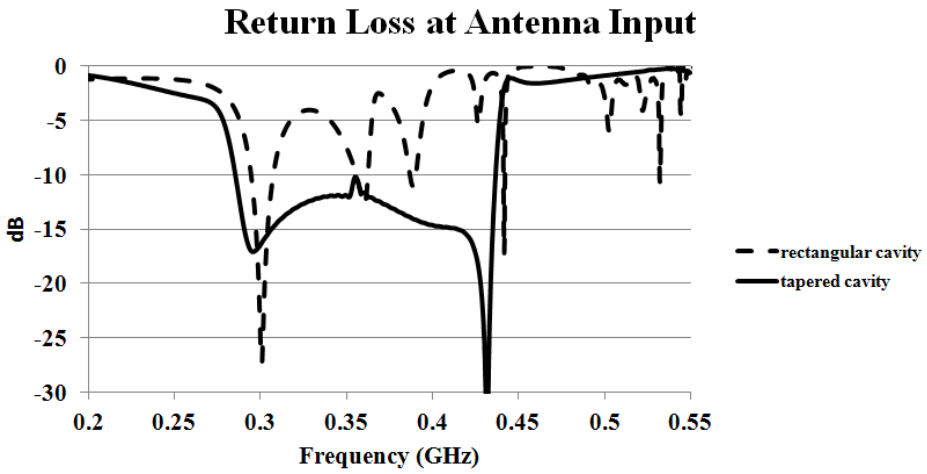

Figure 4.11: Return loss of the tapered dielectric LPA and the loaded FLPA.

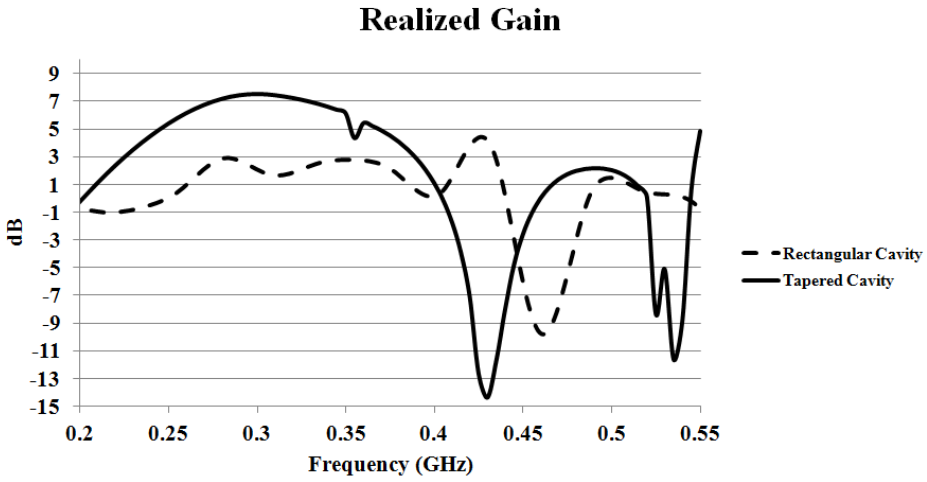

Figure 4.12: Realized gain of the tapered dielectric LPA and the loaded FLPA.

Figure 4.10 through figure 4.12 compare the VSWR, return loss, and realized gain of the tapered dielectric LPA in figure 4.6 to that of the fully loaded LPA in figure 3.17. The solid curve shows the results of the tapered cavity design with λ_o = 2.0 m, and the dashed curve shows the results of the non-tapered cavity design with λ_o = 1.5 m. Figure 4.13a though figure 4.13c show the radiation plots at $\phi = 0^o$ at 285 MHz, 350 MHz, and 435 MHz. These plots achieve peak realized gain values at bore sight of 7.36 dB, 6.17 dB, and -11.7 dB respectively.

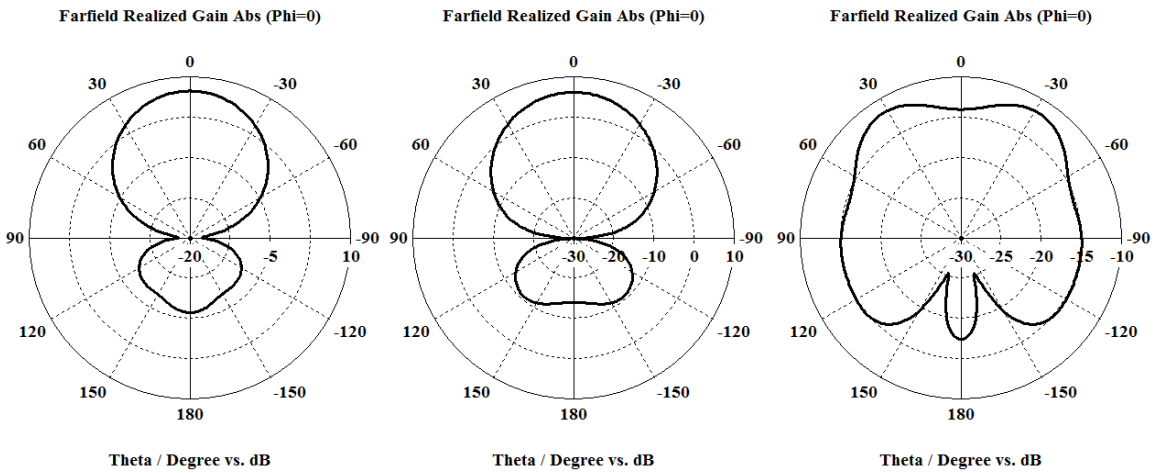

(a) (b) (c)

Figure 4.13: Radiation patterns of the tapered dielectric. (a) 285 MHz. (b) 350 MHz. (c) 435 MHz.

Figure 4.10 and figure 4.11 show that partially loading the cavity with a dielectric medium suppresses the destructive interference due to multiple resonances seen in the dotted curve. In fact we see a VSWR of less than 2 and an S11 less than -10 dB from 285 MHz to 435 MHz (0.53 octaves). Figure 4.12 shows we have significantly improved the realized gain over the non-tapered cavity from 200 MHz to 400 MHz with up to 4.5 dB improvement. From 200 MHz to 400 MHz the tapered cavity model produces a positive realized gain with a cavity profile of $0.05\lambda_o$.

Looking more closely at figure 4.12, we see a dramatic decline in the realized gain manifest itself at about 430 MHz for the tapered cavity design. This partially corresponds to the abrupt degradation in VSWR and return loss seen in the solid curves of figure 4.10 and figure 4.11 at 440 MHz. However, we see the realized gain begin to degrade around 400 MHz where the VSWR curve is still less than 2.0. A second contributing factor is coming from the two-port matching network. If we think about the

two-port matching network as a two-element monopole array fed 180° out of phase, then we would expect the broadside radiation to cancel when the monopoles are at odd multiples of $\lambda_o/4$. This would cause a null in the directivity, and thus the realized gain, at broadside. This is exactly what we are seeing between 400 MHz to 450 MHz in figure 4.12. To demonstrate this phenomenon we show the three dimensional far field directivity pattern of the LPA at 400 MHz and 430 MHz in figures 4.14a through 4.14b and figures 4.15a through 4.15b.

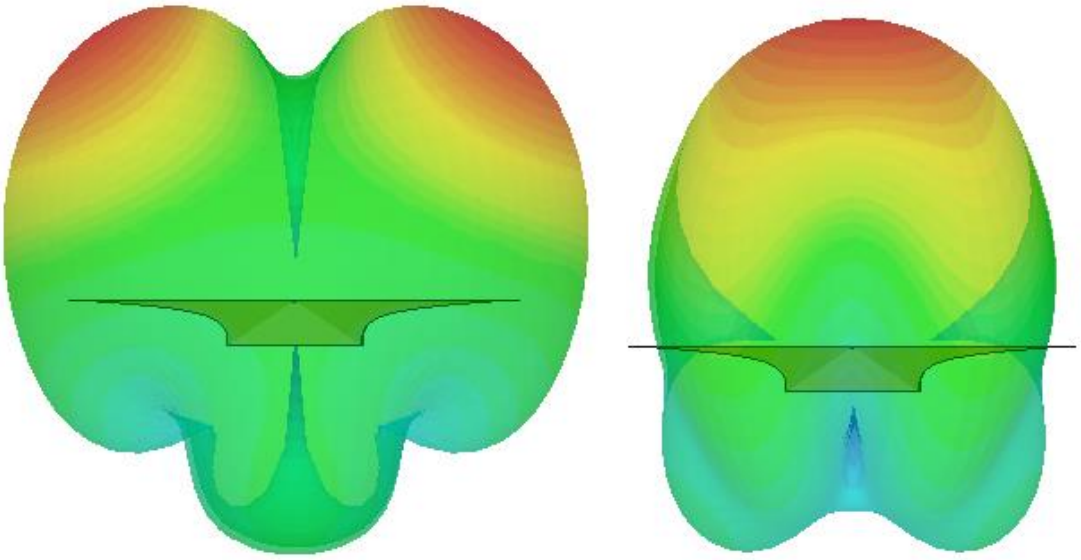

(a) (b)

Figure 4.14: Far field directivity patterns of the tapered dielectric LPA at 400 MHz. (a) Fed in phase. (b) Fed 180° out of phase.

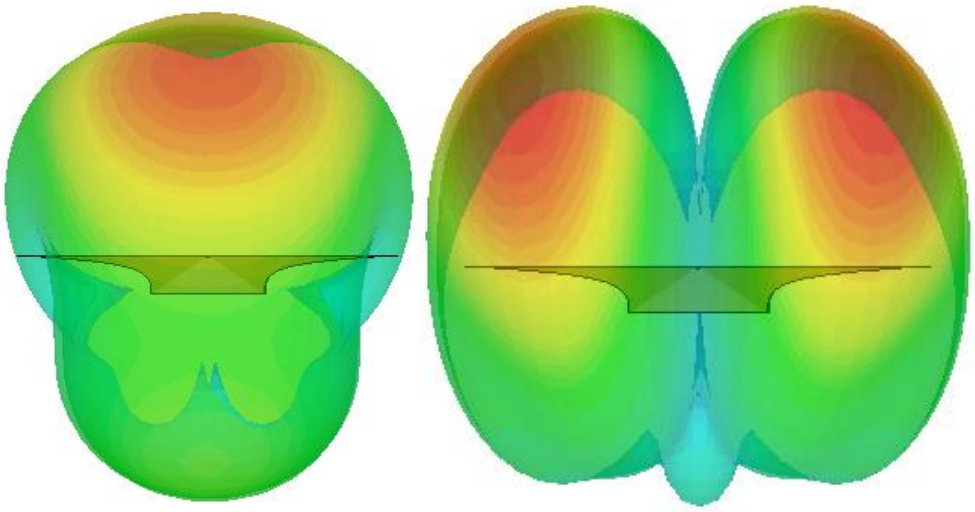

(a) (b)

Figure 4.15: Far field directivity patterns of the tapered dielectric LPA at 440 MHz.

(a) Fed in phase. (b) Fed 180° out of phase.

Figures 4.14a and 4.14b show the directivity at 400 MHz when the two port matching network are fed in phase versus when they are fed 180° out of phase. Figure 4.15a and 4.15b show the same thing at 440 MHz. In figures 4.14b and 4.15b, we see how as we approach the frequency that corresponds to $L = \lambda_o / 4$ we switch from a peak at broadside (indicated in red) to a null at broadside (indicated in blue) when our probes are fed 180° out of phase. The behavior is reversed for when we feed our ports in phase as indicated by figures 4.14a and 4.15a.

As a verification of the two-port matching network over the one-port matching network we show in figures 4.8b and 4.8a respectively, we simulate the LPA model of figure 4.9 with the two feed structures in figure 4.16a and figure 4.16b. We use the same dimensions as those in table 4.1 with $L_1 = L$, $L_2 = 2L$, and $\lambda_o = 1.5$ m. Figure 4.17 shows a comparison of the VSWR seen at the coaxial line input for both the single port matching network and dual port matching network. We see that the balanced feed

provides a vast improvement over the unbalanced feed which provides no useable bandwidth except for two sharp resonances at 285 MHz and 442 MHz. The results of this section demonstrate that by suppressing higher order resonances and switching to a balanced matching network, we are able to get a good impedance match versus the fully loaded rectangular cavity of section 3.3.

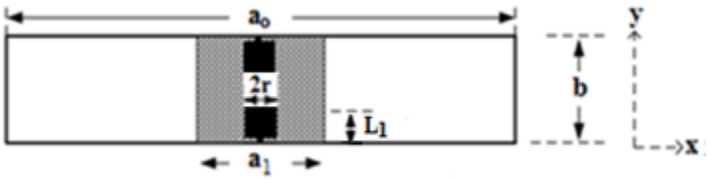

(a)

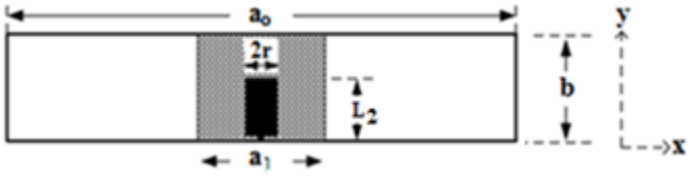

(b)

Figure 4.16: (a) Symmetric two port feed at aperture of LPA. (b) Asymmetric one port feed at aperture of LPA.

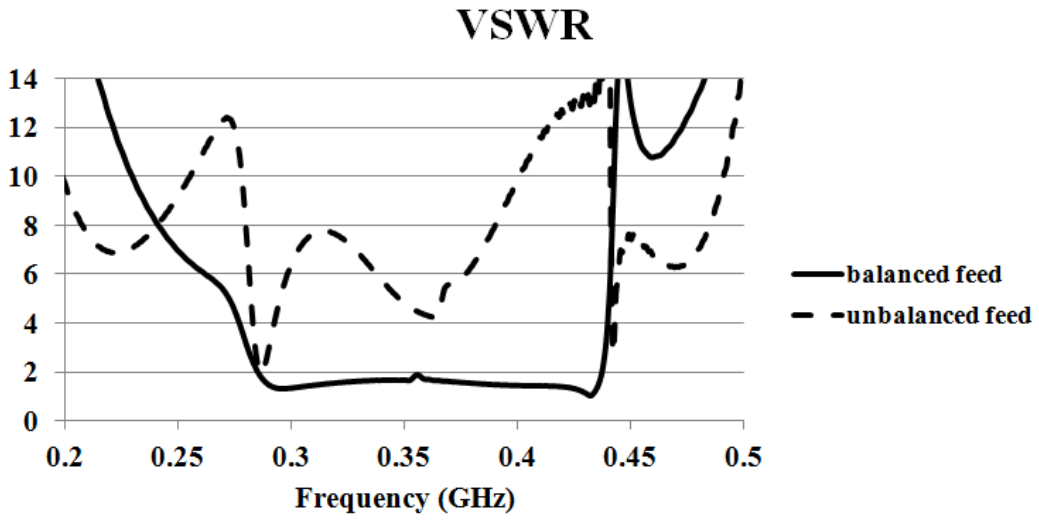

Figure 4.17: VSWR of the balanced two-port feed and the unbalanced one-port feed.

4.4 Comparison of Isotropic LPA Design to FLPA, and State of the Art

Using the FLPA design from section 3.2, we compare the two tapered isotropic LPA designs from sections 4.3 and 4.4 highlighting differences in bandwidth, realized gain, and cavity profile.

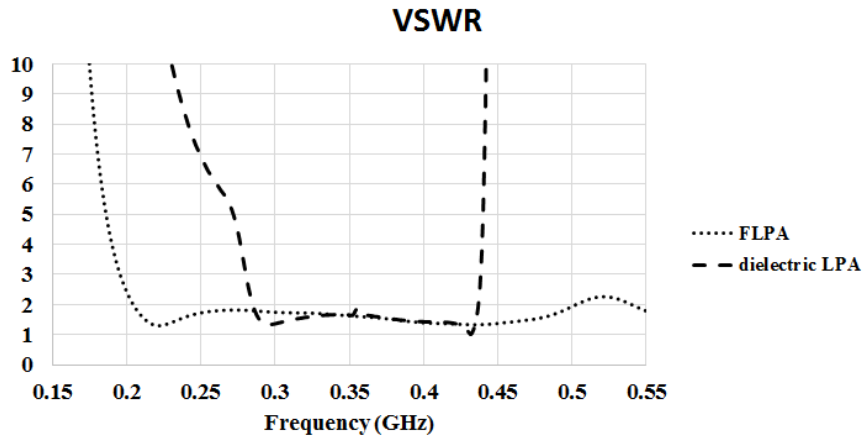

Figure 4.18: VSWR of the tapered dielectric LPA and FLPA.

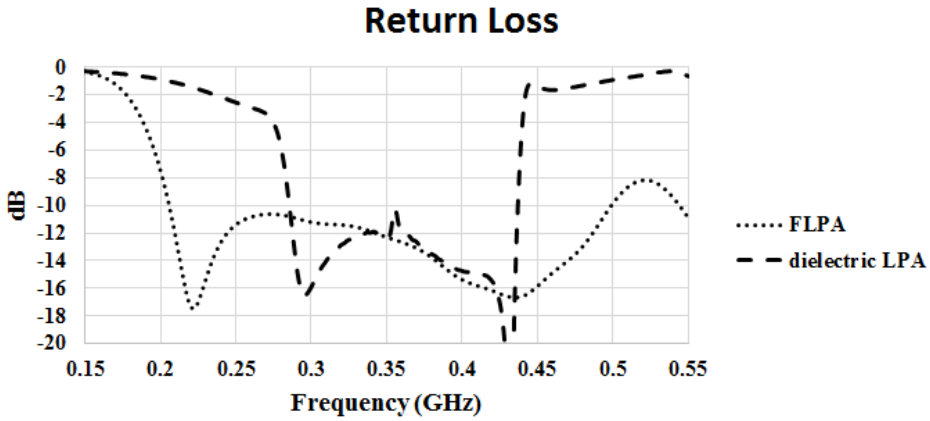

Figure 4.19: Return loss of the tapered dielectric LPA and FLPA.

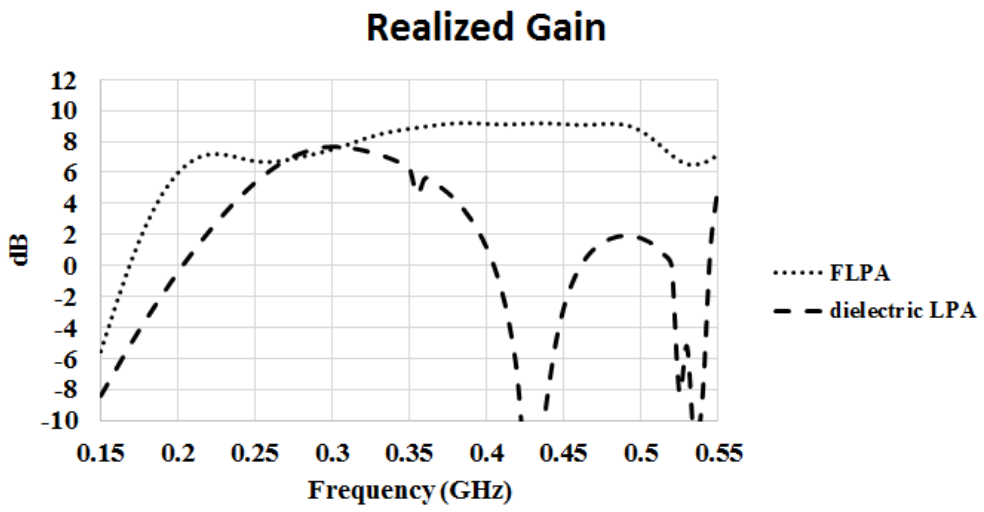

Figure 4.20: Realized gain of the tapered dielectric LPA and FLPA.

Figure 4.18 through figure 4.20 show comparisons of the VSWR, return loss, and realized gain of the tapered dielectric LPA and FLPA designs. We calculate the results for λ_o = 2 m and λ_o = 1.56 m respectively. These figures show that the FLPA design is clearly the best in terms of bandwidth with 1.4 octaves of better than -10 dB bandwidth, whereas the tapered dielectric LPA has approximately 0.53 octaves of -10 dB bandwidth. We see from figure 4.20 that the tapered dielectric LPA only has comparable realized gain to the FLPA from 250 MHz to 350 MHz.

We should note that the tapered dielectric LPA has a larger aperture than the FLPA since they are both scaled to a larger value of λ_o. The profile of the tapered dielectric LPA is $d = 0.05\lambda_o$ versus $d = 0.14\lambda_o$ for the FLPA. This represents a 64.3% reduction in electrical height over the FLPA. Therefore, the tapered dielectric LPA design represent a major reduction in profile at the expense of bandwidth. However, we saw in appendix B that the performance of anisotropic magnetic material was superior to that of isotropic materials, and we expand greatly on this idea in chapter 5.

Table 4.2: Comparison of tapered LPAs to state of the art wideband LPA designs.

reference	**Aperture**	**substrate**	**BW (octaves)**	**gain (dB)**	**profile (λ_o)**
[17]	spiral	dielectric	7.3	-2.6 - 6.9	0.03
[18]	Inverted L	dielectric	0.59	-	0.09
[19]	Bowtie	dielectric	0.77	4.0 - 6.0	0.064
[20]	Discone	none	0.92	-	0.09
[21]	Monopole	HIS/EBG	0.77	7.0 - 10.25	0.1
[22]	Bowtie	HIS/EBG	1.07	3.3 - 9.35	0.05
[23]	dipole	HIS/EBG	0.41	-	0.06
-	FLPA	none	1.44	4.8 - 8.2	0.14
-	tapered cavity	dielectric	0.53	-20.0 – 8.0	0.05

Table 4.3 shows that the tapered isotropic cavity LPAs have comparable profiles to the thinnest state of the art LPAs. The tapered dielectric LPA is an antenna utilizing a commercial dielectric, and while it maintains a thin profile, its bandwidth performance is worse than just about every other LPA in table 4.3. Also, its positive realized gain doesn't extend over the entire VSWR bandwidth.

Chapter 5
LPA Design Incorporating an Anisotropic Transverse Resonance Formulation

This chapter investigates the performance of a radiating rectangular cavity partially loaded with uniaxial anisotropic media. First, we discuss in detail the properties of the anisotropic magnetic media we will use to load our LPA design. Then we derive the anisotropic transverse resonance condition for a partially loaded rectangular cavity with a high index medium. The high index medium incorporates the same linear taper as in chapter 4. We derive a novel cavity shape tailored to the taper in the anisotropic medium which maintains a constant resonant frequency within the cavity. This tapered anisotropic cavity design results in an LPA model achieving 1.2 octaves of bandwidth with a positive realized gain and a further 20.0% reduction in electrical height over the isotropic LPA of section 4.3. Furthermore, we show that based on the anisotropic transverse resonance, we can eliminate the need to taper the cavity by setting $\mu_z = \varepsilon_y = 1$ and yield the same results. We also demonstrate how the design scales in frequency when maintaining the same anisotropic tensor values. Finally, we investigate the effects of adding losses to the $\underline{\underline{\boldsymbol{\mu}}}_r$ tensor. We describe the simulation of all models in this design in appendix E. In the interest of studying the effects of magnetic media on the performance of an LPA, we keep $\underline{\underline{\boldsymbol{\varepsilon}}}_r = \varepsilon_r \underline{\underline{\boldsymbol{I}}}$.

5.1 Measured Parameters of the Anisotropic Permeability Tensor

This section illustrates actual measured data of the effective permeability provided for the P4 Metaferrite purchased by the U.S. Army Research Laboratory from Metamaterials Inc. The measurement process that produces this data is proprietary to Metamaterials Inc. We define the anisotropic $\underline{\underline{\boldsymbol{\mu}}}_r$ tensor as

$$\underline{\underline{\mu_r}}(f) = \begin{bmatrix} \mu_x(f) & 0 & 0 \\ 0 & \mu_y(f) & 0 \\ 0 & 0 & \mu_z(f) \end{bmatrix}, \tag{5.1}$$

where f is frequency. The inclusion of the f in the definition of equation 5.1 indicates that both the magnitudes and loss tangents of the tensor elements are frequency dependent.

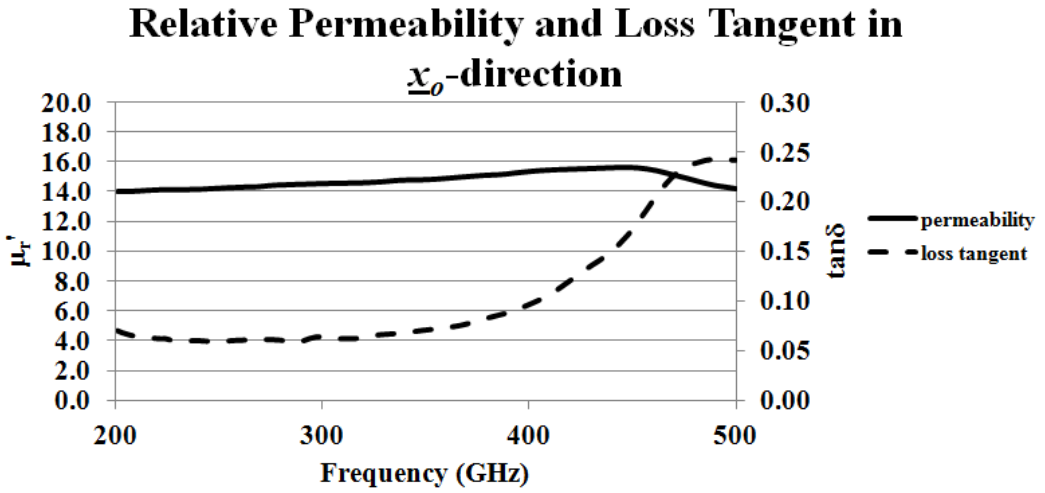

Figure 5.1: Relative permeability and loss tangent of P4 metaferrite in the $\underline{x}_o$-direction.

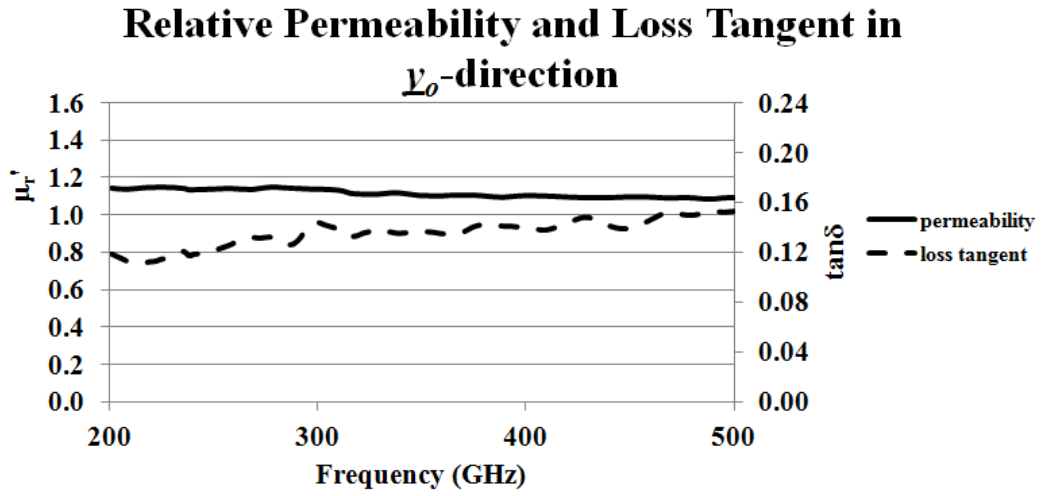

Figure 5.2: Relative permeability and loss tangent of P4 metaferrite in the $\underline{y}_o$-direction.

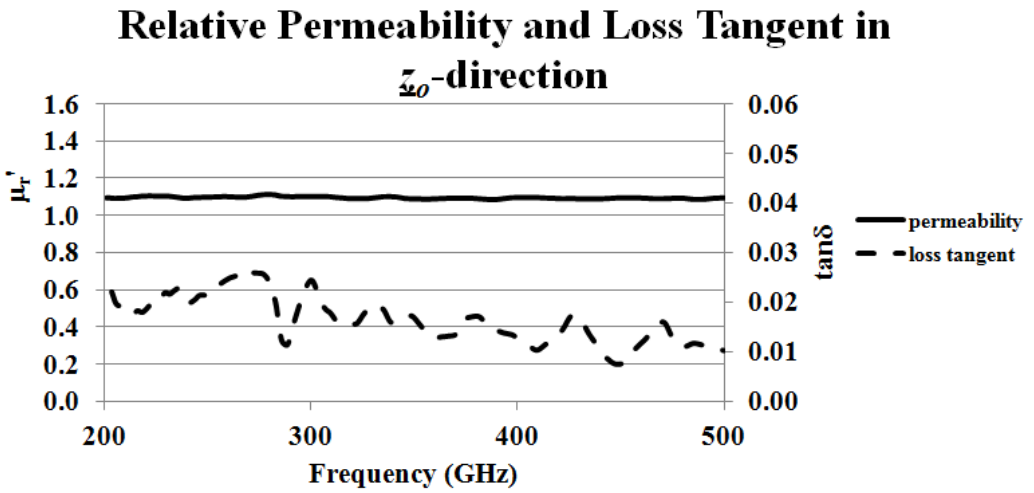

Figure 5.3: Relative permeability and loss tangent of P4 metaferrite in the $\underline{z}_o$-direction.

Figure 5.3 through figure 5.3 show the magnitude and loss tangent of the $\underline{\underline{\mu}}_r$ tensor elements. We can see from figure 5.1 that $\underline{x}_o$ is the dominant direction. We see that the value of μ_x' varies between 14 and 16 from 200 MHz to 500 MHz, while the loss tangent varies from 0.05 to 0.25 over the same frequency range. The magnitude of μ_y' and μ_z' in the $\underline{y}_o$- and $\underline{z}_o$-directions is approximately unity while the loss tangent in the $\underline{y}_o$-direction varies between 0.08 and 0.1, and the loss tangent in the $\underline{z}_o$-direction is approximately 0.02. In order to simplify the simulations, we will use a frequency independent value of 15 for the dominant axis or axes of the $\underline{\underline{\mu}}_r$ tensor and 1 for all other axes. Initial investigations will assume a lossless media, but in section 5.3.2 we will introduce not only the measured frequency dependent $\underline{\underline{\mu}}_r$ tensor but the losses as well.

5.1.1 *Validation of Measured Parameters via Simulation and Measurement*

Since, the measured values of figure 5.1 through figure 5.3 serve as the basis for all the LPA designs and CST models from this point on, we want to verify that their accuracy. We achieve this by utilizing an antenna test bed that consists of a center fed fat dipole backed by a rectangular cavity. Each arm of the dipole is fed 180° out of phase

using two SMA ports. We partially load the cavity with tiles of the P4 metaferrite tiles we describe in appendices A.1 through A.3. This prototype antenna simply provides a mechanism to measure data and verify the accuracy of the anisotropic properties claimed by the manufacturer.

We must make clear that we use this test bed to verify the accuracy of the P4 metaferrite tile measurements only. We did not intend this antenna test bed to verify any aspect of the antenna designs from this dissertation or even to perform well from 200 MHz to 500 MHz. In fact, the results of this section show this antenna to have a poor impedance match and realized gain. However, in terms of verifying the accuracy of the measurements of anisotropic tensor values, our only interest is in how the return loss and realized gain of the simulations compare to the experimental results, not whether the test bed represents a good antenna design. That being said, the comparison of simulation to experimental results for the antenna test bed in this section shows good agreement, and verifies the accuracy of the data in figure 5.1 through figure 5.3.

Figure 5.4a shows the dimensions of the cavity and the radiating dipole element. Figure 5.4b shows the cavity in profile and specifies the dimensions of the feed elements. The dipole is center fed 180° out of phase. The dipole is a piece of FR4 with a lossy copper coating and the cavity walls are also lossy copper; however, we define the copper elements as a PEC in our simulation as this simplifies the model.

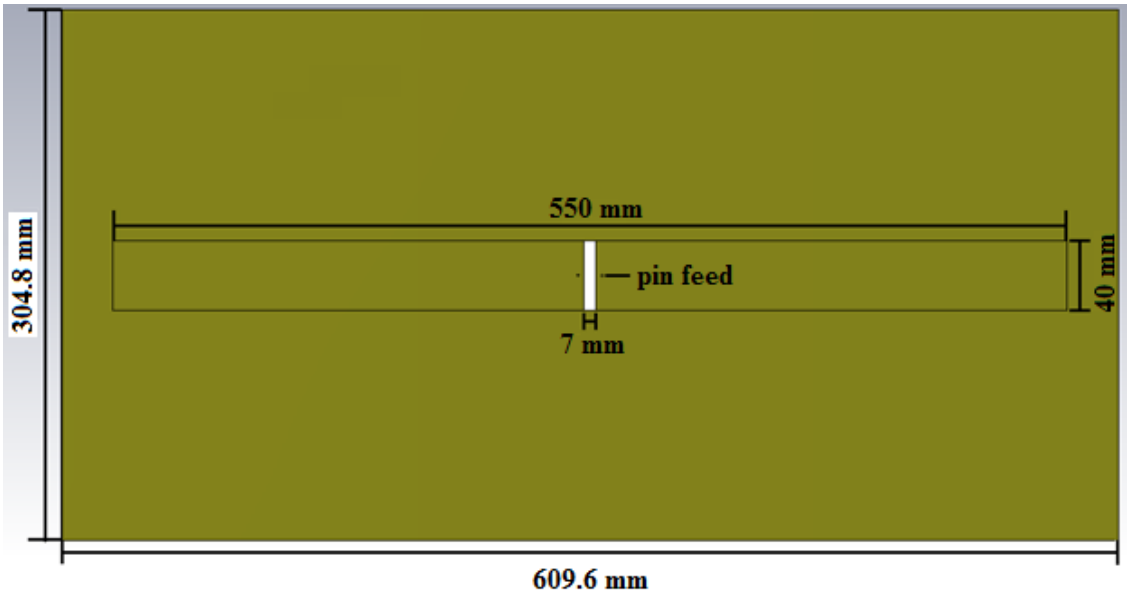

(a)

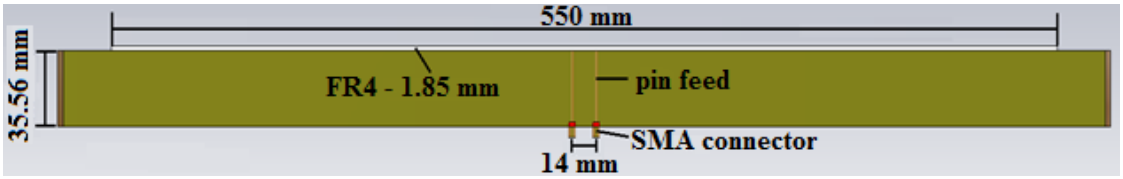

(b)

Figure 5.4: Test bed cavity dimensions. (a) Transverse (*x*,*y*) plane. (b) Normal (*x*,*z*) plane.

Figure 5.5a and figure 5.5b show how we load the test bed cavity with P4 metaferrite tiles. Figure 5.5a shows the placement of the P4 metaferrite tiles in relation to the arms of the dipole cavity. The placement of the tiles is arbitrary as we were not interested in optimizing the performance of the antenna test bed. Figure 5.5b shows the antenna in profile and illustrates the placement of the tiles with respect to the backshort of the cavity.

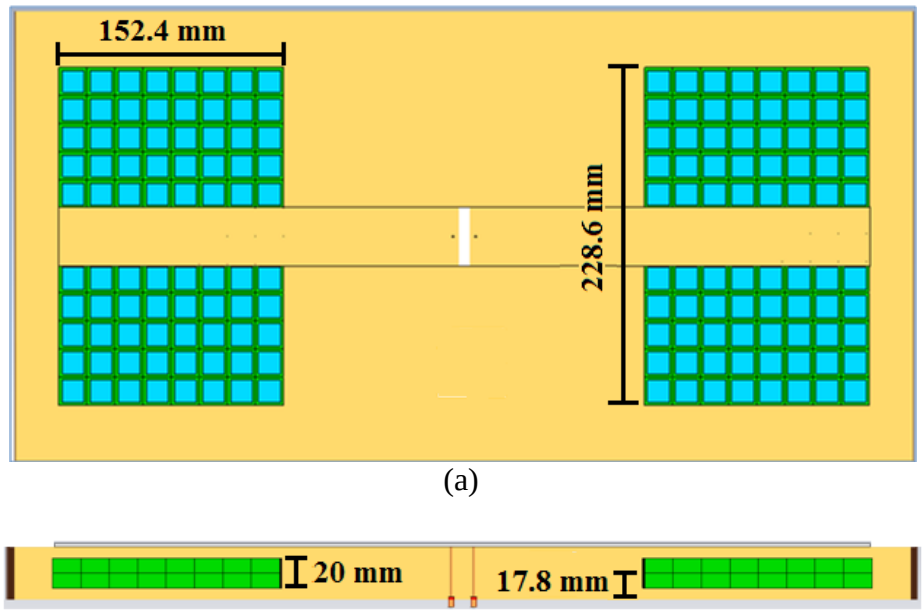

Figure 5.5: Metaferrite placement in the cavity. (a) Transverse (*x*,*y*) plane. (b) Normal plane (*x*,*z*).

Figure 5.6 shows the comparison of measured S-parameters versus those generated by the simulation of the model using CST Studio Suite 2014. The blue and red lines represent the measurement results, while the green and purple lines represent simulation results. Both sets of plots show good agreement between simulation and measurement with a frequency shift of about 10 MHz, which represents about a 3.5% deviation.

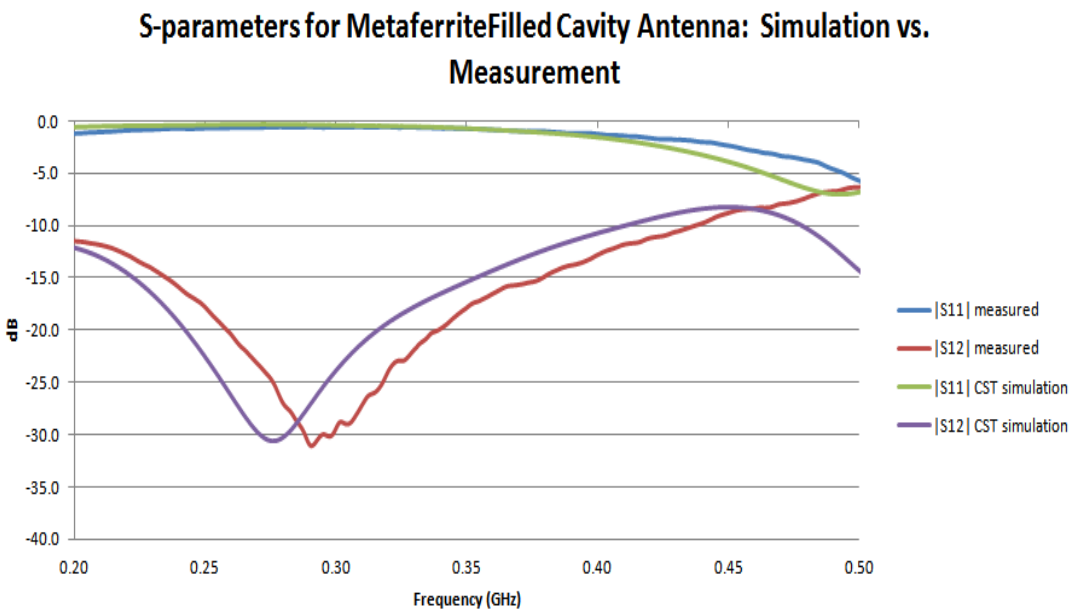

Figure 5.6: Measured and simulated S-parameters of the cavity test bed with Metaferrite.

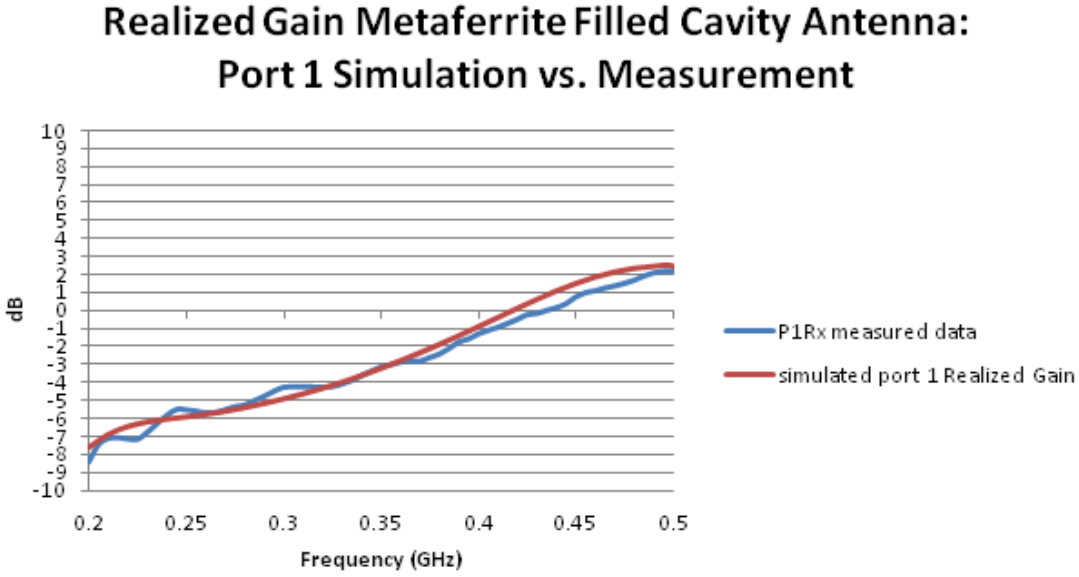

Figure 5.7: Measured and simulated realized gain of the cavity test bed loaded with Metaferrite.

Figure 5.7 shows the realized gain of the antenna test bed measured in an anechoic chamber versus simulation results for the model shown in figure 5.5a and figure 5.5b. Based on the agreement between the S-parameter and realized gain results, we can say

the model of the $\underline{\underline{\mu_r}}$ tensor values from figure 5.1 through figure 5.3 accurately represents those of a real medium. This gives us confidence in using these values as the basis for our anisotropic tensors in sections 5.3 and 5.4.

5.2 Anisotropic Transverse Resonance of a Partially Loaded Parallel Plate Waveguide

This section describes the derivation of an anisotropic transverse resonance condition established between the conducting walls of the cavity. If we assume a linear taper in the width of the anisotropic medium, $w(z)$, then at any depth z in the cavity, we can represent the horizontal distance as a partially filled parallel plate transmission line as in section 4.1. We repeat figure 4.1 as figure 5.8 for convenience. Again we can calculate $L_g(z)$ as the unknown distance between the edge of the high index medium and the cavity wall based on a transverse resonance condition in the $\underline{\mathbf{x}}_o$-direction. However, we first need to derive the characteristic impedance of the anisotropic region in the transmission line model.

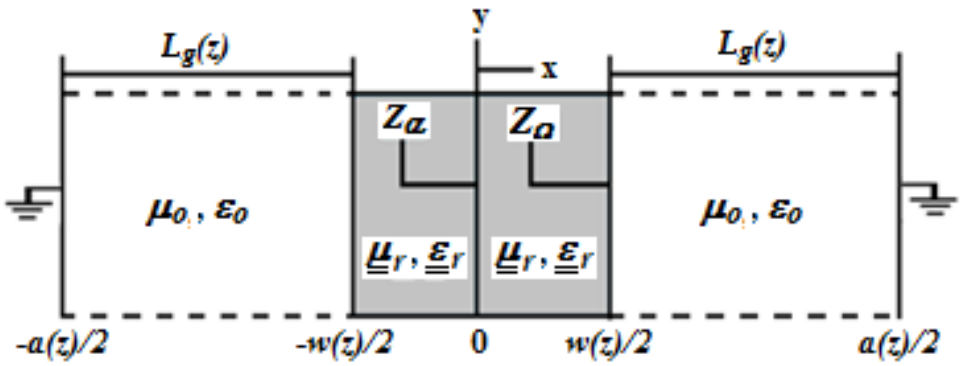

Figure 5.8: Symmetrically loaded transmission line model with a short at either end.

5.2.1 *Electric and Magnetic Fields in the Free Space Region*

We start with Maxwell's source free equations:

$$\nabla \times \underline{E} = -j\omega\mu_o \underline{H}\,, \tag{5.2a}$$

$$\nabla \times \underline{H} = j\omega\varepsilon_o \underline{E}\,. \tag{5.2b}$$

Evaluating the curl operator of equations 5.2a and 5.2b yields the following transverse components for the electric and magnetic fields in the waveguide in terms of H_z and E_z

$$E_x = -\frac{j}{k_o^2 - k_{zo}^2}\left(\omega\mu_o \frac{dH_z}{dy} + k_{zo}\frac{dE_z}{dx}\right), \tag{5.3a}$$

$$E_y = \frac{j}{k_o^2 - k_{zo}^2}\left(\omega\mu_o \frac{dH_z}{dx} - k_{zo}\frac{dE_z}{dy}\right), \tag{5.3b}$$

$$H_x = \frac{j}{k_o^2 - k_{zo}^2}\left(\omega\varepsilon_o \frac{dE_z}{dy} - k_{zo}\frac{dH_z}{dx}\right), \tag{5.3c}$$

$$H_y = -\frac{j}{k_o^2 - k_{zo}^2}\left(\omega\varepsilon_o \frac{dE_z}{dx} + k_{zo}\frac{dH_z}{dy}\right). \tag{5.3d}$$

To solve for H_z we formulate the transverse free space wave equation from 5.2a and 5.2b as

$$\nabla_T \times \nabla_T \times \underline{H} = j\omega\varepsilon_o\left(\nabla_T \times \underline{E}\right) = \nabla_T\left(\nabla_T \cdot \underline{H}\right) - \nabla_T^2 H_z\,,$$

$$j\omega\varepsilon_o\left(-j\omega\mu_o H_z\right) + \nabla_T^2 H_z = 0\,,$$

$$\left(\frac{d^2}{dx^2} + \frac{d^2}{dy^2} + k_o^2\right) H_z = 0\,. \tag{5.4}$$

At resonance $k_{zo} = 0$, which allows us to calculate resonance at cutoff for this structure. If we assume a TE_{10}-like resonance, then $k_{yo} = 0$ for the first resonance at cutoff, which means no variation of the fields in the *y*-direction. This means that $d^2H_z/dy^2 = 0$ and

$$\left(\frac{d^2}{dx^2}+k_o^2\right)H_z=0\,, \tag{5.5}$$

$$\beta_o=k_o\,. \tag{5.6}$$

Solving equation 5.5 for H_z and inserting into equations 5.3a through 5.3d yields

$$H_z=Ae^{-jk_ox}+Be^{+jk_ox}\,, \tag{5.7a}$$

$$E_y=\frac{j\omega\mu_o}{k_o^2}\left(-jk_o\right)\left(Ae^{-jk_ox}-Be^{+jk_ox}\right)=Z_o\left(Ae^{-jk_ox}-Be^{+jk_ox}\right). \tag{5.7b}$$

We can see from equations 5.3a through 5.3d that based on our resonance conditions on E_z, k_{zo} and k_{yo} that $E_x = 0$, $H_x = 0$ and $H_y = 0$.

5.2.2 Electric and Magnetic Fields in the Anisotropic Region

Again assume Maxwell's source free equations in the anisotropic region

$$\nabla x\underline{E}=-j\omega\mu_o\underline{\mu}_r\cdot\underline{H}\,, \tag{5.8a}$$

$$\nabla x\underline{H}=j\omega\varepsilon_o\underline{\varepsilon}_r\cdot\underline{E}\,, \tag{5.8b}$$

$$\underline{\varepsilon}_r=\begin{bmatrix}\varepsilon_x & 0 & 0\\ 0 & \varepsilon_y & 0\\ 0 & 0 & \varepsilon_z\end{bmatrix}, \tag{5.9a}$$

$$\underline{\mu}_r=\begin{bmatrix}\mu_x & 0 & 0\\ 0 & \mu_y & 0\\ 0 & 0 & \mu_z\end{bmatrix}. \tag{5.9a}$$

We know from appendix C that evaluating the curl operator of equations 5.8a and 5.8b yields the following transverse components for the electric and magnetic fields in the anisotropic medium. We also know the form of the dispersion equations for both E_z and H_z.

$$E_x = -\frac{j}{k_o^2 \mu_y \varepsilon_x - k_{z1}^2}\left(\omega \mu_o \mu_y \frac{dH_z}{dy} + k_{z1}\frac{dE_z}{dx}\right), \tag{5.10a}$$

$$E_y = \frac{j}{k_o^2 \mu_x \varepsilon_y - k_{z1}^2}\left(\omega \mu_o \mu_x \frac{dH_z}{dx} - k_{z1}\frac{dE_z}{dy}\right), \tag{5.10b}$$

$$H_x = \frac{j}{k_o^2 \mu_x \varepsilon_y - k_{z1}^2}\left(\omega \varepsilon_o \varepsilon_y \frac{dE_z}{dy} - k_{z1}\frac{dH_z}{dx}\right), \tag{5.10c}$$

$$H_y = -\frac{j}{k_o^2 \mu_y \varepsilon_x - k_{z1}^2}\left(\omega \varepsilon_o \varepsilon_x \frac{dE_z}{dx} + k_{z1}\frac{dH_z}{dy}\right), \tag{5.10d}$$

$$\frac{k_o^2 \varepsilon_x}{k_o^2 \mu_y \varepsilon_x - k_z^2}\frac{d^2 E_z}{dx^2} + \frac{k_o^2 \varepsilon_y}{k_o^2 \mu_x \varepsilon_y - k_z^2}\frac{d^2 E_z}{dy^2} + k_o^2 \varepsilon_z E_z = 0, \tag{5.11a}$$

$$\frac{k_o^2 \mu_x}{k_o^2 \mu_x \varepsilon_y - k_z^2}\frac{d^2 H_z}{dx^2} + \frac{k_o^2 \mu_y}{k_o^2 \mu_y \varepsilon_x - k_z^2}\frac{d^2 H_z}{dy^2} + k_o^2 \mu_z H_z = 0. \tag{5.11b}$$

Now set $k_{z1} = 0$ which allows us to calculate resonance at cutoff for this structure. Similarly, we can assume that $k_{y1} = 0$ for the first resonance. This means $d^2H_z / dy^2 = 0$

$$\left(\frac{d^2}{dx^2} + k_o^2 \mu_z \varepsilon_y\right) H_z = 0, \tag{5.12}$$

$$\beta_1 = k_o \sqrt{\mu_z \varepsilon_y}. \tag{5.13}$$

Solving equation 5.12 for H_z and plugging the result into equations 5.10a through 5.10d yields

$$H_z = Ce^{-j\beta_1 x} + De^{+j\beta_1 x}, \tag{5.14a}$$

$$E_y = \frac{jZ_o}{k_o \varepsilon_y}\left(-j\beta_1\right)\left(Ce^{-j\beta_1 x} - De^{+j\beta_1 x}\right) = Z_o\sqrt{\frac{\mu_z}{\varepsilon_y}}\left(Ce^{-j\beta_1 x} - De^{+j\beta_1 x}\right). \tag{5.14b}$$

We can see from equations 5.10a through 5.10d that based on our resonance conditions on E_z, k_{z1} and k_{y1} that $E_x = 0$, $H_x = 0$ and $H_y = 0$.

5.2.3 Solving for the Characteristic Impedances of the Two Regions

The first boundary condition exists at the perfect electric conductor (PEC) boundary at $x = -a / 2$ where the electric field is known to be zero

$$E_y\Big|_{x=-\frac{a}{2}} = 0 \rightarrow Ae^{jk_o\frac{a}{2}} = Be^{-jk_o\frac{a}{2}},$$

$$A = Be^{-jk_o a}. \tag{5.15}$$

Plugging equation 5.15 into our equations 5.7a and 5.7b yields

$$\begin{aligned} E_y &= Z_o B\left[e^{-jk_o x}e^{-jk_o a} - e^{+jk_o x}\right] \\ &= Z_o Be^{-jk_o\frac{a}{2}}\left[e^{-jk_o\left(x+\frac{a}{2}\right)} - e^{+jk_o\left(x+\frac{a}{2}\right)}\right], \end{aligned}$$

$$E_y = -2jZ_o Be^{-jk_o\frac{a}{2}}\sin\left[k_o\left(x+\frac{a}{2}\right)\right]. \tag{5.16a}$$

Similarly,

$$H_z = Be^{-jk_o a}e^{-jk_o x} + Be^{+jk_o x},$$

$$H_z = 2Be^{-jk_o\frac{a}{2}}\cos\left[k_o\left(x+\frac{a}{2}\right)\right]. \tag{5.16b}$$

Now we can solve for the impedance of the free space region as $Z = -E_y / H_z$

$$Z_o = -\frac{E_y}{H_z} = jZ_o\tan\left[k_o\left(x+\frac{a}{2}\right)\right], \quad 0 \le \left(x+\frac{a}{2}\right) \le \frac{a-w}{2}. \tag{5.17}$$

The second boundary condition exists at $x = -w / 2$ where the tangential fields at the boundary are equal. In this case, there are two tangential fields in E_y and H_z. At the boundary, we have the following three conditions

$$E_y^-\Big|_{x=-\frac{w}{2}} = E_y^+\Big|_{x=-\frac{w}{2}}, \tag{5.18a}$$

$$H_z^-\Big|_{x=-\frac{w}{2}} = H_z^+\Big|_{x=-\frac{w}{2}}, \tag{5.18b}$$

$$Z_o\Big|_{x=-\frac{w}{2}}^- = Z_1\Big|_{x=-\frac{w}{2}}^+. \tag{5.18c}$$

Plugging equations 5.7a and 5.7b into equations 5.18a and 5.18b yields the following set of equations

$$-2jBe^{-jk_o\frac{a}{2}}\sin\left[k_o\left(\frac{a-w}{2}\right)\right] = \sqrt{\frac{\mu_z}{\varepsilon_y}}\left(Ce^{-j\beta_1\frac{w}{2}} - De^{+j\beta_1\frac{w}{2}}\right), \tag{5.19}$$

$$2Be^{-jk_o\frac{a}{2}}\cos\left[k_o\left(\frac{a-w}{2}\right)\right] = Ce^{-j\beta_1\frac{w}{2}} - De^{+j\beta_1\frac{w}{2}}. \tag{5.20}$$

This gives us two equations to solve for three unknowns. In order to solve for the third unknown, we can match equation 5.17 to the impedance in the anisotropic region at $x = -w / 2$. Again we solve for $Z = -E_y / H_z$ from equations 5.16a and 5.16b

$$Z_1 = Z_o\sqrt{\frac{\mu_z}{\varepsilon_y}}\left[\frac{De^{+j\beta_1 x} - Ce^{-j\beta_1 x}}{De^{+j\beta_1 x} + Ce^{-j\beta_1 x}}\right] = Z_o\sqrt{\frac{\mu_z}{\varepsilon_y}}\left[\frac{1-\rho e^{-j2\beta_1 x}}{1+\rho e^{-j2\beta_1 x}}\right], \tag{5.21a}$$

$$|Z_1| = Z_o\sqrt{\frac{\mu_z}{\varepsilon_y}}, \tag{5.21b}$$

$$\rho = \frac{C}{D}. \tag{5.22}$$

Now applying boundary condition 5.18c to equations 5.17 and 5.21a

$$Z_o\sqrt{\frac{\mu_z}{\varepsilon_y}}\left[\frac{1-\rho e^{j\beta_1 w}}{1+\rho e^{j\beta_1 w}}\right] = jZ_o\tan\left[k_o\left(\frac{a-w}{2}\right)\right],$$

$$\left[\frac{1-\rho e^{j\beta_1 w}}{1+\rho e^{j\beta_1 w}}\right] = j\sqrt{\frac{\varepsilon_y}{\mu_z}}\tan\left[k_o\left(\frac{a-w}{2}\right)\right] = j\Psi,$$

$$1-\rho e^{j\beta_1 w} = j\Psi + j\Psi\rho e^{j\beta_1 w},$$

$$1-j\Psi = j\Psi\rho e^{j\beta_1 w} + \rho e^{j\beta_1 w},$$

$$\rho = \frac{1-j\Psi}{1+j\Psi}e^{-j\beta_1 w} = e^{-j2\pi\sqrt{\mu_z\varepsilon_y}\frac{w}{\lambda}}\left\{\frac{1-j\sqrt{\frac{\varepsilon_y}{\mu_z}}\tan\left[\pi\left(\frac{a-w}{\lambda}\right)\right]}{1+j\sqrt{\frac{\varepsilon_y}{\mu_z}}\tan\left[\pi\left(\frac{a-w}{\lambda}\right)\right]}\right\}. \tag{5.23}$$

Substituting equation 5.23 into 5.21 gives us our third equation along with equations 5.19 and 5.20 to solve for the three unknowns *B*, *C* and *D*.

5.2.4 Solving for the Anisotropic Transverse Resonance Condition

If we view figure 5.8 as a transmission line representation of our problem, we can solve for L_g in terms of *w* for a given λ_o. We use the input impedance transformations of transmission line theory to calculate $\vec{Z}_{in}$ at *x* = 0. Then by symmetry the transverse resonance condition simplifies to $\vec{Z}_{in} = 0$ or $\vec{Y}_{in} = 0$.

Starting at *x* = -*a* / 2, we can calculate $\vec{Z}_{in}$ at *x* = -*w* / 2 by

$$\vec{Z}_\alpha = jZ_o \tan\left[k_o L_g\right]. \tag{5.24}$$

We can now calculate $\vec{Z}_{in}$ at *x* = 0 as

$$\vec{Z}_\Omega = Z_1 \frac{\vec{Z}_\alpha + jZ_1 \tan\left(\beta_1 \frac{w}{2}\right)}{Z_1 + j\vec{Z}_\alpha \tan\left(\beta_1 \frac{w}{2}\right)}. \tag{5.25}$$

The transverse resonance condition simplifies equation 5.25 to

$$Z_1 + j\vec{Z}_\alpha \tan\left(\beta_1 \frac{w}{2}\right) = 0 . \tag{5.26}$$

Plugging equations 5.21b and 5.23 into equation 5.26 yields the following equation for L_g

$$Z_o\sqrt{\frac{\mu_z}{\varepsilon_y}} - Z_o \tan\left(k_o L_g\right)\tan\left(k_o\sqrt{\mu_z\varepsilon_y}\,\frac{w}{2}\right) = 0 ,$$

$$\frac{L_g}{\lambda} = \frac{1}{2\pi}\tan^{-1}\left[\frac{\sqrt{\frac{\mu_z}{\varepsilon_y}}}{\tan\left(\frac{\pi w}{\lambda}\sqrt{\mu_z\varepsilon_y}\right)}\right]. \tag{5.27}$$

For the isotropic case, L_g depended on both μ_r and ε_r which means all six permittivity and permeability tensor elements affected the return loss of the antenna. Ultimately, we see from appendix B that the permeability value in the direction of the magnetic field at the aperture is what determines the best return loss for our antenna. Now we see that as we change this tensor value (μ_x), there will be no effect on the taper of the cavity. Figure 5.9 shows the relationship between the ratio of μ_z / ε_y and the shape of the cavity.

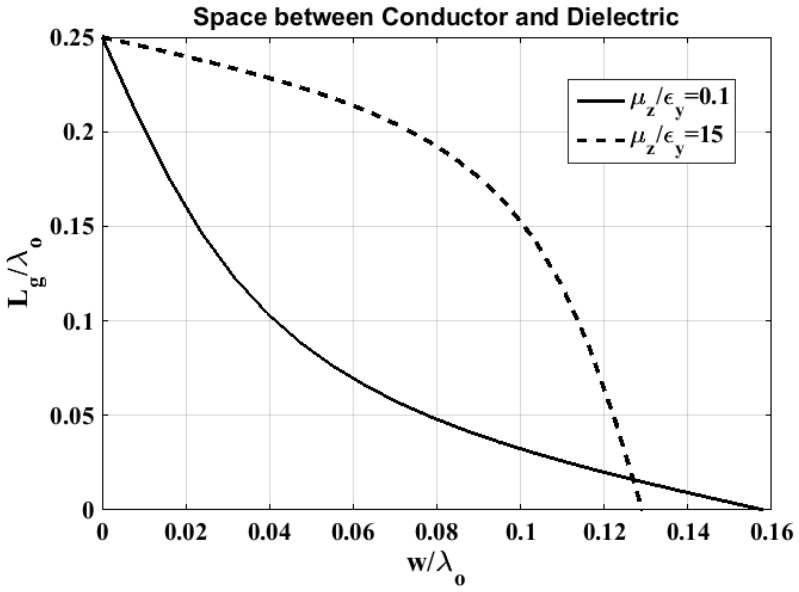

Figure 5.9: Plot of equation 5.27 for various ratios of μ_z / ε_y with an assumed 3.3 inch depth.

Equation 5.27 is closely related to equation 4.14. In fact, this is the exact same equation if we substitute the anisotropic characteristic impedance of $Z_1 = Z_o\sqrt{\mu_z/\varepsilon_y}$ for the isotropic characteristic impedance of $Z_1 = Z_o\sqrt{\mu_r/\varepsilon_r}$ in equation 4.14. Intuitively, this makes sense because by definition we can define an isotropic medium by the anisotropic tensors

$$\underline{\underline{\mu_r}} = \begin{bmatrix} \mu_r & 0 & 0 \\ 0 & \mu_r & 0 \\ 0 & 0 & \mu_r \end{bmatrix},$$

$$\underline{\underline{\varepsilon_r}} = \begin{bmatrix} \varepsilon_r & 0 & 0 \\ 0 & \varepsilon_r & 0 \\ 0 & 0 & \varepsilon_r \end{bmatrix}.$$

In this specialized case, equation 5.27 simplifies to equation 4.14 because $\mu_z = \mu_r$ and $\varepsilon_y = \varepsilon_r$. For this reason, we expect figure 5.10 to be an exact copy of figure 4.4 when utilizing identical ratios of μ_z / ε_y and μ_z / ε_y, and this is the case.

5.3. Tapered LPA design: Anisotropic Ferrite ($\mu_x = \mu_z = 15$, $\varepsilon_y = 1$)

This section describes the numerical calculation of the LPA design shown in figure 5.10 using CST Microwave Studio 2014. We partially load the tapered cavity with a hypothetical magnetic medium exhibiting the following anisotropic tensors

$$\underline{\underline{\mu_r}} = \begin{bmatrix} 15 & 0 & 0 \\ 0 & 1 & 0 \\ 0 & 0 & 15 \end{bmatrix}, \tag{5.28a}$$

$$\underline{\underline{\varepsilon_r}} = \begin{bmatrix} 1 & 0 & 0 \\ 0 & 1 & 0 \\ 0 & 0 & 1 \end{bmatrix}, \tag{5.28b}$$

with $\tan\delta = 0$ in all three Cartesian directions. The values of the two dominant axes are an averaged version of the real part of the permeability in figure 5.1. We feed the LPA using the same type of balanced, symmetric two-port feed from section 4.2. Figure 5.10 shows the geometry of the tapered cavity when $\mu_z / \varepsilon_y = 15$. We show the CST model used in the numerical calculations in figure 5.11. We base the $\underline{\underline{\mu_r}}$ tensor values on those in figure 5.1 through figure 5.3. We assume lossless material for the initial designs. Table 5.1 gives the normalized dimensions of this antenna design in terms of λ_o.

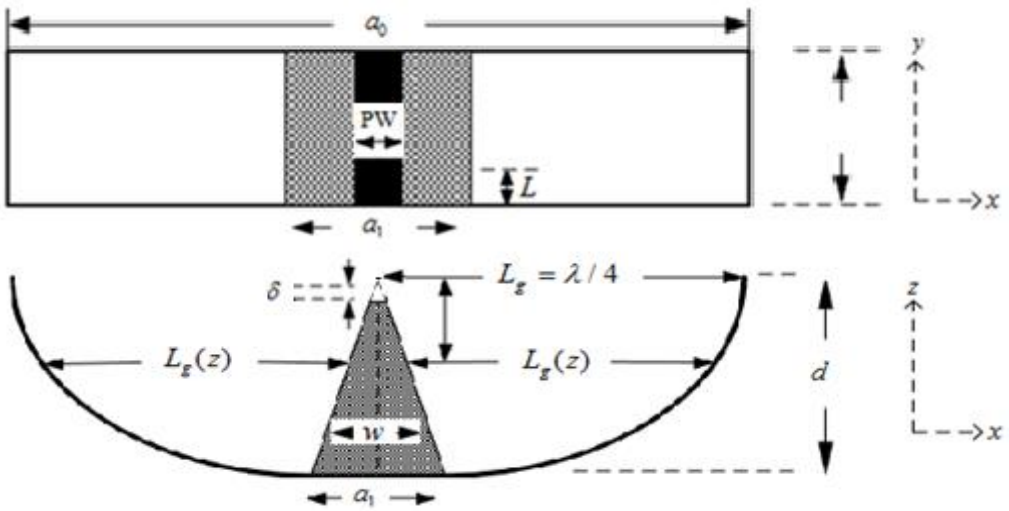

Figure 5.10: The geometry of the anisotropic tapered LPA when $\mu_z / \varepsilon_y = 15$.

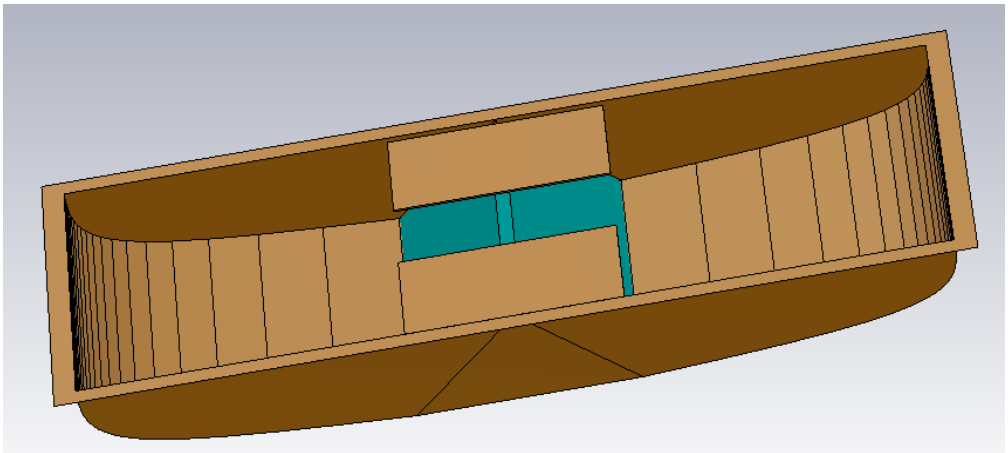

Figure 5.11: The CST model of the anisotropic tapered LPA when $\mu_z / \varepsilon_y = 15$.

Table 5.1: Normalized dimensions for the tapered cavity model given in figure 5.10.

a_0	b	a_1	d	δ	PW	L
$\lambda_o/2$	$\lambda_o/4.5$	$a_o/(\mu_d \varepsilon_d)^{0.5}$	$0.04\lambda_o$	$0.003\lambda_o$	$\lambda_o/8$	$0.08\lambda_o$

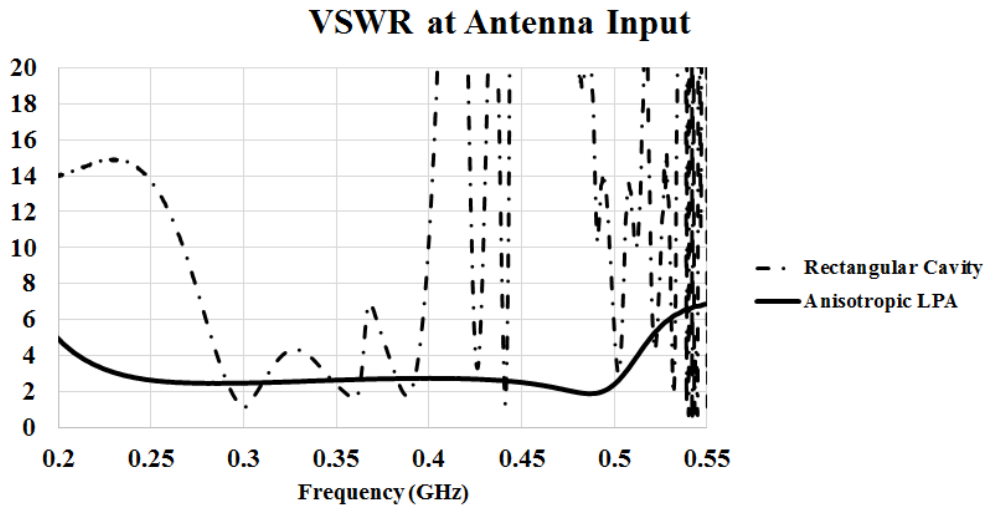

Figure 5.12: VSWR of the loaded FLPA and the tapered anisotropic LPA.

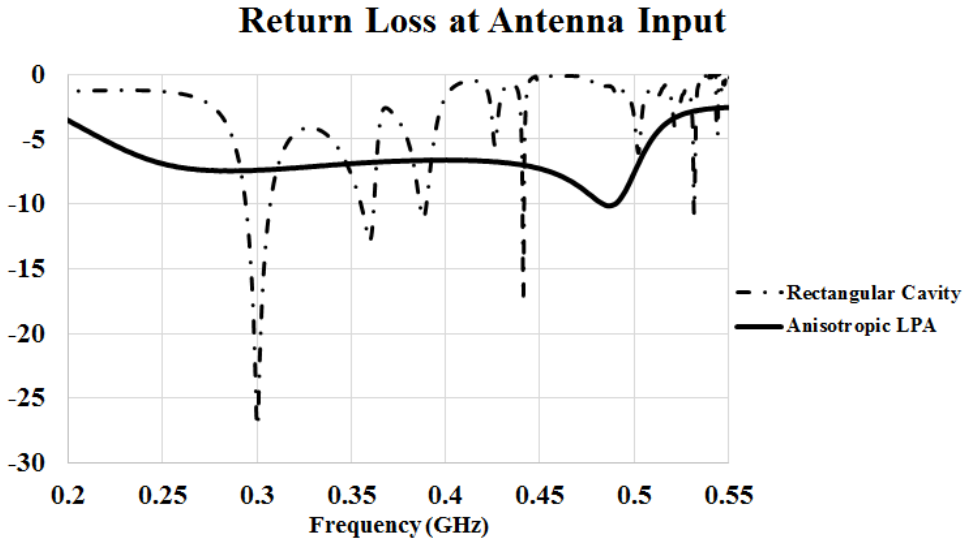

Figure 5.13: Return loss of the loaded FLPA and the tapered anisotropic LPA.

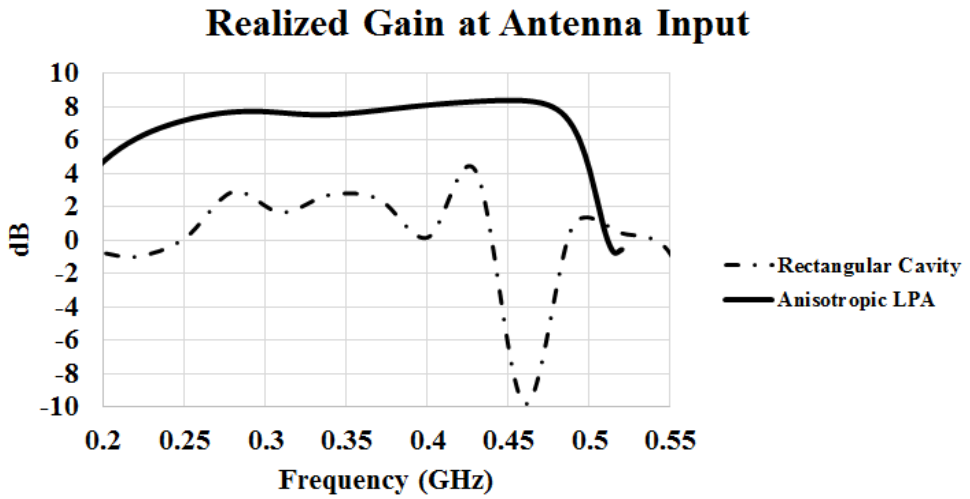

Figure 5.14: Realized gain of the loaded FLPA and the tapered anisotropic LPA.

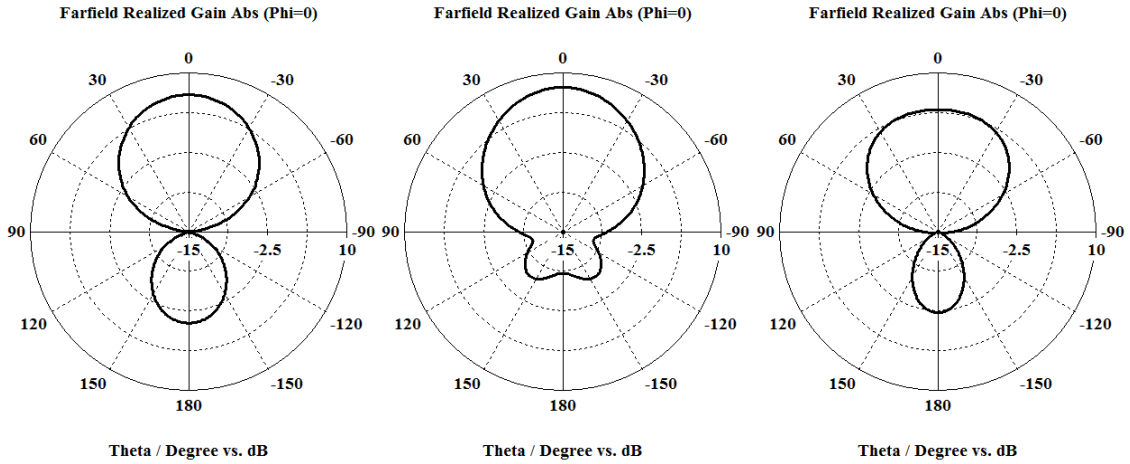

(a) (b) (c)

Figure 5.15: Polar plots of the far field radiation patterns of the anisotropic LPA. (a) 230 MHz. (b) 365 MHz. (c) 500 MHz.

Figure 5.12 through figure 5.14 compares the VSWR, return loss, and realized gain of the anisotropic LPA in figure 5.10 to that of the antenna in figure 3.17. The solid curve shows the results of the tapered cavity design with λ_o = 2.0 m (150 MHz), and the dashed curve shows the results of the loaded FLPA with λ_o = 1.5 m (200 MHz). Figures 5.15a through figure 5.156c show the radiation plots at $\phi = 0^o$ across the bandwidth at

230 MHz, 365 MHz, and 500 MHz. These plots achieve peak realized gain values at bore sight of 6.55 dB, 7.74 dB, and 4.24 dB respectively.

Figure 5.12 and figure 5.13 show that partially loading the cavity with an anisotropic magnetic medium yields a very flat wideband response. In fact, we see a VSWR of less than 3 and a return loss less than -6 dB from 230 MHz to 505 MHz (1.2 octaves). While a VSWR of 3 is not as desirable as a VSWR of 2, it is still useable in most applications and the high realized gain of figure 5.15 justifies this.

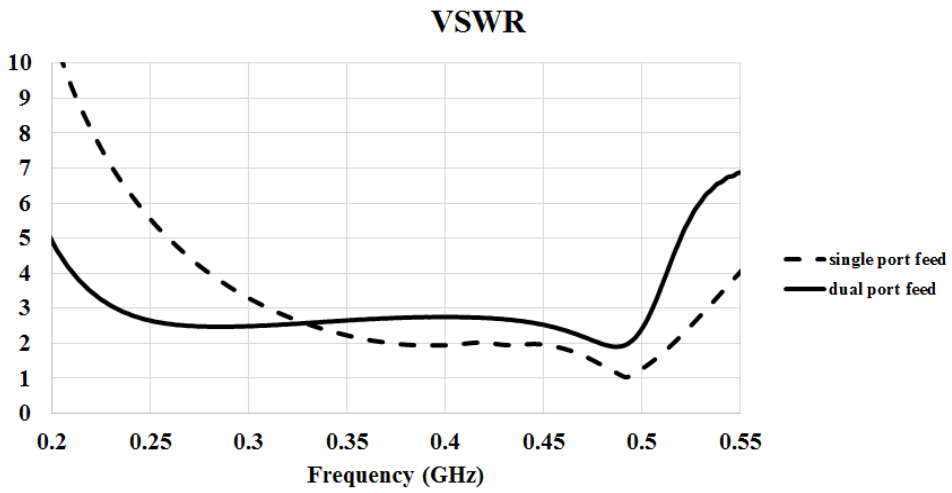

Figure 5.16: VSWR of the anisotropic LPA utilizing a single port and a dual port matching network.

Figure 5.14 shows we significantly improve the realized gain over the non-tapered cavity of section 3.3 from 200 MHz to 505 MHz with up to a 6.0 dB improvement. From 200 MHz to 505 MHz the anisotropic LPA model produces a positive realized gain with a cavity profile of $d = 0.04\lambda_o$. Looking more closely at figure 5.14, we see a dramatic decline in the realized gain manifest itself at about 505 MHz for the anisotropic LPA. This corresponds to the degradation in VSWR and return loss seen in the figure 5.12 and figure 5.13.

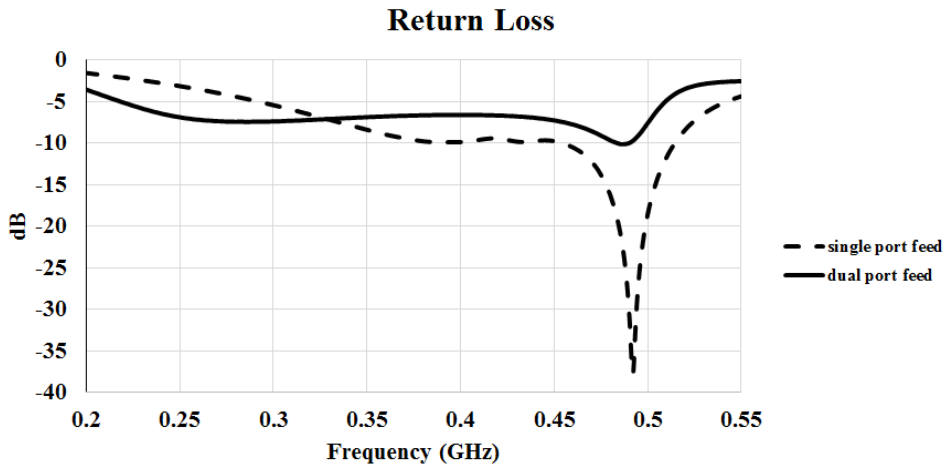

Figure 5.17: Return loss of the anisotropic LPA utilizing a single port and a dual port matching network.

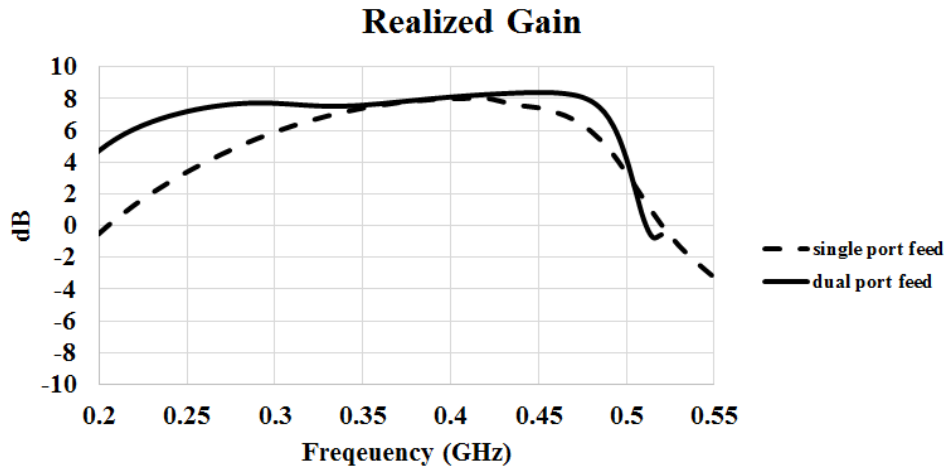

Figure 5.18: Realized gain of the anisotropic LPA utilizing a single port and dual port matching network.

In our proposal, we demonstrated a viable anisotropic LPA design utilizing a tapered cavity similar to that of figure 5.11, but utilizing only a single port matching network (see appendix B.6). Figure 5.16 through figure 5.18 compares the VSWR, return loss, and realized gain of the anisotropic LPA in figure 5.10 to that of the LPA in appendix B.6. Furthermore, we were basing the taper of our cavity on the isotropic

transverse resonance formulation of section 4.1. We gave the tensors for this single-port, anisotropic LPA as

$$\underline{\underline{\mu_r}} = \begin{bmatrix} 15 & 0 & 0 \\ 0 & 1 & 0 \\ 0 & 0 & 1 \end{bmatrix}, \tag{5.29a}$$

$$\underline{\underline{\varepsilon_r}} = \begin{bmatrix} 1 & 0 & 0 \\ 0 & 1 & 0 \\ 0 & 0 & 1 \end{bmatrix}. \tag{5.29b}$$

Because of our incomplete understanding of the anisotropic transverse resonance at that time, we were utilizing a tapered cavity even though the ratio that determines the characteristic impedance of the anisotropic region was $\mu_z / \varepsilon_y = 1$. With $\mu_z = \varepsilon_y = 1$, the anisotropic medium would have the same characteristic impedance as air negating the need for a taper. In this case, tapering the cavity actually increases the resonant frequency as you travel down the cavity in the normal direction. We believe this is why the two-port matching network yields a higher realized gain than the single-port matching network from 400 MHz to 500 MHz even though the single-port matching network yields a better return loss and VSWR. This is due to a reduction in radiation efficiency caused by the distortion of the resonances in the cavity. We also clearly see the improvement in the VSWR, return loss, and realized gain of the two-port matching network compared to the one-port matching network below 310 MHz. This increases the bandwidth from 0.73 octaves to 1.2 octaves while improving the realized gain up to 5.0 dB at the sacrifice of a slightly degraded impedance match above 325 MHz.

5.4 Non-Tapered LPA Design: Anisotropic Ferrite ($\varepsilon_y = \mu_z = 1$, $\mu_x = 15$)

In section 5.2, we discuss the negative effects of tapering the cavity of the anisotropic LPA when $\mu_z = \varepsilon_y = 1$. In this section, we investigate a non-tapered anisotropic LPA to this effect. If we can achieve similar performance to the tapered anisotropic LPA of section 5.2, then this greatly simplifies the manufacturing process of the cavity. In addition, appendix A describes limitations in the ability to produce high permeability on multiple axes of the $\underline{\underline{\mu}}_r$ tensor. The manufacturer can produce higher values of permeability with lower loss tangent on a single axis of the $\underline{\underline{\mu}}_r$ tensor versus two axes. Therefore, if we can produce similar results utilizing only one axis of the $\underline{\underline{\mu}}_r$ tensor by keeping $\mu_y = \mu_z = 1$, then this gives the engineer more flexibility in their value of the tensor's dominant axis.

We partially load the cavity with a hypothetical magnetic medium exhibiting the following anisotropic tensors

$$\underline{\underline{\mu}}_r = \begin{bmatrix} 15 & 0 & 0 \\ 0 & 1 & 0 \\ 0 & 0 & 1 \end{bmatrix}, \tag{5.30a}$$

$$\underline{\underline{\varepsilon}}_r = \begin{bmatrix} 1 & 0 & 0 \\ 0 & 1 & 0 \\ 0 & 0 & 1 \end{bmatrix}, \tag{5.30b}$$

with $\tan\delta = 0$ in all three Cartesian directions. Again we base our value for μ_x on the real part of figure 5.1. We feed the LPA using the same type of balanced, symmetric two-port feed from section 4.2. Figure 5.19 shows a diagram of the non-tapered cavity when $\mu_z / \varepsilon_y = 1$. We show the CST model used in the numerical calculations in figure 5.20. We

assume lossless material for these designs. Table 5.2 gives the normalized dimensions of this antenna design in terms of λ_o.

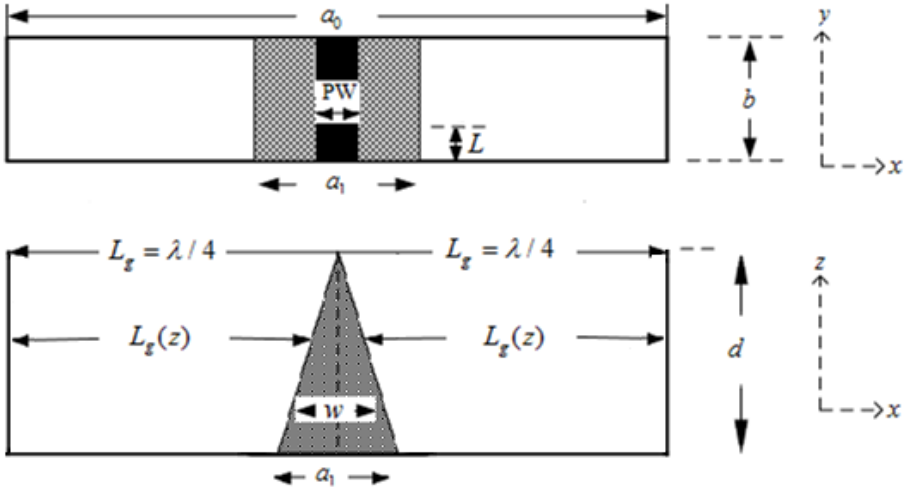

Figure 5.19: The geometry of the non-tapered anisotropic LPA when $\mu_z / \varepsilon_y = 1$.

Table 5.2. Normalized dimensions for non-tapered anisotropic LPA model in figure 5.19.

a_0	b	a_1	d	δ	PW	L
$\lambda_o/2$	$\lambda_o/4.5$	$a_o/(\mu_d \varepsilon_d)^{0.5}$	$0.04\lambda_o$	$0.003\lambda_o$	$\lambda_o/8$	$0.08\lambda_o$

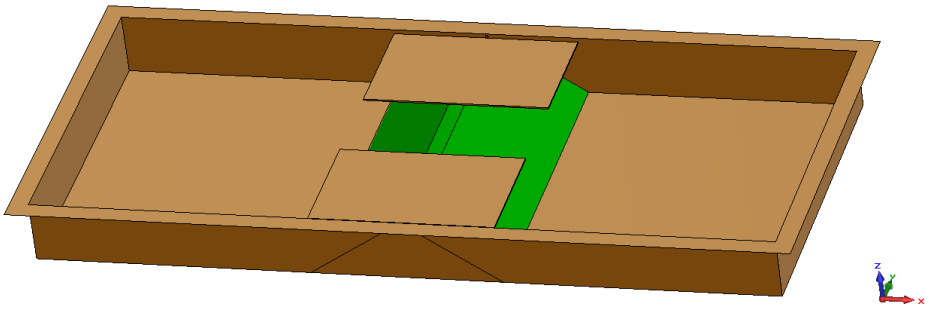

Figure 5.20: The CST model of the non-tapered anisotropic LPA when $\mu_z / \varepsilon_y = 1$.

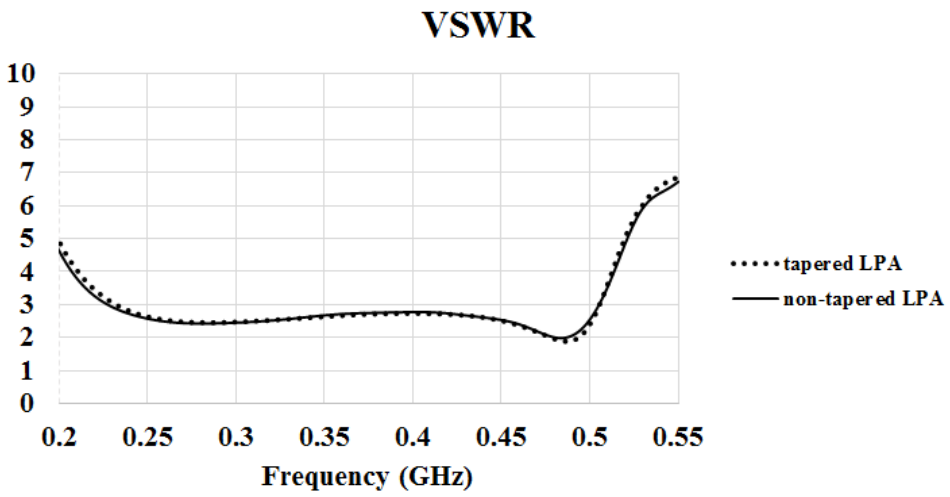

Figure 5.21: VSWR of the tapered and non-tapered anisotropic LPA designs.

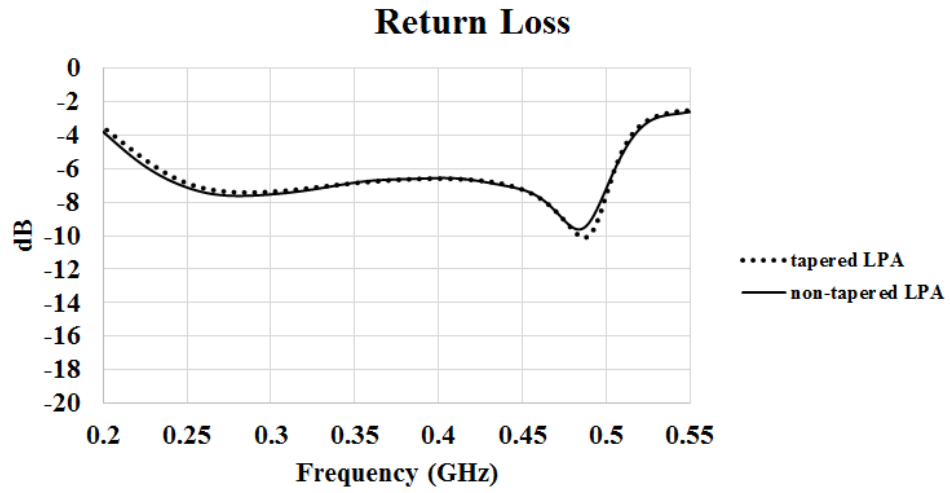

Figure 5.22: Return loss of the tapered and non-tapered anisotropic LPA designs.

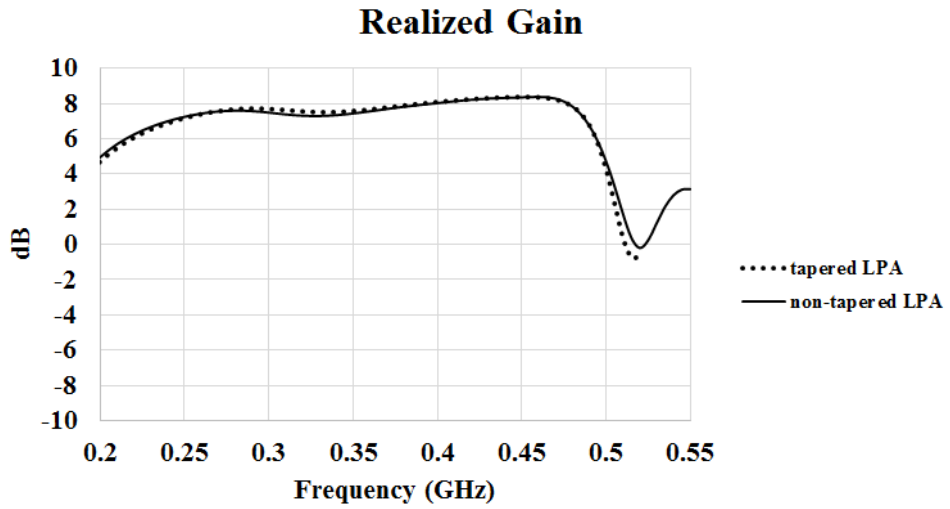

Figure 5.23: Realized gain of the tapered and non-tapered anisotropic LPA designs.

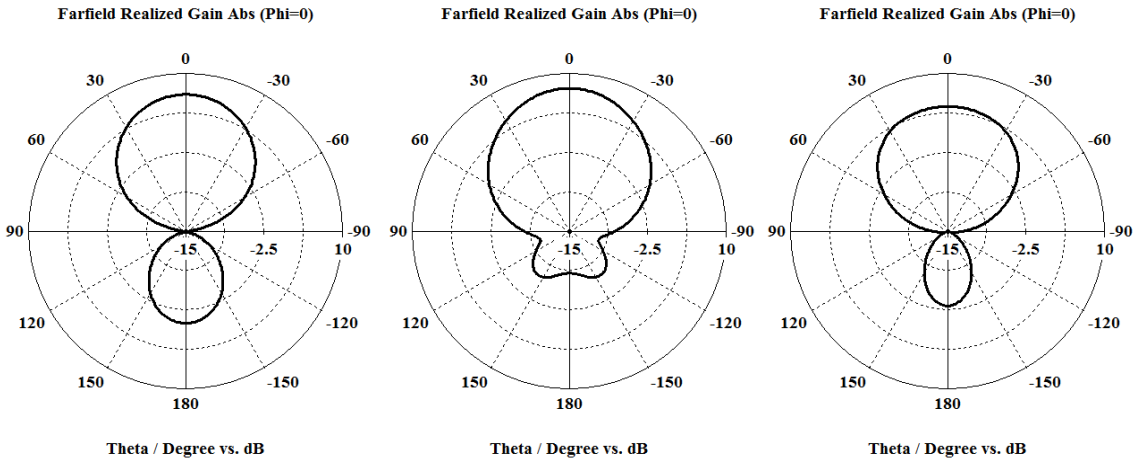

(a) (b) (c)

Figure 5.24: Polar plots of the far field radiation patterns of the non-tapered anisotropic LPA. (a) 230 MHz. (b) 365 MHz. (c) 500 MHz.

Figure 5.21 through figure 5.23 compares the VSWR, return loss, and realized gain of the non-tapered anisotropic LPA in figure 5.19 to that of the tapered anisotropic LPA of section 5.2. The solid curve shows the results of the tapered cavity design with λ_o = 2.0 m (150 MHz), and the dashed curve shows the results of the non-tapered cavity design with λ_o = 2.0 m (150 MHz). Figure 5.24a through figure 5.24c show the radiation

plots at $\phi = 0^o$ across the bandwidth at 230 MHz, 365 MHz, and 500 MHz. These plots achieve peak realized gain values at boresight of 6.67 dB, 7.63 dB, and 4.74 dB respectively.

These figures show nearly identical performance in VSWR, return loss, and realized gain versus frequency with no change in cavity profile. This means that the wideband performance depends more on a constant resonance frequency as opposed to the magnitude of the ratio μ_z / ε_y. Furthermore, the impedance match depends on the relationship between the dimensions of the tuning network and the value of the $\underline{\underline{\mu_r}}$ tensor in the horizontal direction.

5.4.1 Scaling the Design in Frequency

This section demonstrates the ability to scale the design with frequency. We use the same model and normalized dimensions as in figure 5.19 and table 5.2. Similarly, we use the same anisotropic tensors as equations 5.24a and 5.24b. Theoretically we should be able to shift the results of figure 5.21 through figure 5.23 to any frequency band by simply changing the value of λ_o since all dimensions are normalized to this variable.

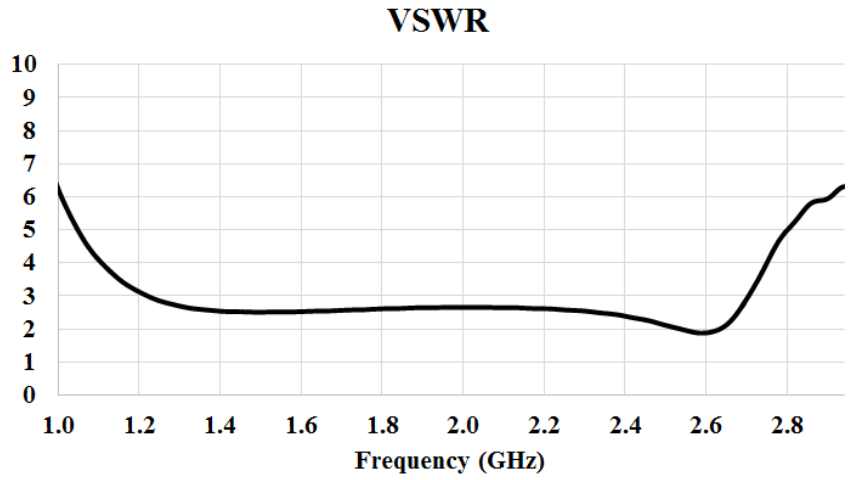

Figure 5.25: VSWR of the non-tapered anisotropic LPA with $\lambda_o = 0.375$ m.

Figure 5.26: Return loss of the non-tapered anisotropic LPA with $\lambda_o = 0.375$ m.

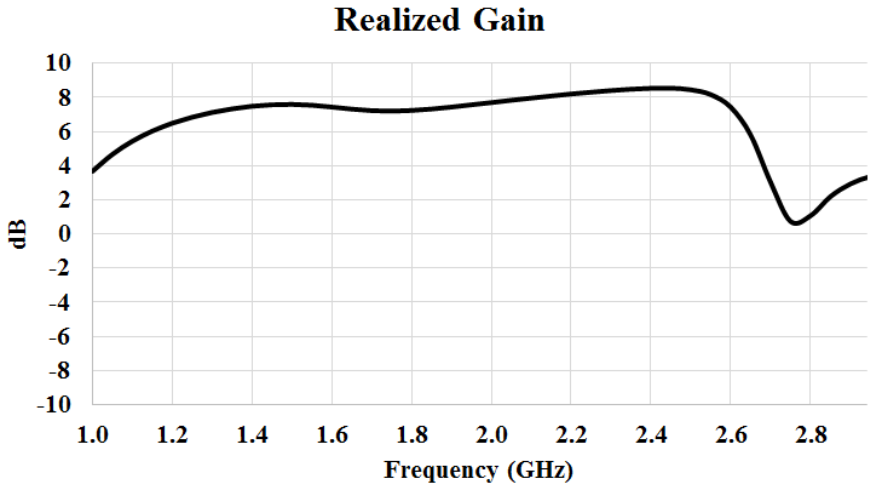

Figure 5.27: Realized gain of the non-tapered anisotropic LPA with $\lambda_o = 0.375$ m.

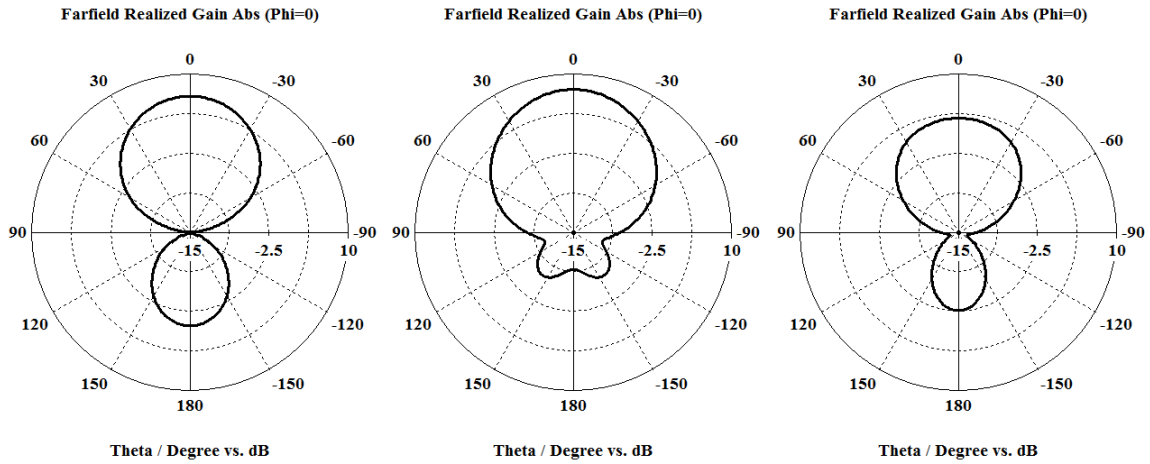

(a) (b) (c)

Figure 5.28: Polar plots of radiation patterns of the anisotropic LPA with $\lambda_o = 0.375$ m.

(a) 1.2 GHz. (b) 1.95 GHz. (c) 2.7 GHz.

Figure 5.25 through figure 5.27 show the VSWR, return loss, and realized gain of the non-tapered anisotropic LPA in figure 5.19 for $\lambda_o = 0.375$ m. From the VSWR and return loss, we see a -6 dB bandwidth from 1.2 GHz to 2.7 GHz or 1.2 octaves. Similarly, we see an identical realized gain curve to that of the non-tapered anisotropic LPA. The only difference is that the curve shifts up in frequency corresponding to the reduction in λ_o from 1.5 m to 0.375 m. Figure 5.28a through figure 5.28c show the radiation plots at $\phi = 0^o$ across the bandwidth at 1.2 GHz, 1.95 GHz, and 2.7 GHz. These plots achieve peak realized gain values at boresight of 6.49 dB, 7.57 dB, and 3.03 dB respectively. The profile of this scaled design remains $d = 0.04\lambda_o$, which at these frequencies yields a 0.62 inch LPA profile.

We maintain that while the reduction in electrical height is a constant when normalized by λ_o, the reduction in actual height is much more dramatic at low UHF frequencies where we have focused the work in this dissertation. This stems from the

fact that λ_o is much larger at these frequencies. Moreover, there are limitations on the manufacture of these anisotropic media, as outlined in appendix B, that limit their operation to below 1.5 GHz depending on tolerance for loss tangent and values of the permeability tensor. However, the results of this section are important because they show the anisotropic LPA design scales to higher frequencies easily. As Metaferrite technology continues to mature, and higher frequencies become available to engineers, we can create very thin antennas for application spaces in higher frequency bands.

5.4.2 Introduction of Losses to the Model

Thus far, all designs and simulations of the anisotropic LPA designs assume that the anisotropic medium is lossless. However, we know from appendix A that the loss tangents of $\underline{\underline{\boldsymbol{\mu}}}_r$ in the dominant axis can be as high as $\tan\delta = 0.25$. This is a very high loss tangent, and therefore we expect the introduction of loss on this order to have noticeable effects on the VSWR, return loss, and realized gain of our non-tapered anisotropic LPA design of section 5.3. Specifically we expect that as loss tangent increases with frequency we will see a reduction in total antenna efficiency due to the loss of power as the electric and magnetic fields travel through the lossy medium. Therefore, we will use the measured data of $\underline{\underline{\boldsymbol{\mu}}}_r$ from figure 5.1 through figure 5.3 to analyze how losses will affect the performance of the non-tapered anisotropic LPA design. We use the same geometry and CST model as in figure 5.19 and figure 5.20 respectively; however, we substitute the lossy parameters of figure 5.1 through figure 5.3 for the $\underline{\underline{\boldsymbol{\mu}}}_r$ tensor, while we keep $\underline{\underline{\boldsymbol{\varepsilon}}}_r = \varepsilon_r \underline{\underline{\boldsymbol{I}}}$. We use the same dimensions as in table 5.2.

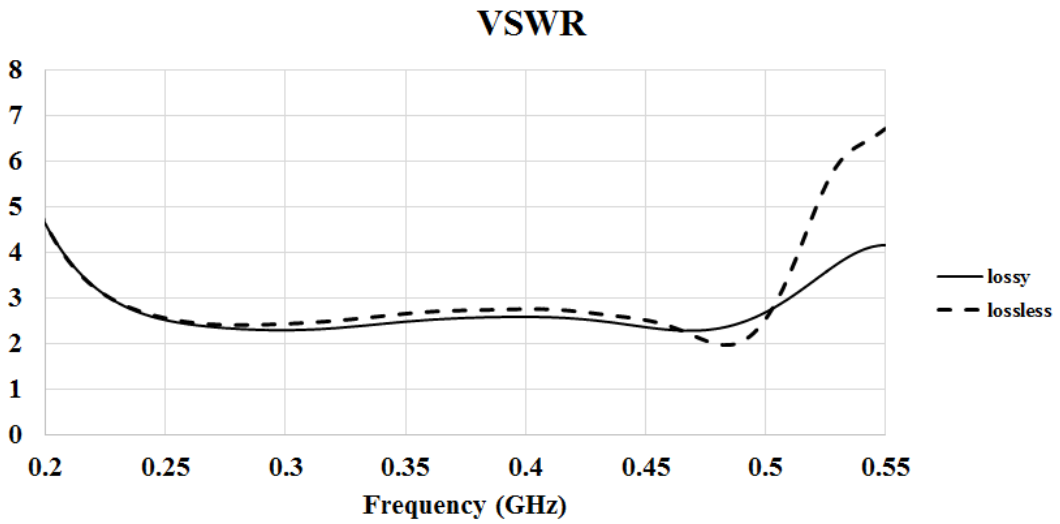

Figure 5.29: Comparison of VSWR for the lossy and lossless media in the non-tapered anisotropic LPA design.

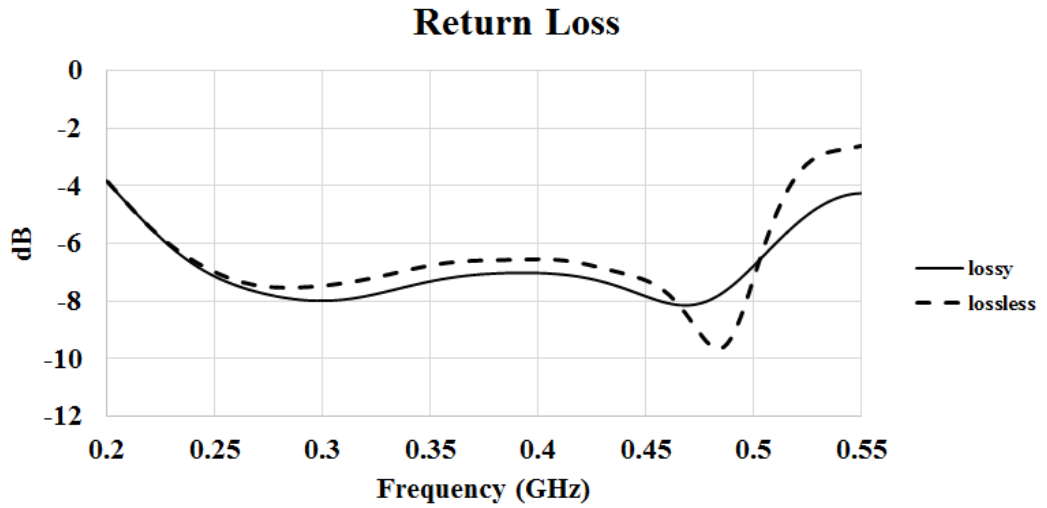

Figure 5.30: Comparison of return loss for the lossy and lossless media in the non-tapered anisotropic LPA design.

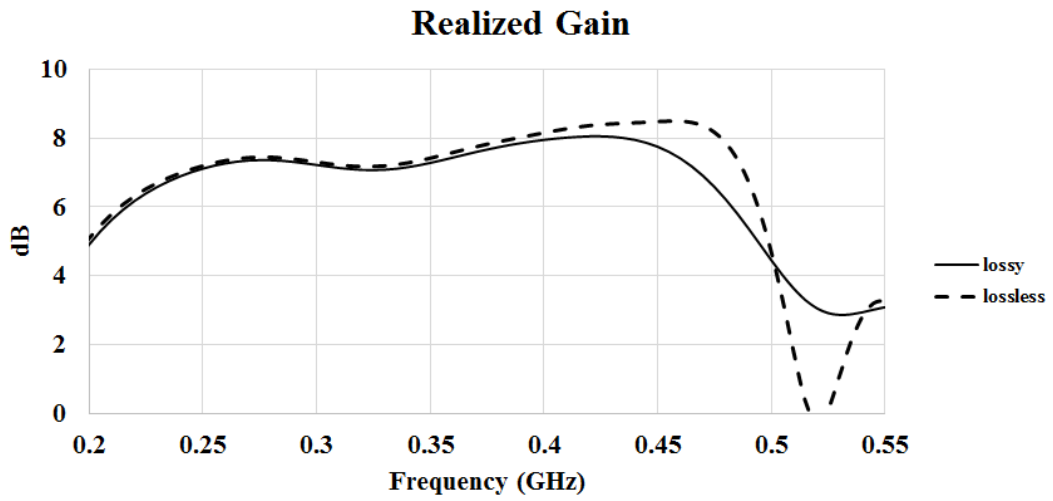

Figure 5.31: Comparison of realized gain for the lossy and lossless media in the non-tapered anisotropic LPA design.

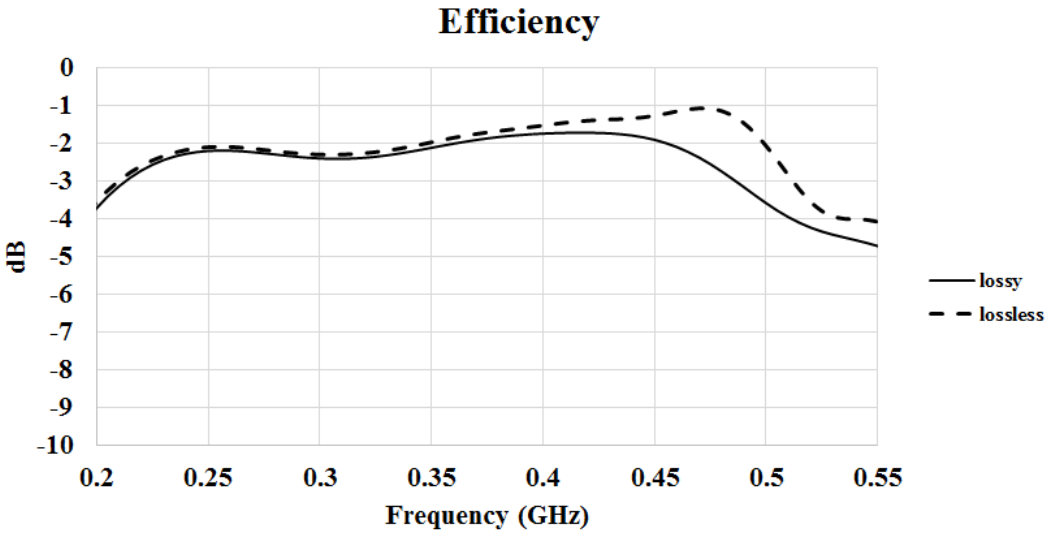

Figure 5.32: Comparison of antenna efficiency for the lossy and lossless media in the non-tapered anisotropic LPA design.

Figure 5.29 through figure 5.31 shows comparisons of the VSWR, return loss, realized gain, and antenna efficiency for both the lossy and lossless media. The efficiency is a measure of how much power an antenna radiates versus how much power the waveguide port provides to the antenna. This takes into account the power loss due to

the loss tangent in the anisotropic medium. Generally speaking, we expect the introduction of material losses to the model to improve the impedance match because there is less total power to reflect back to the waveguide port. We see in figure 5.29 and figure 5.30 that both the VSWR and return loss curves show a slight improvement across most of the frequency band and a more drastic improvement where the loss tangent is highest at 500 MHz and above.

Since we know realized gain utilizes efficiency as part of its calculation from equation1.4, we expect a close correlation between figure 5.31 and figure 5.32. We see this up to around 500 MHz. Beyond this we see the realized gain of the lossy LPA approach that of the lossless LPA even though the efficiency of the lossless LPA remains higher. This highlights an important tradeoff in the use of lossy media. We already highlighted how a lossy media will reduce antenna efficiency while at the same time improving the impedance match at the antenna input. We see from figure 5.29 and figure 5.30 that above 500 MHz the impedance match of the lossy LPA is better than that of the lossless LPA. This helps make up for the fact that the antenna efficiency of the lossy LPA is lower than that of the lossless LPA. In conclusion, we see that even introducing relatively high loss tangents for a single axis of $\underline{\mu}_r$ does not drastically affect the performance of the non-tapered anisotropic LPA.

5.5 Comparison of Non-tapered Anisotropic LPA Design to Isotropic LPA, FLPA, and State of the Art

Using the FLPA design from section 3.2 and the isotropic dielectric LPA design from section 4.3, we compare the non-tapered anisotropic LPA design from section 5.3 highlighting differences in bandwidth, realized gain, and cavity profile.

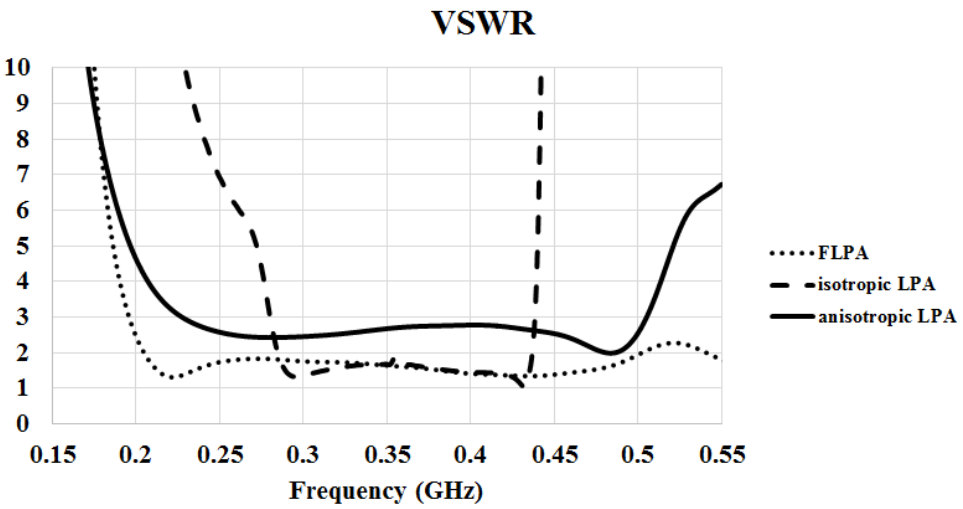

Figure 5.33: VSWR of the FLPA, tapered, dielectric LPA, and non-tapered anisotropic LPA.

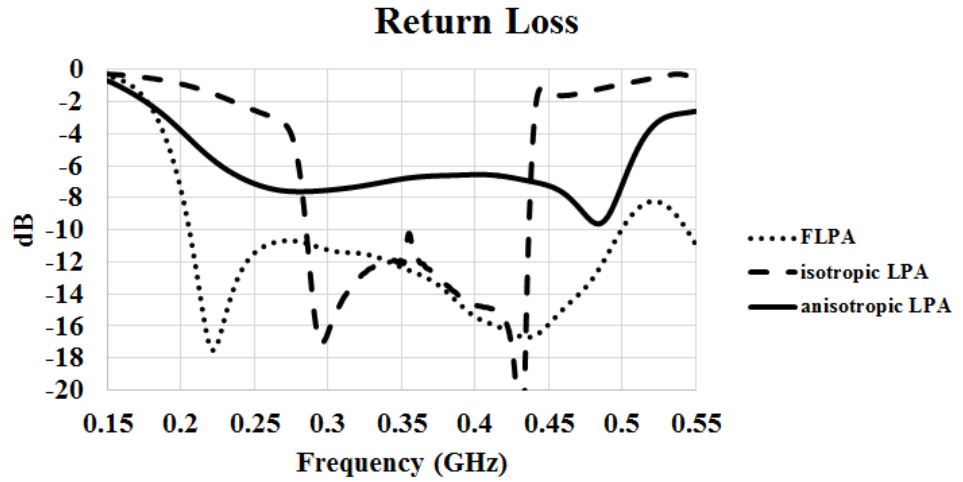

Figure 5.34: Return loss of the FLPA, tapered, dielectric LPA, and non-tapered anisotropic LPA.

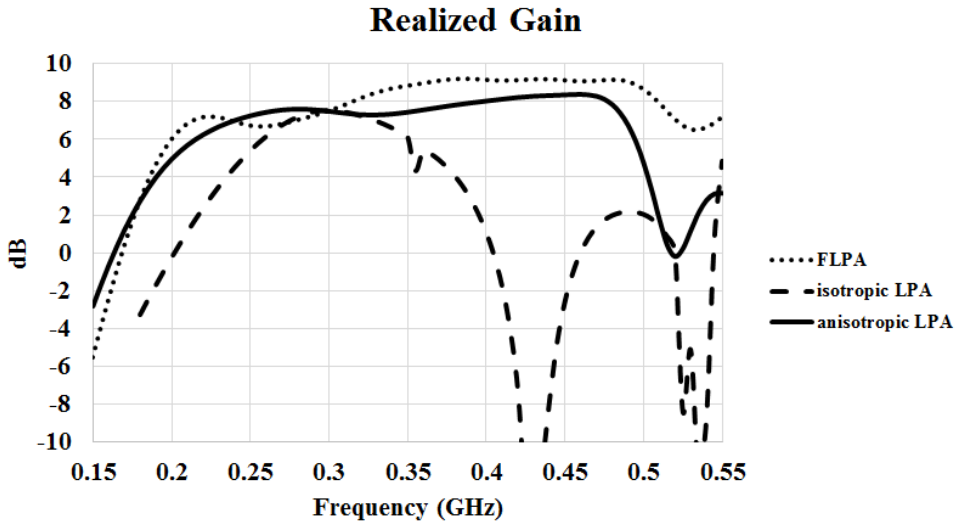

Figure 5.35: Realized gain of the FLPA, tapered dielectric LPA, and non-tapered anisotropic LPA.

Figure 5.33 through figure 5.35 show comparisons of the VSWR, return loss, and realized gain of the FLPA, the tapered dielectric LPA, and the non-tapered anisotropic LPA designs. We calculate the results for λ_o = 1.56 m, λ_o = 2.0 m, and λ_o = 2.0 m respectively. These figures show that the FLPA design is clearly the best in terms of bandwidth with 1.4 octaves of better than -10 dB bandwidth, whereas the dielectric LPA has approximately 0.53 octaves of -10 dB bandwidth, and the non-tapered anisotropic LPA has 1.2 octaves of -6 dB bandwidth.

We see from figure 5.35 that the realized gain of the non-tapered anisotropic LPA is within 1.0 dB of the FLPA across the entire band. The larger aperture size of the non-tapered anisotropic LPA making up for the higher return loss. The non-tapered anisotropic LPA has a realized gain that is far superior to the tapered dielectric LPA from 350 MHz to 500 MHz. This is due to the fact that the quarter wave monopole cancelation of radiation to broadside does not start to take effect until about 485 MHz for the probe

dimensions of the anisotropic LPA design. The performance of the non-tapered anisotropic LPA is especially impressive considering that the electrical height of the profile is $d = 0.04\lambda_o$. This is a 66.7% reduction from the FLPA and a 20.0% reduction from the tapered dielectric LPA.

Table 5.3: Comparison of non-tapered anisotropic LPA to state of the art wideband LPA designs.

reference	**Aperture**	**substrate**	**BW (octaves)**	**gain (dB)**	**profile (λ_o)**
[17]	spiral	dielectric	7.3	-2.6 - 6.9	0.03
[18]	Inverted L	dielectric	0.59	-	0.09
[19]	Bowtie	dielectric	0.77	4.0 - 6.0	0.064
[20]	Discone	none	0.92	-	0.09
[21]	Monopole	HIS/EBG	0.77	7.0 - 10.25	0.1
[22]	Bowtie	HIS/EBG	1.07	3.3 - 9.35	0.05
[23]	dipole	HIS/EBG	0.41	-	0.06
-	FLPA	none	1.44	4.8 - 8.2	0.14
-	tapered cavity	dielectric	0.53	-20.0 – 8.0	0.05
-	Non-tapered cavity	anisotropic	1.2	3.5 – 8.4	0.04

Table 5.3 shows a comparison of the non-tapered anisotropic LPA to the other state of the art LPA designs. The anisotropic LPA outperforms all other linearly polarized LPAs in terms of profile, bandwidth, and realized gain. Take into account that the realized gain of the anisotropic LPA is between 6.0 dB and 8.4 dB from 225 MHz – 495 MHz, and we realize that with a thinner profile and wider bandwidth, the non-tapered anisotropic LPA provides a state of the art LPA with a very simple geometry. Further, the advantages of using anisotropic media versus isotropic media is obvious. Not only is the bandwidth far superior and the profile 20% thinner, but the realized gain doesn't suffer from the cancellation of radiation to broadside in the middle of the VSWR bandwidth like for the two tapered isotropic LPAs. Therefore, we conclude that we

achieve our goal of less than a $0.05\lambda_o$ thick profile with similar performance to an unloaded radiating cavity by utilizing our understanding of transverse resonance developed in section 5.2 for a cavity partially filled with a high index anisotropic medium.

Chapter 6
Conclusions

The goal of this research is to analyze the properties of effective anisotropic media as a means to reduce the profile of a cavity-backed antenna at low UHF. We derive a way to maintain a constant $\lambda_o/2$ resonance between the cavity walls in the presence of high index isotropic and anisotropic media. We achieve this through the use of the transverse resonance condition established in a cavity partially filled with a substrate. We contend the derivation of the anisotropic resonance represents a novel achievement, and furthermore, the application of the technique to our radiating cavity produces a novel geometry for both the isotropic and anisotropic cases.

The final LPA designs produce a tapered dielectric LPA partially loaded with Rogers 6010 substrate. This LPA achieves a 0.53 octave -10 dB bandwidth and positive realized gain over 79% of this bandwidth with a profile of only $0.05\lambda_o$. This provides a cheap solution with a reasonable bandwidth and a profile that compares with the thinnest LPA designs in the literature. We also produce a design for a non-tapered magnetic LPA partially loaded with a hypothetical anisotropic media. This LPA achieves a 1.2 octave -6 dB bandwidth and a realized gain ranging from 3.5 dB – 8.2 dB with a profile of only $0.04\lambda_o$. This is a 21.4% reduction in profile and 126.4% increase in bandwidth over the tapered dielectric design. The non-tapered anisotropic LPA also outperforms other state of the art LPA designs both in terms of profile, bandwidth, and realized gain. Furthermore, it performs on par with a typical $0.14\lambda_o$ air-filled radiating cavity both in terms of impedance match and realized gain, but with a 71.4% reduction in profile.

We arrive at some important conclusions about the constituent design parameters of the non-tapered anisotropic LPA. First, the designer can only hope to achieve a constant resonance frequency with a non-tapered cavity if the values of permeability in the normal direction and permittivity in the vertical direction are unity, i.e. $\mu_z = \varepsilon_y = 1$. This is due to the fact, that the characteristic impedance of the anisotropic medium based on the transverse resonance calculation is $Z_c = Z_o\sqrt{\mu_z/\varepsilon_y}$. Second, in order to achieve the best broadband performance the designer should align the dominant axis of the $\underline{\underline{\mu_r}}$ tensor in the direction of the magnetic field at the aperture. Furthermore, the designer should also keep the ratio of the dominant axis in the $\underline{\underline{\mu_r}}$ tensor to the tensor elements of $\underline{\underline{\varepsilon_r}}$ as high as possible. This allows for the best optimization of the matching network. Lastly, the matching network should consist of a balanced two-port feed fed 180° out of phase. This effectively increases the realized gain by 3 dB and improves the impedance match by negating the reactance caused by the fringing fields of an unbalanced one-port feed. Following these guidelines allows us to utilize anisotropic media in such a way as to push the state of the art in terms of wideband and low profile antenna design at the challenging frequencies of the low UHF band.

6.1 Recommendations for Further Research

This section provides some brief recommendations for further research. First we would like to build a prototype antenna based on the tapered dielectric LPA of section 4.3. This would allow us to verify our isotropic transverse resonance technique via experiment. Due to the complexity of the L_g vs. w equation for the taper of the isotropic cavity, we would need to hire a machine shop to fabricate the cavity. We are unable to produce the precision necessary to accurately manufacture the cavity ourselves.

A second topic of future research would be to design a non-tapered anisotropic LPA that utilizes something more closely resembling a realizable medium. We would like to utilize a uniaxial anisotropic medium whose $\underline{\underline{\varepsilon_r}}$ diagonal elements are equivalent to the ε_r of the metaferrite host substrate. This would correspond to the ε_z data shown in figure A.8 in appendix A. Furthermore, we would like to keep the ratio of μ_x/ε_r the same, since this produces the wideband match we desire. The tensors would then be

$$\underline{\underline{\varepsilon_r}} = \begin{bmatrix} \varepsilon_r & 0 & 0 \\ 0 & \varepsilon_r & 0 \\ 0 & 0 & \varepsilon_r \end{bmatrix},$$

$$\underline{\underline{\mu_r}} = \begin{bmatrix} 15\varepsilon_r & 0 & 0 \\ 0 & 1 & 0 \\ 0 & 0 & 1 \end{bmatrix}.$$

By using these types of tensors and inserting frequency dependent losses, the resulting non-tapered anisotropic LPA would then be theoretically realizable. This would allow us to build and test our designs and compare measurement to simulation. Furthermore, an investigation of increasing the ratio μ_x/ε_r higher than 15 to see if we could further reduce the LPA profile would be interesting. However, at a certain point the value of μ_x will exceed what is possible with current technology. Positive results in this area could help justify further investment to increase the achievable values of $\underline{\underline{\mu_r}}$ and further reduce loss tangents.

References

[1] P. Wade. "Rectangular Waveguide to Coax Transition Design", *QEX*, November/December 2006.

[2] Robert E. Collin, Field Theory of Guided Waves, 2nd Edition, The Institute of Electrical and Electronics Engineers Inc., 345 East 47th St. New York, NY 10017, 1991.

[3] David Pozar, Microwave Engineering, 3rd Edition, John Wiley and Sons, 2005.

[4] A. N. Lagarkov, V. N. Semeneko, V. N. Kisel, and V. A. Christyaev, "Development and Simulation of Microwave Artifical Magnetic Composities Utilizing Non-magnetic Inclusion", *Journal of Magnetism and Magnetic Materials*, vol. 258–259, pp. 161–166, March 2003.

[5] S. Maslovski, P. Ikonen, I. Kolmakov, and S. Tretyakov, "Artificial Magnetic Materials Based on the New Magnetic Particle Metasolenoid", *Progress in Electromagnetics Research*, PIER 54, pp. 61–81, 2005.

[6] Pardavi-Horvath, Martha. "Microwave Applications of Soft Ferrites", *Journal of Magnetism and Magnetic Materials*, vol. 215-216, no. 1, pp. 171-183, 2000.

[7] Kevin Buell, Hossein Mosallaei, and Kamal Sarabandi, "A Substrate for Small Patch Antennas Providing Tunable Miniaturization Factors", IEEE Transactions on Microwave Theory and Techniques, vol. 54, no. 1, pp. 135-146, January 2006.

[8] David Pozar, "Radiation and Scattering from a Microstrip Patch on a Uniaxial Substrate", *IEEE Transactions on Antennas and Propagation*, vol. AP-35, no. 6, pp. 613-621, June 1987.

[9] Wei Ren, Xin Bao Wu, Zhang Yi, and Wei Gan Lin, "Properties of Wave Function in Homogeneous Anisotropic Media", *The American Physical Society: Physical Review E*, vol. 51, no. 1, pp. 671-679, January 1995.

[10] Jennifer Graham, "Arbitrarily Oriented Biaxlly Anisotropic Media: Wave Behvaior and Microstrip Antennas" (2012). *Electrical Engineering and Computer Science – Dissertations*. Paper 320.

[11] Fan-Yi Meng, Qun Wu, and Le-Wei Li, "Transmission Characteristics of Wave Modes in a Rectangular Waveguide filled with Anisotropic Metamaterial", *Applied Physics A: Materials Science and Processing*, vol. 94, pp. 747-753, 2009.

[12] Fan-Yi Meng, Qun Wu, and Jia-Hui Fu, "Miniaturized Rectangular Cavity Resonator based on Anisotropic Metamaterials Bilayer", *Microwave and Optical Technology Letters*, vol. 50, no. 8, pp. 2016-2020, August 2008.

[13] MCLI Waveguide to Coaxial Adapters product page. http://mcli.com/products/waveguide-components/waveguide-to-coaxial-adapters.

[14] A.G. Williamson, "Analysis and Modeling of a Coaxial-line/Rectangular-waveguide Junction", *IEEE Proceedings (Microwaves, Optics, and Antennas)*, vol. 129, no. 5, October 1982.

[15] R. Collin, "A Simple Artificial Anisotropic Medium", IRE Transactions on Microwave Theory and Techniques, vol. 6, issue 4, pp. 206-209, April 1958.

[16] J. Volakis, C.C. Chen, and K. Fujimoto, Small Antennas: Miniaturization Techniques and Applications, McGraw Hill, 2010.

[17] H. Fang, M. Serhir, R. Balakrishnan, R. Guinvarc'h, K. Mouthan, "Low Profile Cavity-Backed Four-Arm Archimedean Spiral Antenna with 8:1 Bandwidth", 8th European Conference on Antennas and Propagation (EuCAP), 2014.

[18] Saqer Alja'afreh, Yi Huang, and Lei Xing, "A Compact, Wideband and Low Profile Planar Inverted-L Antenna", 8th European Conference on Antennas and Propagation (EuCAP), 2014.

[19] Ahmed Toaha Mobashsher and Amin Abbosh, "Three-dimensional folded antenna with ultra-wideband performance, directional radiation and compact size", *IET Microwaves, Antennas, and Propagation*, Vol. 8, Iss. 3, pp. 171-179, 2014.

[20] A. Chen, T. Jiang, Z. Chen and D. Su. "A Novel Low-Profile Wideband UHF Antenna", Progress in Electromagnetrics Research (PIER), Vol. 121, p. 75-88, 2011.

[21] N. Mohamed-Hicho, E. Davin, M. Cabedo-Fabres, and M. Bataller, "A Novel Low-Profile High-Gain UHF Antenna Using High-Impedance Surfaces", *IEEE Antennas and Wireless Propagation Letters*, Volume PP, Issue 99, 2013.

[22] Aita Thor, Anne Lepage, and Xavier Begaud, "Low Profile, Directive and Ultra Wideband Antenna on a High Impedance Surface", 3rd European Conference on Antennas and Propagation (EuCAP), 2009.

[23] M. Tanabe, Y. Oishi, and Y. Mastuda, "Radiation Characteristics of a Wide-Band Dipole Antenna ober an Electromagnetic Band-Gap (EBG) Reflector", IEEE-APS Topical Conference on Antennas and Propagation in Wireless Communications (APWC), 2014.

[24] David Staelin, Ann Morgenthaler, and Jin Au Kong, Electromagnetic Waves, Prentice Hall, Upper Saddle River, New Jersey, 1998.

[25] N. Maruvitz, Waveguide Handbook, 1st Ed., McGraw-Hill Book Company Inc., 1951.

[26] Antenna Substrate Materials Data Sheet, Spectrum Magnetics, LLC., http://www.spectrum-magnetics.com/files/SML-AntennaSubstrateMaterial.pdf.

[27] R. H. MacPhie and A. I. Zaghloul, "Radiation from a rectangular waveguide with infinite flange: Exact solution by correlation matrix," IEEE Trans. Antennas Propagation, vol. AP-28, pp. 497-503, July 1980.

[28] H. Baudrand, J. Tao, and J. Atechian, "Study of radiation properties of open-ended rectangular waveguides," IEEE Trans. Antennas Propagation, vol. 36, no. 8, pp. 1071-1077, Aug. 1988.

[29] H. Baudrand, J. Tao, and J. Atechian, "Study of radiation properties of open-ended rectangular waveguides," IEEE Trans. Antennas Propagation, vol. 36, no. 8, pp. 1071-1077, Aug. 1988.

[30] M. Born and E. Wolf, Principles of Optics: Electromagnetic Theory of Propagation, Interference and Diffraction of Light, 7th ed., Cambridge University Press, 1999.

[31] S. Mudiliar and J.K. Lee, "Dyadic Green's Functions for Layered Anisotropic Medium", *Electromagnetics*, vol. 3, pp. 111-130, 1983.

[32] D. Pozar, "Radiation and Scattering from a Microstrip Patch on a Uniaxial Substrate", IEEE Transactions on Antennas and Propagation. Vol. AP-35, no. 6, June 1987.

[33] H. Baudrand, J. Tao, and J. Atechian, "Study of radiation properties of open-ended rectangular waveguides," IEEE Trans. Antennas Propagation, vol. 36, no. 8, pp. 1071-1077, Aug. 1988.

[34] H. Serizawa and K. Hongo, "Radiation for a Flanged Rectangular Waveguide," IEEE Trans. Antennas Propagation, vol. 53, no.12, pp. 3953-3962, Dec. 2005.

[35] W. Coburn, T. Anthony, and A. Zahgloul, "Open-ended waveguide radiation characteristics – full-wave simulation versus analytical solutions," Antennas and Propagation Society International Symposium (APSURSI), 2010 IEEE.

[36] L. Felsen and N. Marcuvitz, Radiation and Scattering of Waves, Englewood Cliffs, NJ: Prentice Hall Inc., 1973.

[37] G. Strang, Introduction to Linear Algebra, 4th ed., Wellesley, MA: Cambridge Press, 2009.

[38] C. Balanis, Antenna Theory: Analysis and Design, 4th ed., Hoboken, NJ: Wiley and Sons Inc., 2005.

[39] A. Ishimaru, Electromagnetic Wave Propagation, Radiation, and Scattering, Upper Saddle River, NJ: Prentice Hall, 1991.

Appendices

Appendix A
Anisotropic Magnetic Metamaterials

This appendix illustrates actual measured data manufactured Metamaterials, Inc. located in Austin, TX. Metamaterials, Inc. calls this product P4 Metaferrite, and the U.S. Army Research Laboratory purchased this material in 2011 as part of their Battlefield Antenna program. The goal of this program was to produce an $\lambda_o/20$ antenna with positive realized gain from 200 MHz to 500 MHz. All measured data of the P4 Metaferrite is provided by Metamaterials, Inc. and we reproduce it here with their permission as one example of anisotropic magnetic metamaterial. We note the importance of the fact that current manifestations of this anisotropic medium are not limited to the values we describe in this appendix. We verify the values of the $\underline{\underline{\mu}}_r$ and $\underline{\underline{\varepsilon}}_r$ tensors in section A.3 using novel models developed by the author via a prototype test bed. Using this test bed, we compare simulation results to measured data taken at the U.S. Army Research Laboratory. These results verify the measured data provided by Metamaterials, Inc. We obtain all simulation results using models in CST Studio Suite 2014.

A.1 Advantages of Anisotropic Metamaterials

The research of this dissertation, especially chapter 5, shows that anisotropic media yields wider bandwidth and a higher realized gain in a lower profile cavity versus the same design utilizing isotropic media. This is due to the impedance match depending on the alignment of the dominant $\underline{\underline{\mu}}_r$ and $\underline{\underline{\varepsilon}}_r$ tensor elements with the direction of the transverse fields in the cavity. Specifically, in our LPA design we find aligning $\underline{\underline{\mu}}_r$ in the horizontal direction and $\underline{\underline{\varepsilon}}_r$ in the vertical direction produce the best results. Ideally the

ratio of the dominant axis of the $\underline{\underline{\mu_r}}$ tensor to that of the $\underline{\underline{\varepsilon_r}}$ should be large, on the order of 15 or higher. Our initial numerical investigation of the effects of the various tensor elements on antenna performance in appendix B shows that increasing the values of the other tensor elements tend to reduce bandwidth, and in some cases cause a severe degradation in the return loss at the antenna input.

Further advantages of anisotropic material are that Metamaterials Inc. claims that are significantly less dense (1.5 g/cm^3), and therefore much lighter, than traditional ferrites. For example the density of iron is 7.6 g/cm^3 and that of nickel is 8.9 g/cm^3. Since the permeability of the medium is responsible for the wide bandwidth of the low profile design this difference becomes paramount. Any airborne antenna applications require low profiles to reduce drag and light weight to reduce fuel consumption on lift off and to increase acceleration. While these anisotropic magnetic metamaterials are not as light as a dielectric, they are significantly lighter than a traditional ferrite as well as other manufactured isotropic magneto-dielectric metamaterials. For example, the isotropic magneto-dielectric medium produced by Spectrum Magnetics, LLC. that exhibits $12 \leq \mu_r \leq 15$ and $\tan\delta$ = 0.03 to 0.2 with $12 \leq \varepsilon_r \leq 15$ from 100 MHz to 500 MHz has a density of 4.2 g/cm^3 [16].

A.2 Description of the Manufacturing Process

Metaferrites Inc. fabricates the anisotropic metaferrite material using a roll-to-roll sputtering process. The process sputters magnetic filaments onto a substrate of dielectric material in a repeated pattern. This deposits a thin film of magnetic material onto the substrate, and creates a thin sheet of sputtered material. The manufacturer then etches a pattern into the magnetic film. This pattern is ultimately responsible for both the

magnitude and loss tangent of the $\underline{\underline{\mu}}_r$ tensor elements, as the more magnetic material that etches away leads to a lower magnitude and lower loss tangent and vice versa. The final step is to stack these thin sheets together and compress them into a solid block of effective anisotropic media.

While we address the manufacturing process in a very general overview above, much of this process is proprietary to Metamaterials Inc., and we cannot discuss it here. For instance, the electromagnetic properties of the dielectric substrate and the magnetic filaments are proprietary. Similarly, the thickness of the individual sputtered sheets and the way they are pressed and bonded into an effective block is proprietary. Most importantly, the way Metamaterials Inc. isolates and manipulates the values of individual tensor elements in the $\underline{\underline{\mu}}_r$ and $\underline{\underline{\varepsilon}}_r$ tensors is proprietary. However, we provide measured data of the effective media of the P4 Metaferrite in the following section.

A.3 Measured Parameters of Anisotropic P4 Metaferrite

This section illustrates actual measured data of the effective parameters provided for the P4 Metaferrite purchased by the U.S. Army Research Laboratory from Metamaterials Inc. The measurement process that produces this data is proprietary to Metamaterials Inc. We show a picture of a block of the effective anisotropic medium in figure A.1. This is an anisotropic material with the following $\underline{\underline{\mu}}_r$ and $\underline{\underline{\varepsilon}}_r$ tensors

$$\underline{\underline{\varepsilon}}_r(f) = \begin{bmatrix} \varepsilon_x(f) & 0 & 0 \\ 0 & \varepsilon_y(f) & 0 \\ 0 & 0 & \varepsilon_z(f) \end{bmatrix}, \tag{A.1a}$$

$$\underline{\underline{\mu_r}}(f) = \begin{bmatrix} \mu_x(f) & 0 & 0 \\ 0 & \mu_y(f) & 0 \\ 0 & 0 & \mu_z(f) \end{bmatrix}, \tag{A.1b}$$

where f is frequency. The inclusion of the f in the definition of equations A.1a and A.1b indicates that both the magnitudes and loss tangents of the tensor elements are frequency dependent. Much more so than we would expect from a standard dielectric medium.

Figure A.1: Tile of P4 Metaferrite manufactured by Metamaterials Inc.

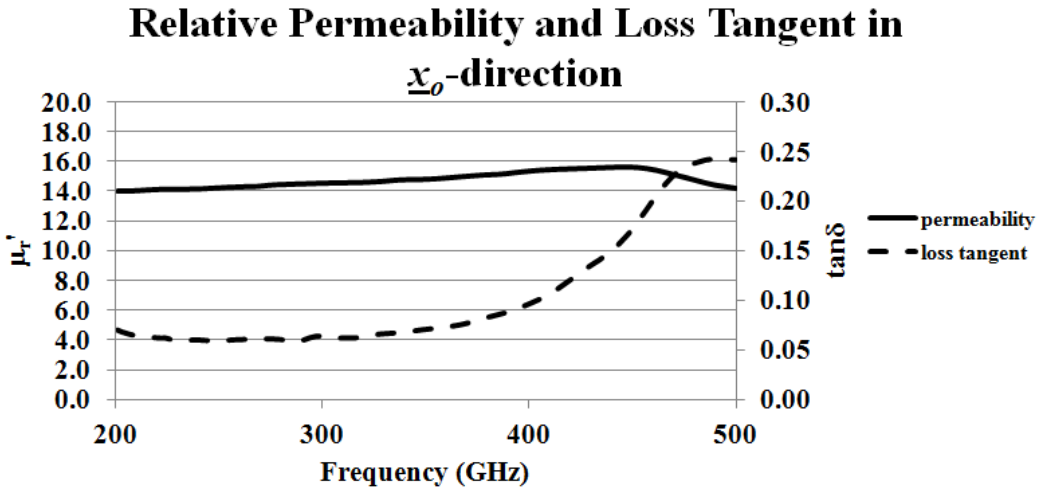

Figure A.2: Relative permeability and loss tangent of P4 Metaferrite in the $\underline{x}_o$-direction.

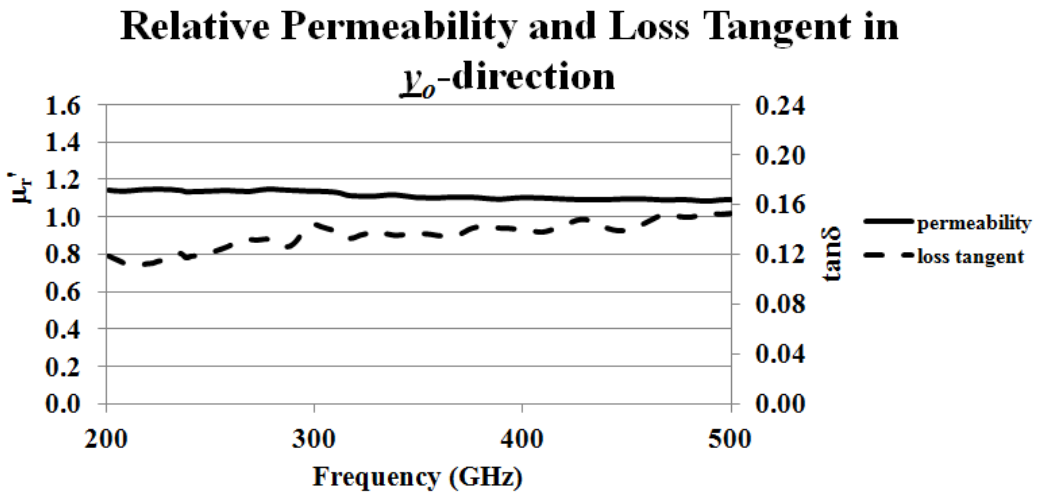

Figure A.3: Relative permeability and loss tangent of P4 Metaferrite in the $\underline{y_o}$-direction.

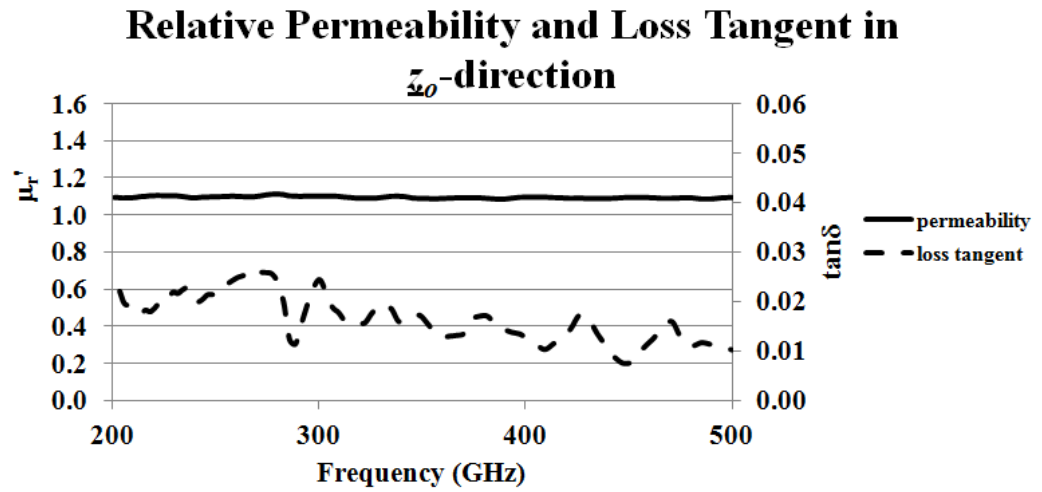

Figure A.4: Relative permeability and loss tangent of P4 Metaferrite in the $\underline{z_o}$-direction.

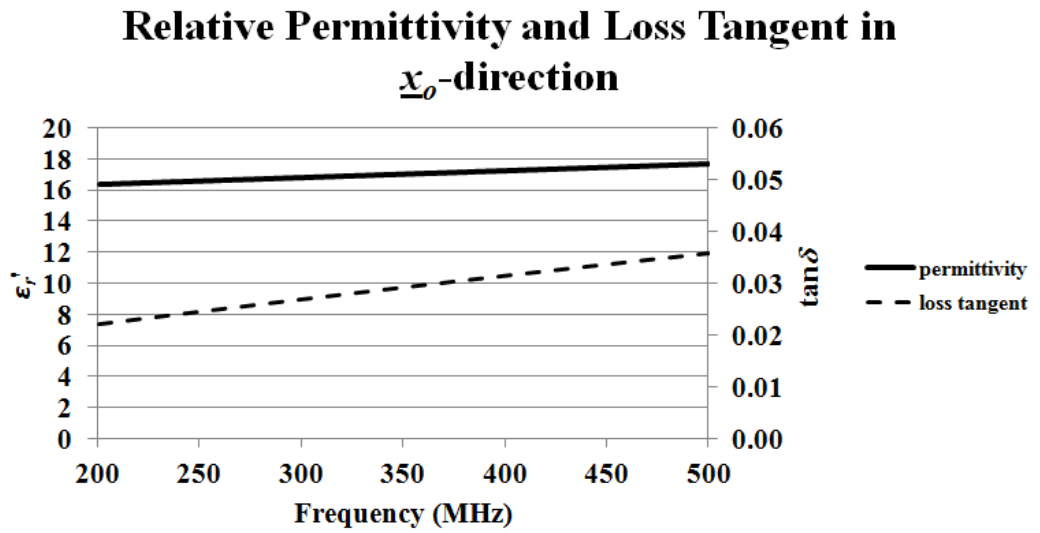

Figure A.5: Relative permittivity and loss tangent of P4 Metaferrite in the $\underline{x}_o$-direction.

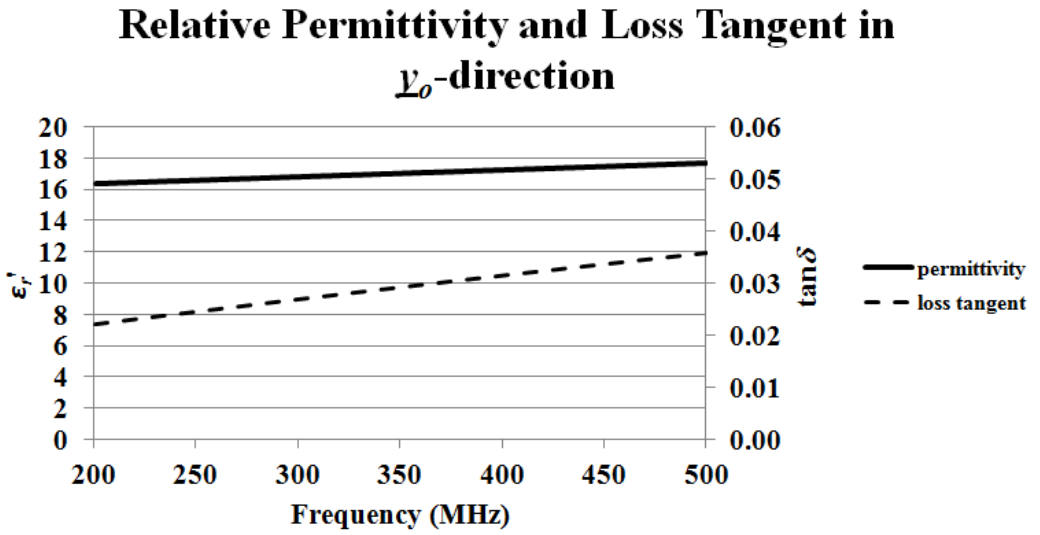

Figure A.6: Relative permittivity and loss tangent of P4 Metaferrite in the $\underline{y}_o$-direction.

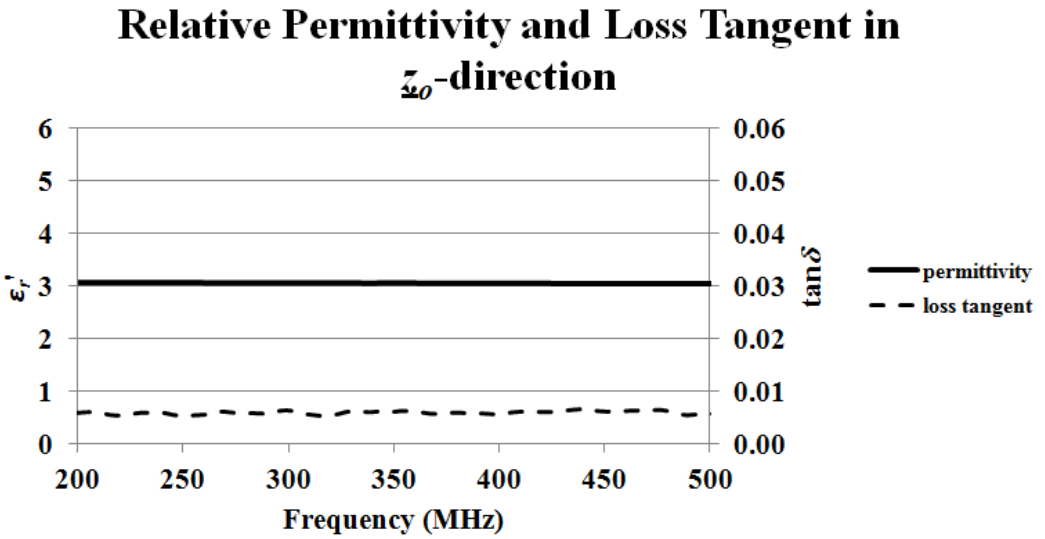

Figure A.7: Relative permittivity and loss tangent of P4 Metaferrite in the $\underline{z}_o$-direction.

Figure A.2 through figure A.4 shows the magnitude and loss tangent of the $\underline{\mu}_r$ tensor elements. We can see from figure A.3 that $\underline{x}_o$ is the dominant direction. We see that the value of μ_x' varies between 14 and 16 from 200 MHz to 500 MHz, while the loss tangent varies from .05 to .25 over the same frequency range. We should note that ARL purchased this material in 2010, and that the drastic increase in loss tangent from 400 MHz to 500 MHz is the result of an old manufacturing process. Metamaterials Inc. claims that this steep fluctuation in loss tangent is not present in the newer manufacturing processes. The magnitude of μ_x' and μ_y' in the $\underline{y}_o$ an $\underline{z}_o$ directions is approximately unity while the loss tangent in the $\underline{y}_o$-direction varies between tanδ = 0.12 and tanδ = 0.16, and the loss tangent in the $\underline{z}_o$-direction is approximately tanδ = 0.02.

Figure A.5 through figure A.7 show the magnitude and loss tangent of the $\underline{\varepsilon}_r$ tensor elements. We can see from figure A.5 and figure A.6 that the $\underline{x}_o$- and $\underline{y}_o$-directions are the same. However, this is due to the fact the ARL wanted these values to be the same, and is not inherent to some property of the manufacturing process. We see that the

value of ε_x' and ε_y' varies between 16 and 18 from 200 MHz to 500 MHz, while the loss tangent varies from .02 to .04 over the same frequency range. The magnitude of ε_z' in the $\underline{\hat{z}}_o$-direction is approximately 3 while the loss tangent is approximately 0.005. Metamaterials Inc. claims they can tailor the permittivity in the $\underline{\hat{x}}_o$- and $\underline{\hat{y}}_o$-directions from 3 to 1000 while maintaining these low loss tangents. The values of ε_z' and μ_z' are fixed.

A.4 Electromagnetic Models of P4 Metaferrite

As part of our research efforts, the author developed an electromagnetic model of the P4 Metaferrite provided by Metamaterials Inc. This model is novel as the manufacturer does not provide a detailed model of their anisotropic material. This section details the geometrical model developed in CST Studio Suite 2014 to simulate the macroscopic properties of the P4 Metaferrite tiles. We also illustrate the accuracy of this model by building and measuring a rudimentary antenna test bed. The antenna simulations incorporating our model of the anisotropic P4 Metaferrite tiles show good agreement of the measurement data for the same antenna test bed.

Figure A.2 shows a picture of a single tile of the material. The dimensions of the each tile are 76.2 mm x 76.2 mm x 10 mm in the $\underline{\hat{x}}_o$-, $\underline{\hat{y}}_o$-, and $\underline{\hat{z}}_o$-directions respectively. The entire tile does not have the $\underline{\underline{\varepsilon}}_r$ and $\underline{\underline{\mu}}_r$ values described in section A.3. In figure A.2, we see a 4x4 grid-like pattern of 16 white patches. These 16 patches extend the full depth (10 mm) of the block in the normal direction, and each individual patch consists of the P4 Metaferrite we describe in sections A.1 through A.3. In between these squares are dielectric spacers whose properties also have an effect on the effective $\underline{\underline{\varepsilon}}_r$ and $\underline{\underline{\mu}}_r$ of the tile as a whole.

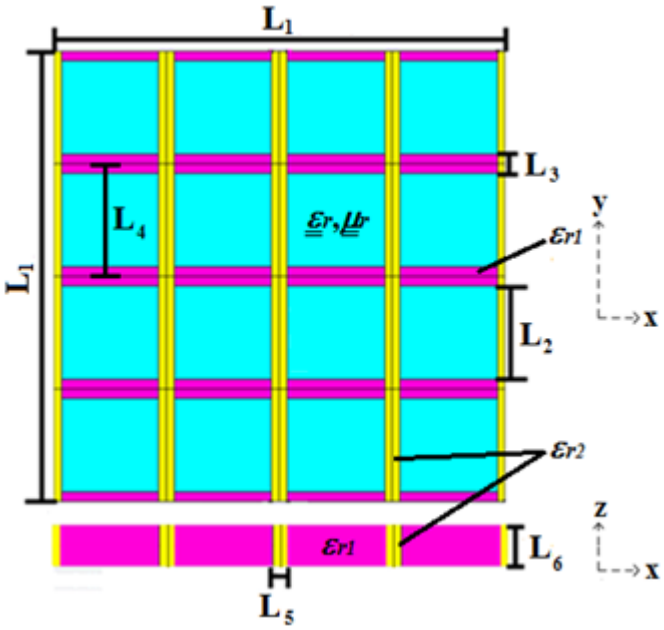

Figure A.8: Electromagnetic model of the P4 Metaferrite tile.

Figure A.8 shows an electromagnetic model of a single block of the P4 Metaferrite with dimensions L_1 x L_1 x L_6. The blue material represents the P4 Metaferrite and has dimensions of L_2 x L_2 x L_6. We define these sections of P4 Metaferrite with the properties we describe in section A.3. The purple material is a dielectric with dimensions L_2 x (L_3/2) x L_6 and a relative permittivity of ε_{r1}. The yellow material is a dielectric spacer with dimensions (L_5/2) x L_4 x L_6 and a relative permittivity of ε_{r2}, where $L_4 = L_2 + L_3$ and $\varepsilon_{r1} \neq \varepsilon_{r2}$. We note that the outer tile dimensions have no effect on the effective parameters of the P4 Metaferrite itself. The tiles from figure A.2 are cut to 76.2 mm^2 x 10 mm because those were the block sizes ordered by ARL. Any tile size and/or shape could be fabricated. However, the specific dimensions of the P4 Metaferrite blocks within the tile as well as the dimensions and dielectric properties of the dielectric spacers do affect the performance of the tile. Therefore, we do not give these dimensions as Metamaterials Inc. considers this information proprietary.

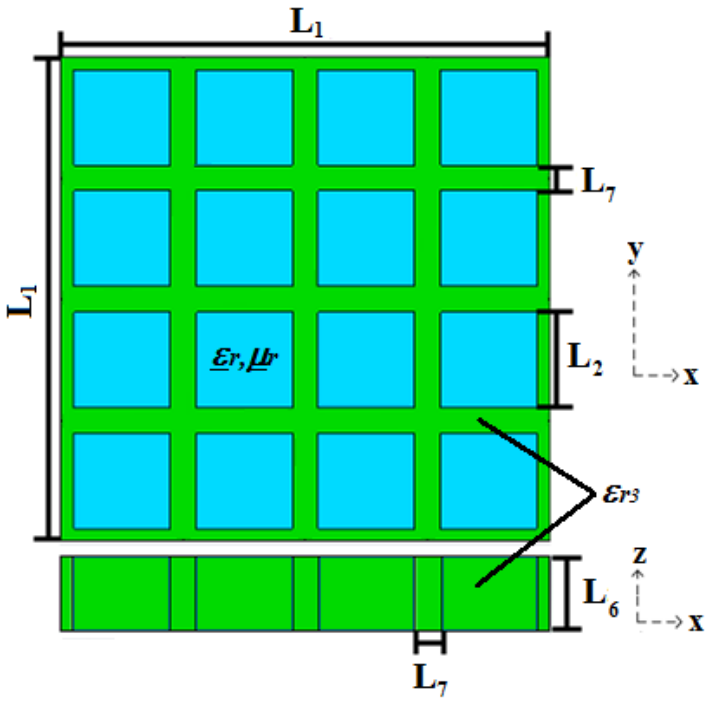

Figure A.9: Simplified P4 Metaferrite block model as developed by ARL.

We show the geometric model we use in the antenna test bed simulations in figure A.9. We make some simplifications to the model in figure A.8. We define the blue P4 Metaferrite squares with the same dimensions as in figure A.8. However, we average the dimensions and permittivity of the dielectric spacers such that $L_7 = (L_3 + L_5) / 2$ and $\varepsilon_{r3} = (\varepsilon_{r1} + \varepsilon_{r2}) / 2$. This approach significantly reduces the number of boundary conditions in the model which reduces simulation time. The agreement between simulation and measurement in section A.4.1 shows that these are valid simplifications that have minimal effect on the overall simulation results.

A.4.1 *Model Verification*

This section details the performance of an antenna test bed we use to verify the models we describe in section A.4. The test bed antenna is a center fed fat dipole backed by a rectangular cavity. Each arm of the dipole is fed 180° out of phase using two SMA

ports. We partially load the cavity with tiles of the P4 Metaferrite tiles we describe in sections A.1 through A.3.

We must make clear that we use this test bed to verify the accuracy of the P4 Metaferrite tile models only. We did not intend this antenna test bed to verify any aspect of the antenna designs from chapter 5 or even to perform well from 200 MHz to 500 MHz. In fact, the results of this section show this antenna to have a poor impedance match at the inputs. However, in terms of verifying the model, our only interest is in how the return loss and realized gain of the simulations compare to the experimental results, not whether the test bed represents a good antenna design. That being said, the comparison of simulation to experimental results for the antenna test bed in this section shows good agreement, and verifies the accuracy of the electromagnetic model of the P4 Metaferrite tile.

Figure A.10a shows the dimensions of the cavity and the radiating dipole element. Figure A.10b shows the cavity in profile and specifies the dimensions of the feed elements. The dipole is center fed 180° out of phase by two pins which are pressure fit to two SMA coaxial connectors. The dipole is a piece of FR4 with a lossy copper coating and the cavity walls are also lossy copper; however, we define the copper elements as a PEC in our simulation as this simplifies the model and reduces simulation time and memory requirements.

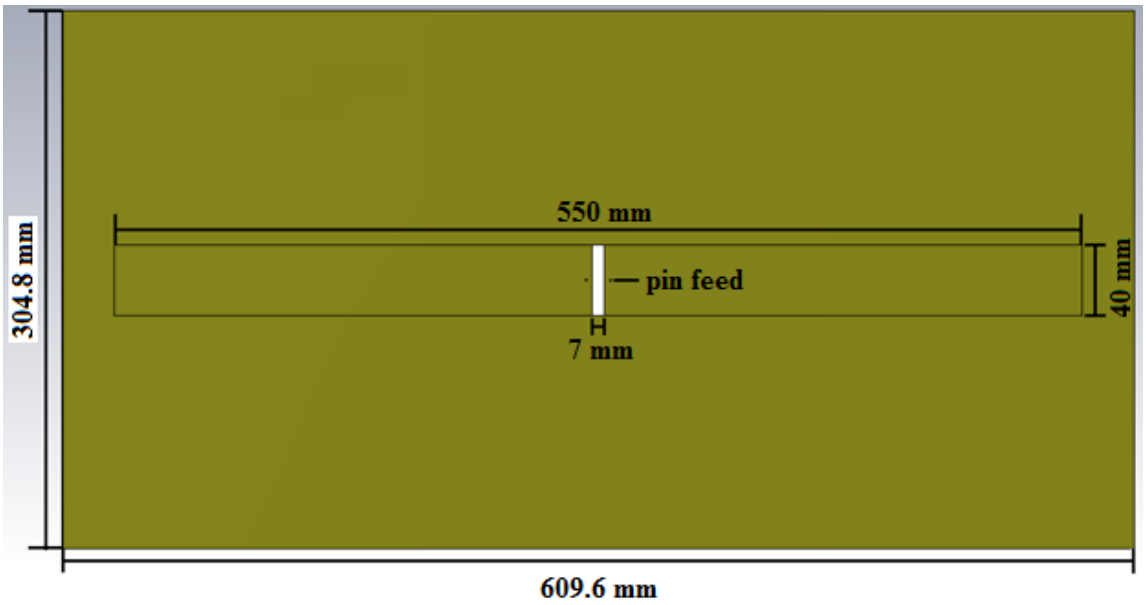

(a)

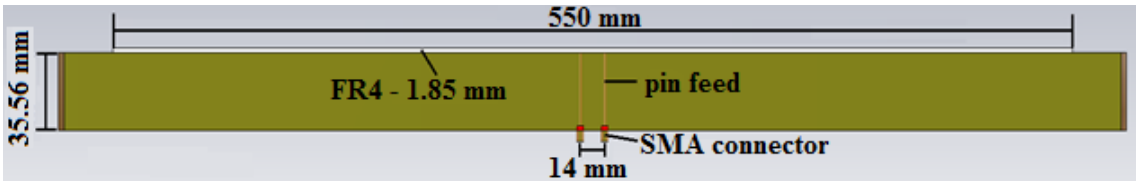

(b)

Figure A.10: Test bed cavity dimensions. (a) Transverse (*x*,*y*) plane. (b) Normal (*x*,z) plane.

The outer conductors of the two SMA connectors maintain a common ground with the walls of the cavity. We short the inner conductors of the SMA connectors to each arm of the dipole. The prototype pressure fits the feed pins into two Teflon standoffs (shown in red in figure A.10b), which maintains connectivity with the inner conductor of the SMA and allows for easy removal. The diameter of the inner conductor and outer conductor of the SMA connectors is 1.27 mm and 4.27 mm. We fill the connectors with lossy Teflon maintaining a 50 Ω impedance across the frequency range. Figure A.11a and figure A.11b show how we load the test bed cavity with P4 Metaferrite

tiles. Figure A.11a shows the placement of the P4 Metaferrite tiles in relation to the arms of the dipole cavity. The placement of the tiles is arbitrary as we were not interested in optimizing the performance of the antenna test bed. However, we purposely retain symmetry in the $\underline{x}_o$- and $\underline{y}_o$-directions to enable the use of symmetric boundary conditions in the simulation which cuts simulation time in half. Figure A.11b shows the antenna in profile and illustrates the placement of the tiles with respect to the backshort of the cavity. We see that we stack two layers of tiles on top of each other on both sides.

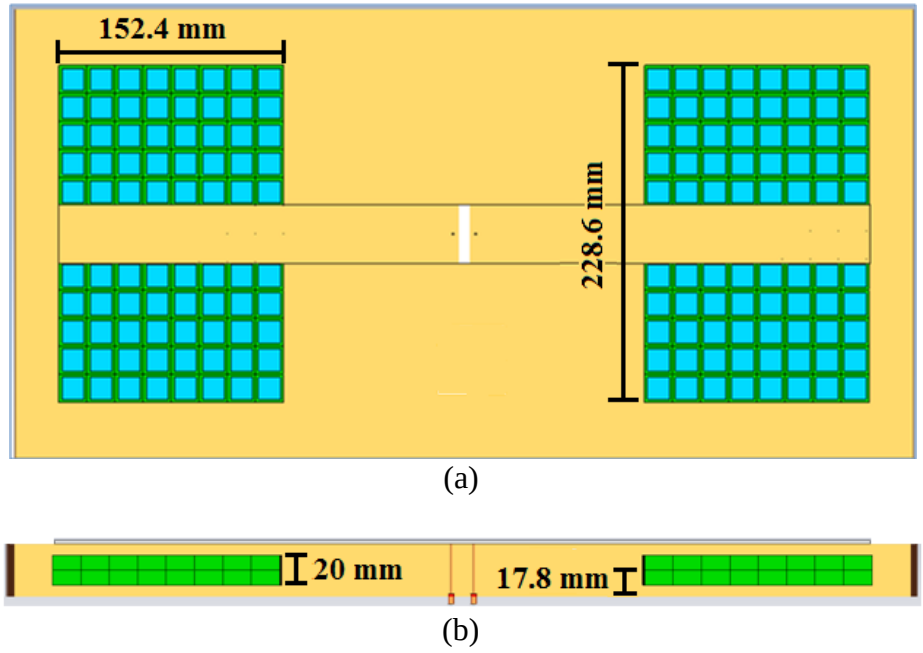

Figure A.11: Metaferrite placement in the cavity. (a) Transverse (x,y) plane. (b) Normal (x,z) plane.

Figure A.12 shows the comparison of measured S-parameters versus those generated by the simulation of the model using CST Studio Suite 2014. The blue and red lines represent the measurement results, while the green and purple lines represent simulation results. Both sets of plots show good agreement between simulation and measurement with a frequency shift of about 10 MHz, which represents about a 3.5%

deviation. This indicates that both the 3D model of the antenna test bed and the P4 Metaferrite model of section A.4.1 are accurate.

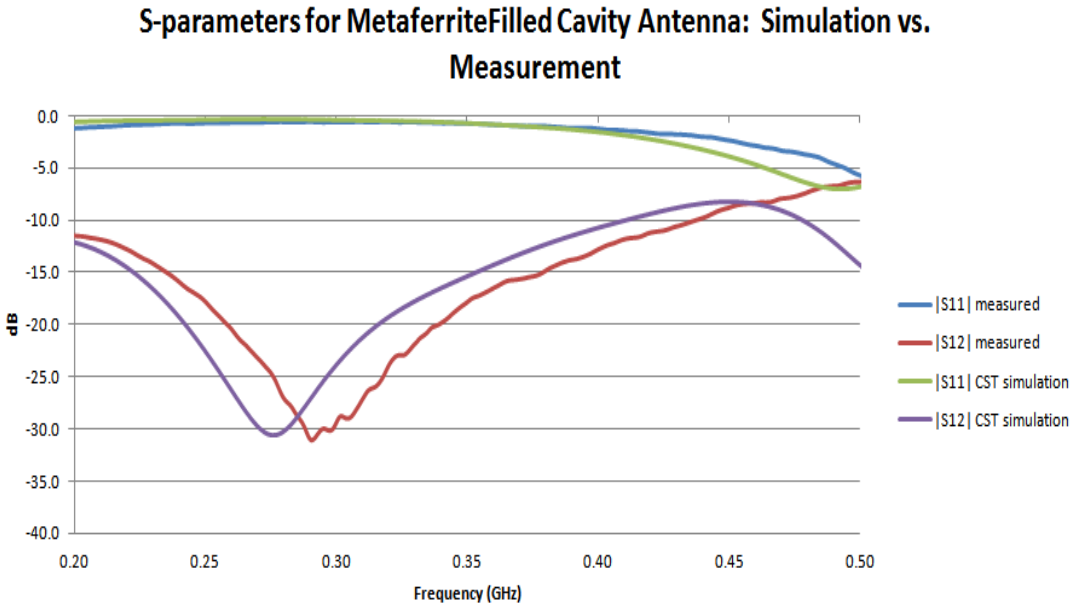

Figure A.12: Measured and simulated S-parameters of the loaded cavity test bed.

Figure A.13 shows the far-field realized gain of the antenna test bed measured in an anechoic chamber versus simulation results for the model shown in figure A.11a and figure A.11b. We took the measurements by feeding one SMA port as the input with the second port terminated in a 50 Ω load. Similarly, the simulation results excite one SMA port with a waveguide port, while terminating the second port with a 50 Ω load. This approach negates the need to use a commercial phase shifter to produce the 180° phase difference needed at the two input ports. Again, since we are only concerned with matching simulated results to measurements, we do not need to feed both ports as would be the case in a real application. This eliminates potential errors that could occur when trying to reproduce a precise model of a commercial device.

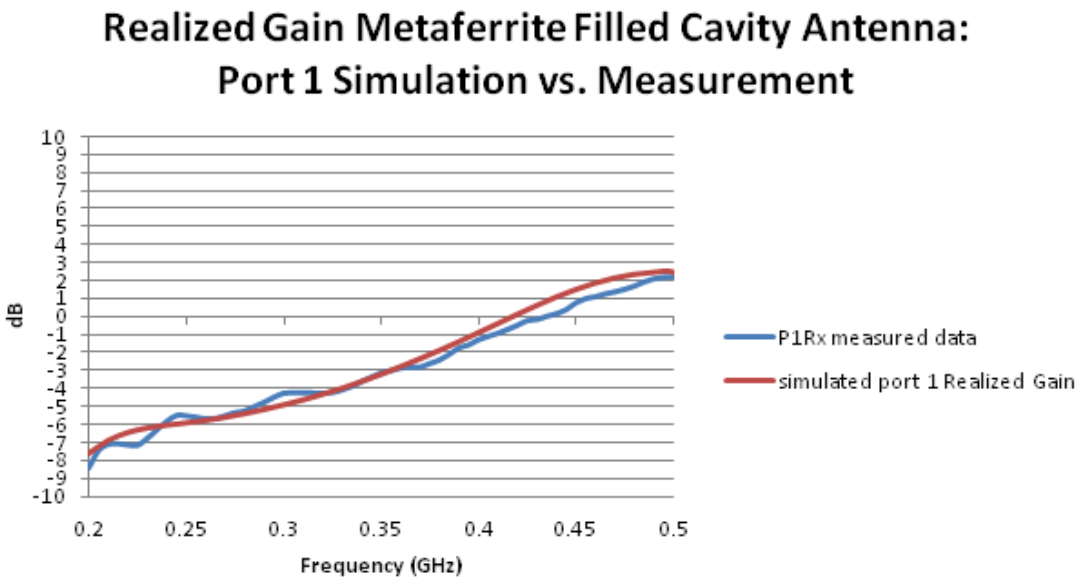

Figure A.13: Measured and simulated realized gain of the loaded cavity test bed.

Based on the agreement between the S-parameter and realized gain results, we can say our model of the P4 Metaferrite tiles accurately represents the effective behavior of the anisotropic metamaterial. This section details the investigation of the accuracy of an electromagnetic model for the P4 Metaferrite of figure A.1. We modeled and built an antenna test bed utilizing the P4 Metaferrite models of figure A.9. Simulation results based on this model compare very favorably with experimental data. This agreement verifies that the final model is an accurate representation of the properties of the P4 Metaferrite tiles, which we can now incorporate into future antenna designs.

Appendix B
Numerical Case Study of Linearly Tapered Low Profile Cavities

This appendix uses a numerical case study to analyze the properties of high index effective media used to load a cavity backed LPA. The LPA under investigation is a radiating rectangular cavity, with an open aperture, and a surrounding flange at the aperture. A tapered high index medium establishes local resonance condition with the conducting cavity walls. The LPA is fed by a variation on a traditional CWT feed similar to the one we use in the FLPA design of section 3.2.

We investigate the effects of various media including isotropic, anisotropic, dielectrics, ferrites, and magneto-dielectrics. Furthermore, this appendix demonstrates that using an anisotropic magnetic medium to load the cavity achieves positive realized gain from 200 MHz to 500 MHz, better than a 3:1 VSWR (return loss of -6 dB) from 300 MHz to 500 MHz and a cavity profile of $0.06\lambda_{max}$, where λ_{max} is the maximum free space wavelength in the VSWR frequency band.

B.1 Definition of Linearly Tapered Cavity Model

Initially we investigate an idea for a partially loaded and linearly tapered rectangular cavity to suppress the high order resonances. These high order resonances arise when fully loading the cavity with a high index medium as in section 3.3. These high order resonances are responsible for the volatile VSWR and realized gain curves of figure 3.19 and figure 3.20 respectively. We attempt to remove these high order resonances by linearly tapering our cavity inversely to our high index medium within the cavity.

We show this design in figure B.1 where a_0 is the horizontal dimension of the aperture, a_1 is half a wavelength inside the medium, b is the vertical dimension of the aperture, d is the cavity profile, L is the length of the probe, r is the width of the probe, and T is the thickness of the probe. We remove the top of the tapered medium because CST Studio Suite 2014 has issues resolving the infinitesimal tip in its mesh. Therefore, δ is the distance in the normal direction between the aperture and the top of the medium. T and δ are not given in normalized dimensions because they stay fixed with frequency.

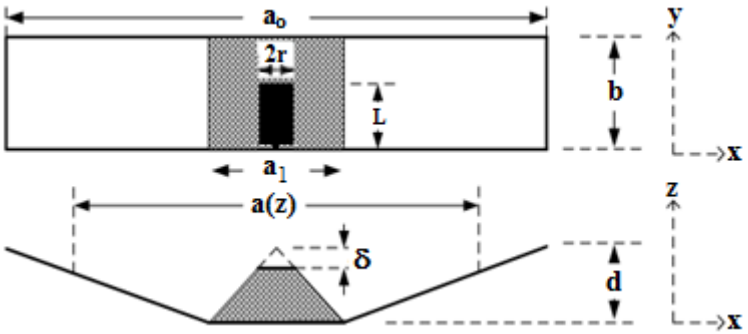

Figure B.1: Geometry of a linearly tapered cavity partially loaded with a high index medium.

Table B.1: Normalized dimensions for the tapered cavity model of figure B.1.

a_0	a_1	b	r	L	d	T	δ
$\lambda_o/2$	$a_o/(\mu_r\varepsilon_r)^{0.5}$	$\lambda_o/4.5$	$0.01\lambda_o$	$0.138\lambda_o$	$0.069\lambda_o$	2 mm	6.8 mm

We define the cavity profile d as $\lambda'_g/4$ where we define λ'_g, the effective guide wavelength, as

$$\lambda_g^{'} = \frac{\lambda_{o,cf}}{\sqrt{0.5\mu_r\varepsilon_r - \left(\frac{\lambda_{o,cf}}{(a_0 + a_1)}\right)^2}}. \tag{B.1}$$

This serves as an average of the guide wavelength of a fully loaded, non-tapered cavity taken at cavity depth $z = -d / 2$. The inverse relationship between the linear taper of the cavity walls and the width of the high index medium justifies the use of equation B.1.

B.2 Linearly Tapered Rectangular Cavity Partially Loaded with Isotropic Material

This section examines the cavity model we define in figure B.1 and table B.1 with a cavity partially loaded with isotropic high index materials exhibiting dielectric and/or magnetic properties. The hope is to see a significant reduction in cavity profile from the air-filled cavity of section. We equate the probe width, $2r$, with the width of the top of the high index medium at $z = -\delta$. We hope to provide a smooth impedance transition from the high index medium to free space using these probe dimensions.

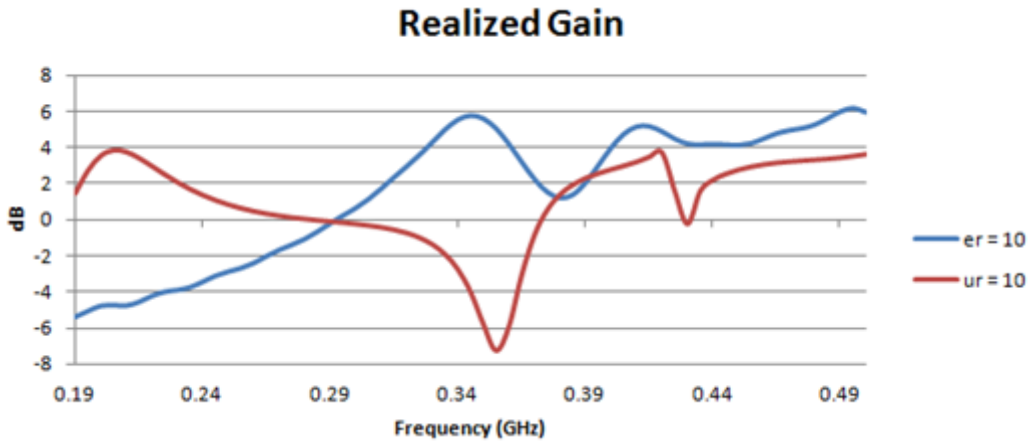

Figure B.2: Realized gain of the linearly tapered cavity loaded with dielectric and magnetic media.

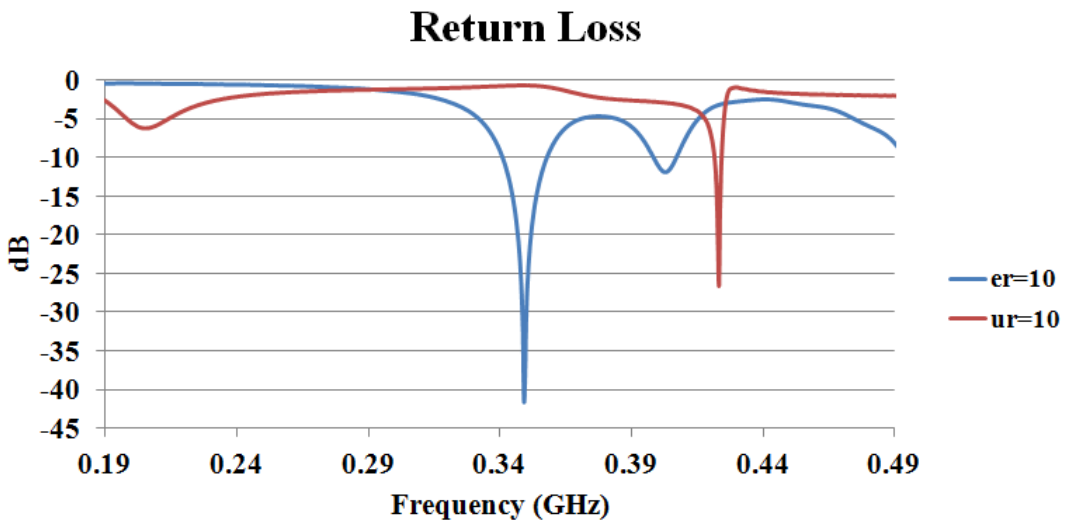

Figure B.3: Return loss of the linearly tapered cavity loaded with dielectric and magnetic media.

Figure B.2 and figure B.3 show the realized gain and return loss curves for isotropic media with values of (ε_r = 10, μ_r = 1) and (ε_r = 1, μ_r = 10) respectively. We calculate these results for λ_o = 1.56m (192 MHz). We achieve a cavity profile of d = 0.07λ_o compared to d = 0.14λ_o for the air filled cavity of section 3.2. This represents a 50.0% reduction in cavity profile.

For the dielectric material, from 290 MHz to 500 MHz there is a positive realized gain even though the return loss is not particularly good. This stems from the fact that there is a large aperture of λ_o^2 / 9 which becomes larger in terms of wavelength as frequency increases. At 350 MHz, where $d \approx \lambda'_g$ / 4, there is a narrowband match of better than -40 dB corresponding to the peak realized gain of about 5.8 dB. We expect this behavior since the best performance for a traditional CWT occurs for the air-filled cavity with a backshort approximately λ'_g / 4 from the probe.

For the magnetic material, the realized gain starts out positive from 200 MHz and crosses 0 dB at the same point that the realized gain for the dielectric material becomes positive at 290 MHz. The realized gain becomes positive again at about 275 MHz. While both curves have a dip at 420 MHz, the dip of the magnetic material is much more pronounced, and it also finishes much lower at the end of the frequency band. The return of the magnetic material shows extremely poor input match over much of the band from 200 MHz to 500 MHz. Since the dielectric material and magnetic material seem to cover different parts of the spectrum in terms of realized gain, it will be interesting to see how a magneto-dielectric material responds.

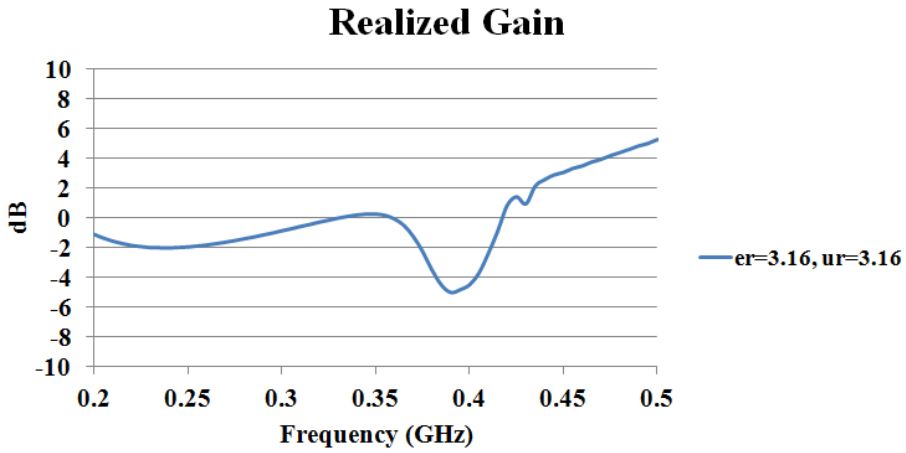

Figure B.4: Realized gain of the linearly tapered cavity loaded with a magneto-dielectric medium.

Figure B.4 and figure B.5 show the realized gain and return loss curves for an isotropic magneto-dielectric medium with values of $\varepsilon_r = \sqrt{10}$ and $\mu_r = \sqrt{10}$ respectively. We chose these values so the cavity dimensions match those in table B.1. Figure B.4 shows a realized gain pattern that has negative realized gain over much of the band from 200 MHz to 420 MHz. This seems to indicate that using a magneto-dielectric medium is

not as effective as a purely magnetic or dielectric isotropic medium. Decreasing the values of ε_r and μ_r until they approached unity would in fact trend the curves in figure B.4 and figure B.5 towards those of the air-filled rectangular cavity, but that also increases the total cavity profile.

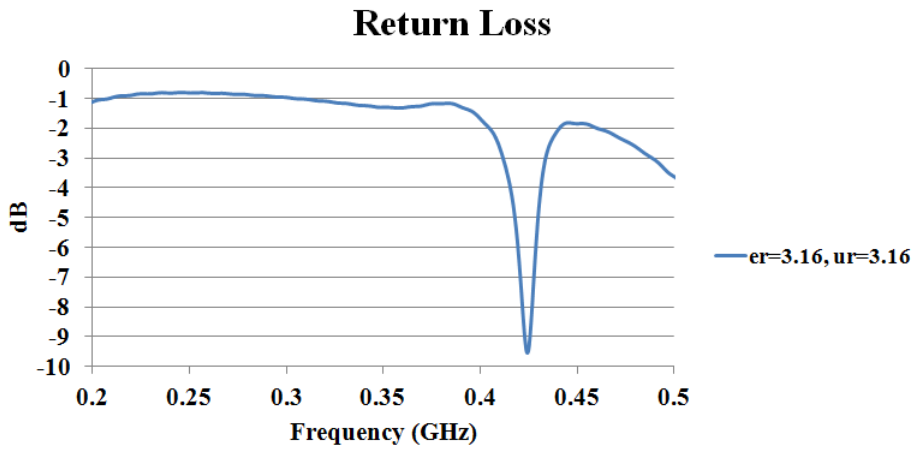

Figure B.5: Return loss of the linearly tapered cavity loaded with a magneto-dielectric medium.

This section demonstrates the ability to reduce the antenna profile by 50.0% with a partial loading of the air-filled cavity in section 3.2. Both the cases for dielectric and magnetic media show positive realized gain performance over parts of the frequency band.

B.3 Linearly Tapered Rectangular Cavity Partially Loaded with Anisotropic Material

This section analyzes the effects that diagonally anisotropic media have on the performance of the LPA model of figure B.1 with dimensions in table B.1. We define the anisotropy of the effective medium as

$$\underline{\varepsilon}_r = \begin{bmatrix} \varepsilon_x & 0 & 0 \\ 0 & \varepsilon_y & 0 \\ 0 & 0 & \varepsilon_z \end{bmatrix}, \tag{B.2a}$$

$$\underline{\mu}_r = \begin{bmatrix} \mu_x & 0 & 0 \\ 0 & \mu_y & 0 \\ 0 & 0 & \mu_z \end{bmatrix}. \tag{B.2b}$$

By isolating individual components of the permittivity and permeability tensors, we will identify behavior that improves the return loss and realized gain curves over those utilizing isotropic materials.

Initially, we examine how anisotropy in a single tensor element of equations B.2a and B.2b affects the behavior of the LPA. All other tensor elements are set to unity in each case. We refer to the axis of analysis as the dominant axis. We use the same form of equation B.1 where ε_r and μ_r will be replaced with the tensor values of the dominant axis.

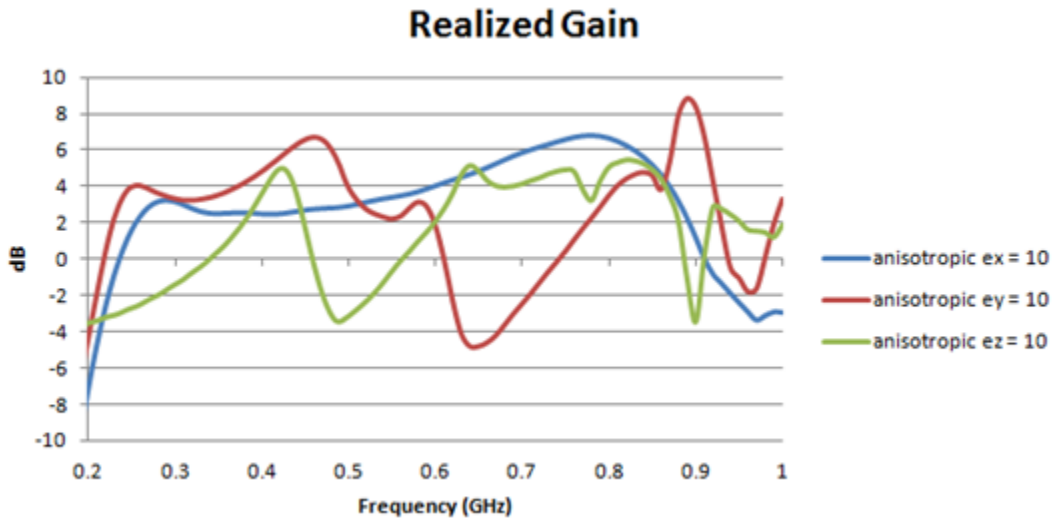

Figure B.6: Realized gain of the linearly tapered cavity loaded with anisotropic dielectric media.

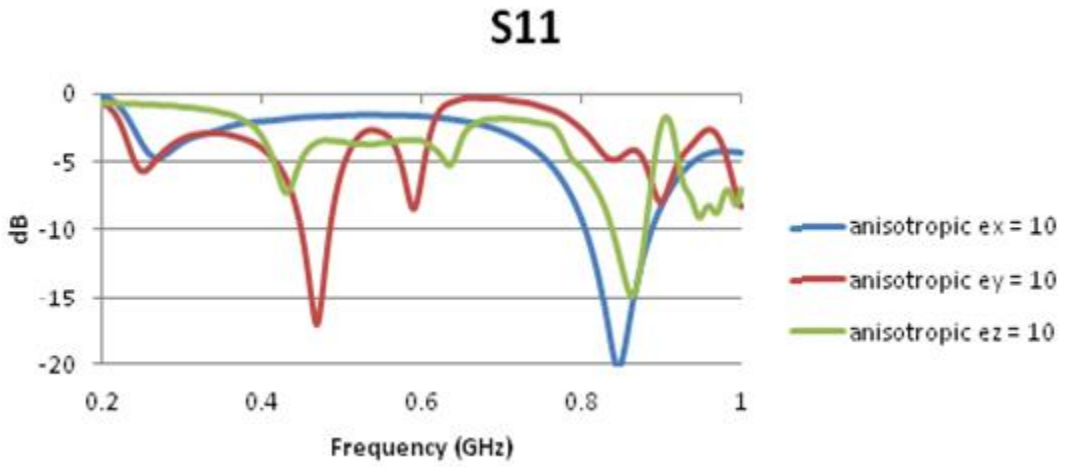

Figure B.7: Return loss of the linearly tapered cavity loaded with anisotropic dielectric media.

Figure B.6 and figure B.7 show the realized gain and return loss for a tapered cavity with λ_o = 1.56 m (192 MHz). We load the cavity with diagonally anisotropic media exhibiting ε_x = 10, ε_y = 10 or ε_z = 10 respectively. The blue curve represents the ε_x = 10 case, and clearly shows the best wideband performance in terms of positive realized gain from 240 MHz through 920 MHz. In this case, we align the dominant axis of the $\underline{\underline{\boldsymbol{\varepsilon}}}_r$ tensor in the same direction as the magnetic field at the aperture. The red curve shows the realized gain for the ε_y = 10 case as positive from 215 MHz through 605 MHz. In this instance, we align the dominant axis of the $\underline{\underline{\boldsymbol{\varepsilon}}}_r$ tensor in the same direction as the electric field at the aperture. The green curve represents the ε_z = 10 case and shows a positive realized gain from about 340 MHz through 460 MHz. While it goes positive again from about 575 MHz through 895 MHz, this is the narrowest band of positive realized gain seen in the frequency of interest and doesn't warrant further investigation. Comparing

the red and blue curves shows the LPA performs better at a lower frequency when aligning the $\underline{\varepsilon}_r$ tensor with the electric field in the cavity.

Figure B.7 shows that these positive realized gains do not necessarily mean there is a good input impedance match. Even for a return loss of -2 dB we still see a positive realized gain. A poor impedance match means much of the input power reflects from the antenna at the input resulting in an inefficient antenna that wastes the bulk of the power supplied to it. Clearly the impedance match at the input to the coaxial line feed needs improvement to achieve a useable wideband VSWR of 3 or better.

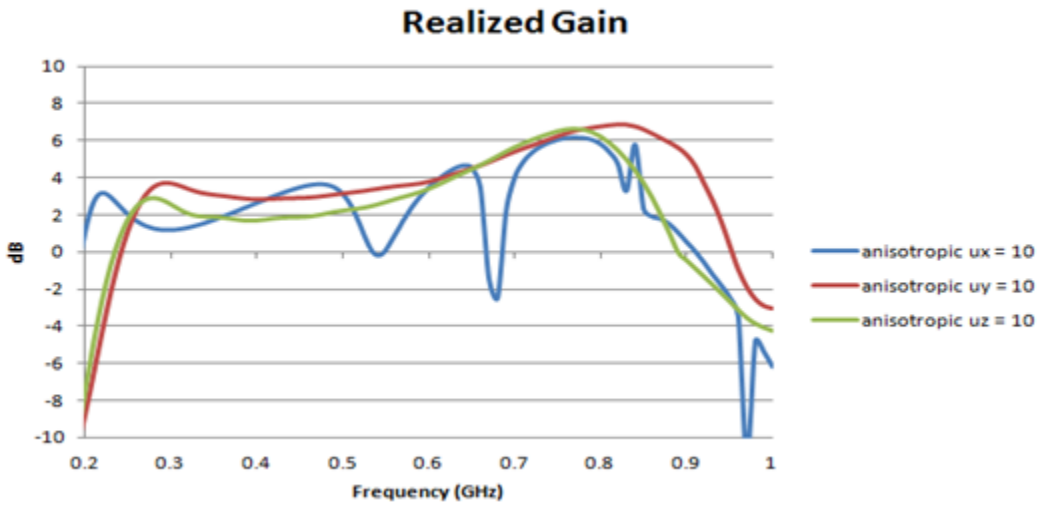

Figure B.8: Realized gain of the linearly tapered cavity loaded with anisotropic magnetic media.

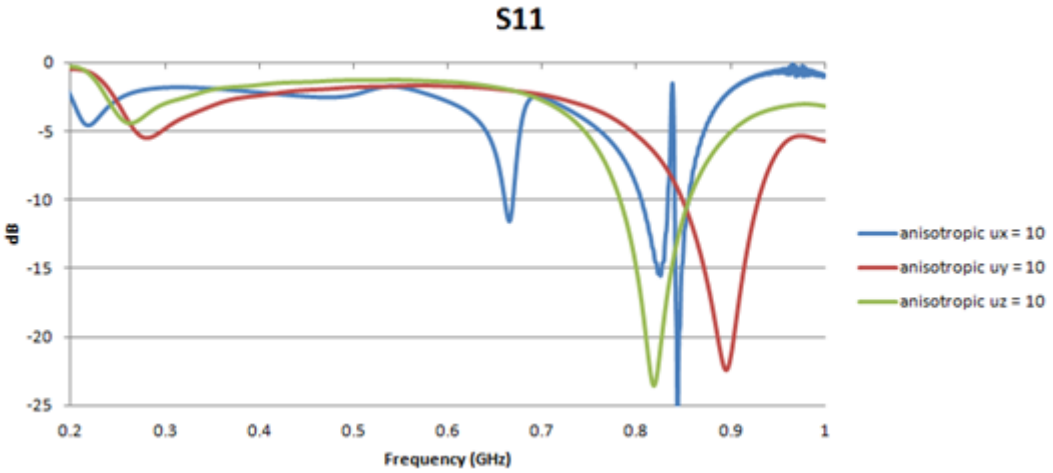

Figure B.9: Return loss of the linearly tapered cavity loaded with anisotropic magnetic media.

Figure B.8 and figure B.9 show the realized gain and return loss for a tapered cavity with λ_o = 1.33 m (225 MHz). We load the cavity an anisotropic medium exhibiting μ_x = 10, μ_y = 10 or μ_z = 10 respectively. The blue curve represents the μ_x = 10 case where the dominant axis of the $\underline{\underline{\mu_r}}$ tensor aligns with the direction of the magnetic field at the aperture. This case shows positive realized gain from 200 MHz through 540 MHz. The red curve represents the μ_y = 10 case where the dominant axis of the $\underline{\underline{\mu_r}}$ tensor aligns in the direction of the electric at the aperture. This case shows almost identical performance to the ε_x = 10 case with positive realized gain from 240 MHz through 920 MHz. The green curve represents the μ_z = 10 case and shows similar behavior to the μ_y = 10 case with a positive realized gain from about 240 MHz through 895 MHz. However, the μ_z = 10 has a lower realized gain than the μ_y = 10 case across the whole frequency range. Again figure B.9b shows a flat return loss, but the impedance match at the coaxial input needs improvement across the entire band of interest in all three cases.

This section demonstrates an improvement in the realized gain of the tapered cavity partially loaded with anisotropic media versus with isotropic media. The $\mu_x = 10$ case exhibits a positive realized gain over the entire frequency band from 200 MHz to 500 MHz. While this result is encouraging, the return loss shows how poor the input impedance match of this design is. However, as a preliminary design the potential to produce positive realized gain for a low-profile cavity based on an altered CWT exists. The results in this section indicate that using anisotropic media is advantageous over isotropic media, especially when aligning the dominant axes of the $\underline{\underline{\mu}}_r$ and $\underline{\underline{\varepsilon}}_r$ tensors with the directions of the magnetic and electric field at the aperture respectively.

B.4 Further Reduction of Cavity Profile

Section B.3 shows that aligning the dominant axes of the $\underline{\underline{\mu}}_r$ and $\underline{\underline{\varepsilon}}_r$ tensors with the directions of the magnetic and electric field at the aperture is the best configuration to achieve a positive realized gain starting 200 MHz. We hypothesize that increasing the value of the dominant axes in these cases allows us to further reduce the total cavity profile while maintaining a positive realized gain. Table B.2 gives the antenna dimensions for the $\mu_x = 15$ case with a rectangular cavity profile of $d = 0.063\lambda_o$ based on equation A.1 with μ_x substituted for μ_r.

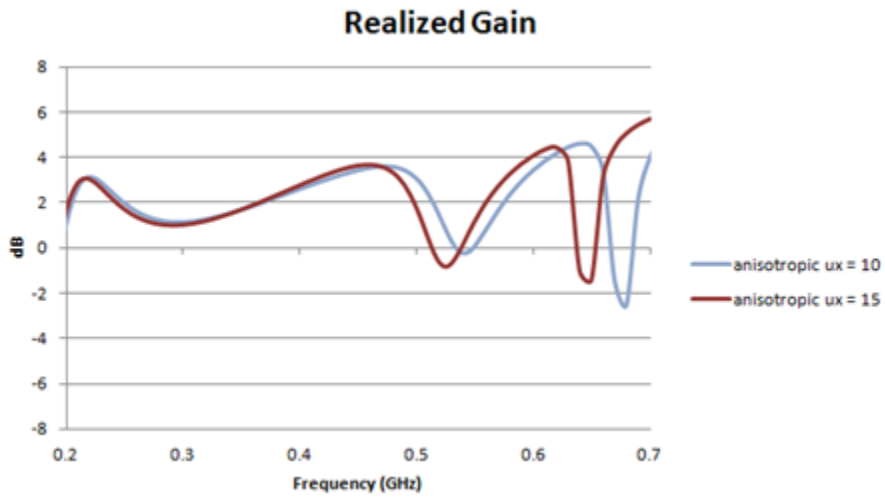

Figure B.10: Realized gain of the linearly tapered cavity loaded with anisotropic magnetic media with varying μ_x.

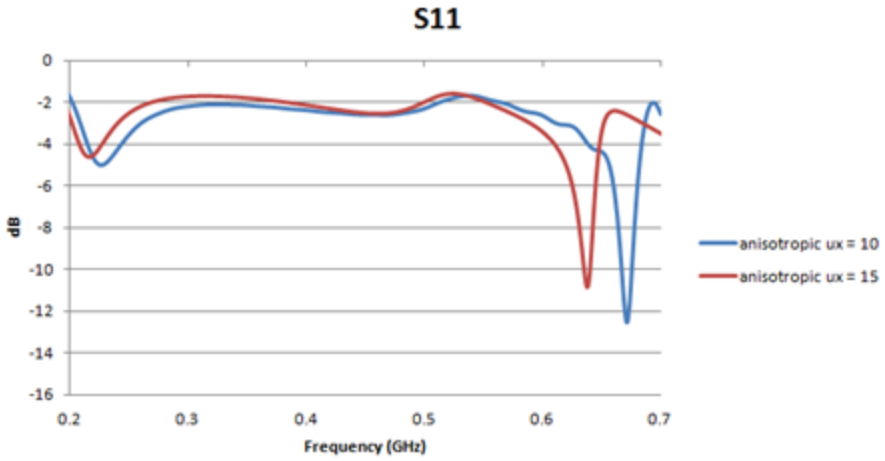

Figure B.11: Return loss of the linearly tapered cavity loaded with anisotropic magnetic media with varying μ_x.

Table B.2: Normalized dimensions for the linearly tapered cavity when $\mu_x = 15$.

a_0	a_1	b	r	L	d	T	δ
$\lambda_o/2$	$a_o/(\mu_r \varepsilon_r)^{0.5}$	$\lambda_o/4.5$	$0.01\lambda_0$	$0.138\lambda_o$	$0.063\lambda_o$	2 mm	6.8 mm

Figure B.10 and figure B.11 show the realized gain and return loss for an anisotropic medium with $\mu_x = 10$ and $\mu_x = 15$ respectively. We make both calculations for

λ_o = 1.33 m. The blue curve corresponds to the μ_x = 10 case, and the red curve corresponds to the μ_x = 15 case. There is very little difference in the realized gain or return loss except for a slight shift down in frequency when μ_x = 15. There is still a positive realized gain from 200 MHz to 500 MHz while reducing the profile of the cavity to $d = 0.06\lambda_o$ compared to $d = 0.07\lambda_o$ for the μ_x = 10 case. This represents a further 9% reduction in cavity profile.

These results demonstrate that increasing the horizontal axis of the $\underline{\underline{\mu}}_r$ tensor has the desired effect of further reduction in cavity profile while having very little effect on the antenna performance. However, we must keep in mind that we assume these media are lossless in this case study, whereas real world media may have non-negligible losses. Another idealization we make is the use of an infinite flange. While this is a widely used mechanism in theoretical models [27]-[29], a practical application requires a minimal flange. In the next section, we verify that reducing the size of the flange does not negatively impact the positive results seen thus far.

B.5 Reduction of Flange Size

Section B.4 shows how increasing the horizontal axis of the $\underline{\underline{\mu}}_r$ tensor in the direction of the magnetic field at the aperture further reduces the cavity profile of the LPA. Since this improvement does not significantly degrade the performance of the LPA, this section analyzes the effect of reducing the size of the flange around the aperture. The numerical case studies of sections B.2 through B.4 assume an infinite conducting flange surrounding the cavity aperture. We use this approximation for simulation purposes, and from a practical standpoint, approximating a flange of several wavelengths by a finite flange is valid. However, chapter 3 shows that based on

commercial designs, a flange of $1.43\lambda_o$ is ideal. However, at low UHF this flange size may also be prohibitively large. Therefore, it is important to see how much the reduction in flange size will affect the results seen thus far. The following results use the normalized dimensions in table B.2 and correspond to the model of figure B.1. We load the cavity of figure B.1 with an anisotropic medium defined by equation with $\mu_x = 15$ and all other tensor elements on the diagonal set to unity.

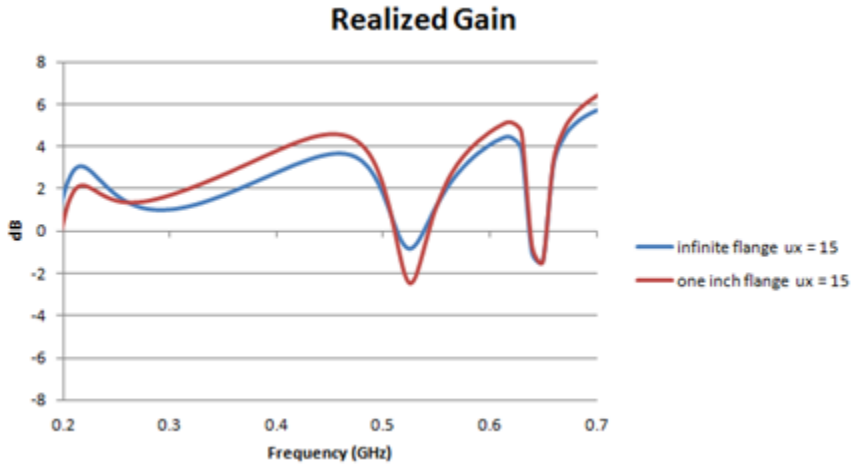

Figure B.12: Realized gain of the linearly tapered cavity loaded with anisotropic magnetic media with different flange sizes.

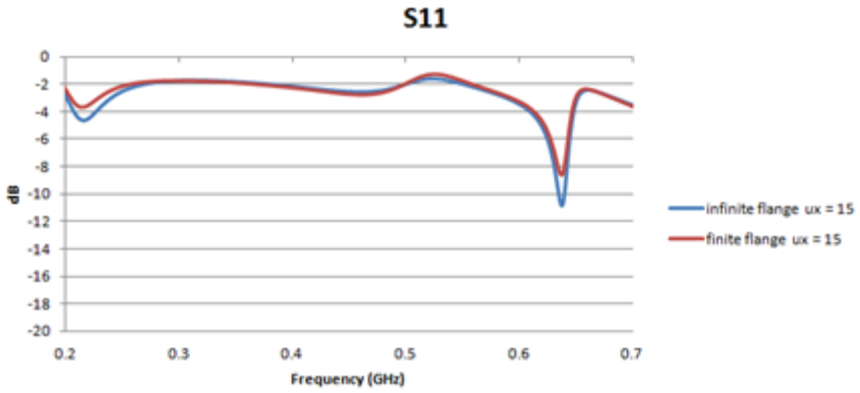

Figure B.13: Return loss of the linearly tapered cavity loaded with anisotropic magnetic media with different flange sizes.

Figure B.12 and figure B.13 compare the results for a finite flange of 1.0 inches surrounding the cavity aperture to those of the infinite flange of section B.4. The blue curve represents the infinite flange and the red curve represents the finite flange. The figures show approximately a ± 1.0 dB difference between the two realized gain curves and nearly identical return loss. This shows that even for a significant reduction in flange size, the design achieves a comparable result which is very important for real life applications. Now we will focus on how tuning the dimensions of the rectangular probe affect the return loss seen at the coaxial input to the altered CWT feed.

B.6 Effect of Probe Dimensions on the Return Loss

Currently, the LPA design results in a profile of $0.06\lambda_o$ with a positive realized gain from 200 MHz to 500 MHz. However, a poor return loss at the coaxial input keeps this design from achieving comparable results to the benchmark performance of the antenna in section 3.2. One potential reason for the impedance mismatch may stem from a reactance created within the cavity. The abrupt transition from high index metamaterial to free space near the aperture is probably the reason for this mismatch. One way to counteract this would be to increase the width of the rectangular probe used to stimulate the fields inside the cavity. Thus far all designs in the numerical case study use $r = 0.01\lambda_o$ to match the width of the medium at $z = -\delta$. This section explores the effect of changing r on the return loss of the LPA at the coaxial input.

Figure B.14 and figure B.15 show the realized gain and return loss for different r used to stimulate the fields inside the cavity. All other dimensions are the same as those listed in table B.2 with $\mu_x = 15$. Figure B.15 shows that as r increases there is better wideband performance up to $2r = 0.152\lambda_o$ (8.0 inches). When $2r = 0.191\lambda_o$ (10.0 inches),

degradation occurs in the return loss. The best case scenario in terms of the impedance match is for when $2r = 0.152\lambda_o$ providing a return loss of better than -10 dB from 375 MHz to 575 MHz (0.53 octaves) and better than -6 dB from 300 MHz to 575 MHz (0.92 octaves). This is a major improvement over a significant portion of the band.

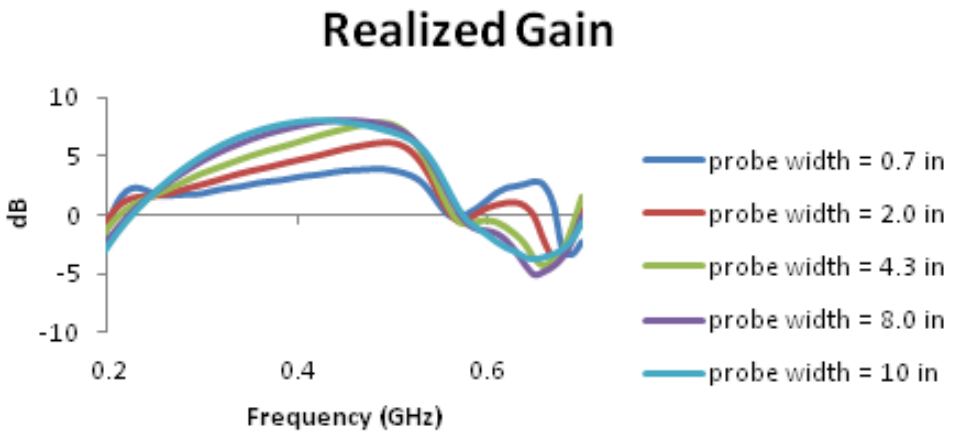

Figure B.14: Realized gain of the linearly tapered cavity loaded with anisotropic magnetic media with different probe widths.

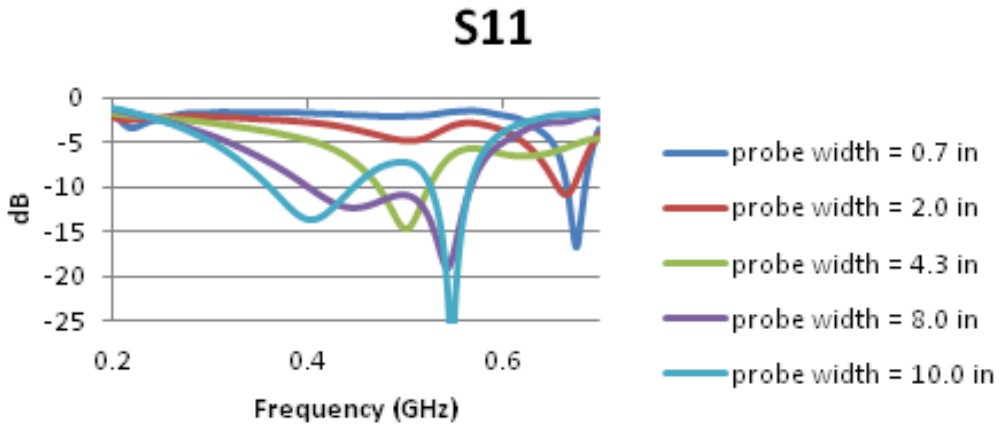

Figure B.15: Return loss of the linearly tapered cavity loaded with anisotropic magnetic media with different flange sizes.

Figure B.14 shows how the improved return loss affects the realized gain. There is up to a 4.0 dB improvement between the dark blue curve and purple curve representing the $2r = 0.01\lambda_o$ (0.7 inch) and $2r = 0.152\lambda_o$ cases respectively. A trade off in terms of realized gain has been made at the lower end of the frequency band to achieve this improved performance at the higher end. The realized gain bandwidth moves to 220 MHz to 580 MHz (1.64 octaves). This demonstrates how sensitive the antenna's impedance match is to the dimensions of the rectangular probe, and that by tuning the probe we can directly affect the impedance match seen at the coaxial input to the LPA.

Appendix C
Plane Wave Propagation in an Anisotropic Medium

The electromagnetic wave propagation in homogeneous anisotropic dielectric media has been well understood in optical media since the fifties. At optical frequencies, one has to rely on naturally occurring crystalline media with anisotropic properties. However, as early as 1958 Collin showed that at microwave frequencies, where the wavelength is much greater, it is possible to fabricate artificial dielectric media having anisotropic properties [14].

The recent development of low loss anisotropic magneto-dielectrics greatly expands the current antenna design space. Here we present a rigorous derivation of the wave equation and dispersion relationships for anisotropic magneto-dielectric media. All results agree with those presented by Meng, et. al [11], [12]. Furthermore, setting $\underline{\underline{\mu}}_r = \underline{\underline{I}}$, where $\underline{\underline{I}}$ is the identity matrix, yields results that agree with those presented by Pozar and Graham for anisotropic dielectric media [8], [10].

C.1 Anisotropic Wave Equation

In order to solve for the propagation constants we will need to formulate the dispersion relationship from the anisotropic wave equation. This allows us to solve for the propagation constant in the normal direction of the anisotropic medium. We start with the anisotropic, time harmonic form of Maxwell's source free equations for the electric and magnetic fields

$$\nabla x \underline{E} = j\omega\mu_o \underline{\underline{\mu}}_r \cdot \underline{H}, \tag{C.1a}$$

$$\nabla x \underline{H} = -j\omega\varepsilon_o \underline{\underline{\varepsilon}}_r \cdot \underline{E}, \tag{C.1b}$$

where ω is the frequency in radians, ε_o is the permittivity of free space, μ_o is the permeability of free space, $\underline{E} = \underline{x}_o E_x + \underline{y}_o E_y \pm E_z$ and $\underline{H} = \underline{x}_o H_x + \underline{y}_o H_y \pm H_z$. We define $\underline{\underline{\mu_r}}$ and $\underline{\underline{\varepsilon_r}}$ as

$$\underline{\underline{\varepsilon_r}} = \begin{bmatrix} \varepsilon_x & 0 & 0 \\ 0 & \varepsilon_y & 0 \\ 0 & 0 & \varepsilon_z \end{bmatrix}, \tag{C.2a}$$

$$\underline{\underline{\mu_r}} = \begin{bmatrix} \mu_x & 0 & 0 \\ 0 & \mu_y & 0 \\ 0 & 0 & \mu_z \end{bmatrix}. \tag{C.2a}$$

Now we define the curl operator as

$$\nabla \times \underline{\Phi} = \underline{x}_o \left(\frac{d\Phi_z}{dy} - \frac{d\Phi_y}{dz} \right) + \underline{y}_o \left(\frac{d\Phi_x}{dz} - \frac{d\Phi_z}{dx} \right) + \underline{z}_o \left(\frac{d\Phi_y}{dx} - \frac{d\Phi_x}{dy} \right). \tag{C.3}$$

Applying equations C.2a, C.2b and C.3 to equations C.1a and C.1b yields the following representations of C.1a and C.1b

$$\begin{aligned} &\underline{x}_o \left(\frac{dE_Z}{dy} - \frac{dE_Y}{dz} \right) + \underline{y}_o \left(\frac{dE_X}{dz} - \frac{dE_Z}{dx} \right) \\ &\quad + \underline{z}_o \left(\frac{dE_Y}{dx} - \frac{dE_X}{dy} \right) = -j\omega\mu_o \left(\mu_x H_X \underline{x}_o + \mu_y H_Y \underline{y}_o + \mu_z H_Z \underline{z}_o \right) \end{aligned}, \tag{C.4a}$$

$$\begin{aligned} &\underline{x}_o \left(\frac{dH_Z}{dy} - \frac{dH_Y}{dz} \right) + \underline{y}_o \left(\frac{dH_X}{dz} - \frac{dH_Z}{dx} \right) \\ &\quad + \underline{z}_o \left(\frac{dH_Y}{dx} - \frac{dH_X}{dy} \right) = j\omega\varepsilon_o \left(\varepsilon_x E_X \underline{x}_o + \varepsilon_y E_Y \underline{y}_o + \varepsilon_z E_Z \underline{z}_o \right) \end{aligned}. \tag{C.4b}$$

Using the radiation condition, we assume a solution of $\underline{E}(\underline{r}) = \underline{E}(x, y) e^{-jk_z z}$. Now we isolate the individual components of equation 0.4a by taking the dot product with $\underline{x}_o$, $\underline{y}_o$, and $\underline{z}_o$ respectively. This operation yields the following equations

$$\frac{dE_z}{dy} - jk_z E_y = -j\omega\mu_o\mu_x H_x, \tag{C.5a}$$

$$jk_z E_x - \frac{dE_z}{dx} = -j\omega\mu_o\mu_y H_y, \tag{C.5b}$$

$$\frac{dE_y}{dx} - \frac{dE_x}{dy} = -j\omega\mu_o\mu_z H_z. \tag{C.5c}$$

The same procedure assuming a solution of $\underline{H}(\underline{r}) = \underline{H}(x,y)e^{-jk_z z}$ for equation C.4b yields

$$\frac{dH_z}{dy} - jk_z H_y = j\omega\varepsilon_o\varepsilon_x E_x, \tag{C.6a}$$

$$jk_z H_x - \frac{dH_z}{dx} = j\omega\varepsilon_o\varepsilon_y E_y, \tag{C.6b}$$

$$\frac{dH_y}{dx} - \frac{dH_x}{dy} = j\omega\varepsilon_o\varepsilon_z E_z. \tag{C.6c}$$

Using equations C.5a through C.5c and C.6a through C.6c allows us to solve for the transverse field components of the electric and magnetic fields in terms of the derivatives of H_z and E_z

$$E_x = -\frac{j}{k_o^2\mu_y\varepsilon_x - k_z^2}\left(\omega\mu_o\mu_y\frac{dH_z}{dy} + k_z\frac{dE_z}{dx}\right), \tag{C.7a}$$

$$E_y = \frac{j}{k_o^2\mu_x\varepsilon_y - k_z^2}\left(\omega\mu_o\mu_x\frac{dH_z}{dx} - k_z\frac{dE_z}{dy}\right), \tag{C.7b}$$

$$H_x = \frac{j}{k_o^2\mu_x\varepsilon_y - k_z^2}\left(\omega\varepsilon_o\varepsilon_y\frac{dE_z}{dy} - k_z\frac{dH_z}{dx}\right), \tag{C.7c}$$

$$H_y = -\frac{j}{k_o^2 \mu_y \varepsilon_x - k_z^2}\left(\omega \varepsilon_o \varepsilon_x \frac{dE_z}{dx} + k_z \frac{dH_z}{dy}\right). \tag{C.7d}$$

Now that we have relationships for the transverse field components, we can solve equations C.1a and C.1b for $\underline{\boldsymbol{H}}$ and $\underline{\boldsymbol{E}}$ respectively

$$\underline{H} = -\frac{\underline{\mu}_r^{-1}}{j\omega\varepsilon_o} \cdot \left(\nabla x \underline{E}\right), \tag{C.8a}$$

$$\underline{E} = \frac{\underline{\varepsilon}_r^{-1}}{j\omega\varepsilon_o} \cdot \left(\nabla x \underline{H}\right) \cdot \tag{C.8b}$$

Taking the cross product of both sides and substituting equation C.1a for $\nabla x \underline{E}$ and C.1b for $\nabla x \underline{H}$ respectively yields

$$\nabla \times \underline{E} = \nabla \times \frac{\underline{\varepsilon}_r^{-1}}{j\omega\varepsilon_o} \cdot \left(\nabla x \underline{H}\right), \tag{C.9a}$$

$$\nabla \times \underline{H} = -\nabla \times \frac{\underline{\mu}_r^{-1}}{j\omega\mu_o} \cdot \left(\nabla x \underline{E}\right), \tag{C.9b}$$

$$\nabla x \underline{\varepsilon}_r^{-1} \cdot \left(\nabla x \underline{H}\right) = k_o^2 \underline{\mu}_r \cdot \underline{H}\,, \tag{C.10a}$$

$$\nabla x \underline{\mu}_r^{-1} \cdot \left(\nabla x \underline{E}\right) = -k_o^2 \underline{\varepsilon}_r \cdot \underline{E}\,. \tag{C.10b}$$

Equations C.10a and C.10b represent the vector wave equations in an anisotropic medium [12].

C.2 Dispersion equation for H_z

We expand the $\nabla x \underline{H}$ term of equation C.10a in terms of C.7a through C.7d, and take the dot product with $\underline{\varepsilon}_r^{-1}$

$$\nabla x\left[\frac{\underline{x}_o}{\varepsilon_x}\left(\frac{dH_Z}{dy}-\frac{dH_Y}{dz}\right)+\frac{\underline{y}_o}{\varepsilon_y}\left(\frac{dH_X}{dz}-\frac{dH_Z}{dx}\right)+\frac{\underline{z}_o}{\varepsilon_z}\left(\frac{dH_Y}{dx}-\frac{dH_X}{dy}\right)\right]=k_o^2\underline{\mu}_r\cdot\underline{H} \quad \text{(C.11)}$$

.

Evaluating the remaining cross product of equation C.11 yields the final form of the expanded wave equation, which we will use to solve for the dispersion relationship in terms of $\underline{H}_z$

$$\underline{x}_o\Pi_x+\underline{y}_o\Pi_y+\underline{z}_o\Pi_z=k_o^2\underline{\mu}_r\cdot\underline{H}, \quad \text{(C.12)}$$

$$\Pi_x=\left(\frac{1}{\varepsilon_z}\frac{d^2H_Y}{dxdy}-\frac{1}{\varepsilon_z}\frac{d^2H_x}{dy^2}-\frac{1}{\varepsilon_y}\frac{d^2H_x}{dz^2}+\frac{1}{\varepsilon_y}\frac{d^2H_z}{dxdz}\right), \quad \text{(C.13a)}$$

$$\Pi_y=\left(\frac{1}{\varepsilon_x}\frac{d^2H_z}{dydz}-\frac{1}{\varepsilon_x}\frac{d^2H_y}{dz^2}-\frac{1}{\varepsilon_z}\frac{d^2H_y}{dx^2}+\frac{1}{\varepsilon_z}\frac{d^2H_x}{dxdy}\right), \quad \text{(C.13b)}$$

$$\Pi_z=\left(\frac{1}{\varepsilon_y}\frac{d^2H_x}{dxdz}-\frac{1}{\varepsilon_y}\frac{d^2H_z}{dx^2}-\frac{1}{\varepsilon_x}\frac{d^2H_z}{dy^2}+\frac{1}{\varepsilon_x}\frac{d^2H_y}{dydz}\right). \quad \text{(C.13c)}$$

Taking the dot product of equation C.12 with the $\underline{\mathbf{z}}_o$-direction allows us to isolate the H_z component of the magnetic field on the right hand side of the equation in terms of equation C.13c on the left hand side

$$-\frac{1}{\varepsilon_y}\frac{d^2H_z}{dx^2}-\frac{1}{\varepsilon_x}\frac{d^2H_z}{dy^2}+\frac{1}{\varepsilon_y}\frac{d^2H_x}{dxdz}++\frac{1}{\varepsilon_x}\frac{d^2H_y}{dydz}=k_o^2\mu_zH_z. \quad \text{(C.14)}$$

Setting $E_z = 0$, if we differentiate C.7c by $d^2 / dxdz$ and C.7d by $d^2 / dydz$, keeping in mind that $d/dz = -jk_z$, we arrive at the following result

$$-\frac{1}{\varepsilon_y}\frac{d^2H_z}{dx^2}-\frac{1}{\varepsilon_x}\frac{d^2H_z}{dy^2}+\frac{k_z^2}{\varepsilon_y\left(k_z^2-k_o^2\varepsilon_y\mu_x\right)}\frac{d^2H_z}{dx^2}+\frac{k_z^2}{\varepsilon_x\left(k_z^2-k_o^2\varepsilon_x\mu_y\right)}\frac{d^2H_z}{dy^2}=k_o^2\mu_zH_z \quad \text{(C.15)}$$

.

Combining the d^2H_z/dx^2 and d^2H_z/dy^2 terms in equation C.15 gives the following second order differential dispersion equation for H_z

$$\frac{k_o^2\mu_x}{k_o^2\mu_x\varepsilon_y - k_z^2}\frac{d^2H_z}{dx^2} + \frac{k_o^2\mu_y}{k_o^2\mu_y\varepsilon_x - k_z^2}\frac{d^2H_z}{dy^2} + k_o^2\mu_z H_z = 0. \qquad \text{(C.16)}$$

C.3 Dispersion equation for *Ez*

We expand the $\nabla x\underline{E}$ term of equation C.10b in terms of equations C.7a through C.7d, and take the dot product with $\underline{\underline{\mu_r}}^{-1}$

$$\nabla x\left[\frac{\underline{x}_o}{\mu_x}\left(\frac{dE_Z}{dy} - \frac{dE_Y}{dz}\right) + \frac{\underline{y}_o}{\mu_y}\left(\frac{dE_X}{dz} - \frac{dE_Z}{dx}\right) + \frac{\underline{z}_o}{\mu_z}\left(\frac{dE_Y}{dx} - \frac{dE_X}{dy}\right)\right] = k_o^2\underline{\varepsilon}_r \cdot \underline{E}\,. \qquad \text{(C.17)}$$

Evaluating the remaining cross product of equation C.17 yields the final form of the expanded wave equation, which we will use to solve for the dispersion relationship in terms of E_z

$$\underline{x}_o\xi_x + \underline{y}_o\xi_y + \underline{z}_o\xi_z = k_o^2\underline{\varepsilon}_r \cdot \underline{E}\,, \qquad \text{(C.18)}$$

$$\xi_x = \left(\frac{1}{\mu_z}\frac{d^2E_Y}{dxdy} - \frac{1}{\mu_z}\frac{d^2E_x}{dy^2} - \frac{1}{\mu_y}\frac{d^2E_x}{dz^2} + \frac{1}{\mu_y}\frac{d^2E_z}{dxdz}\right), \qquad \text{(C.19a)}$$

$$\xi_y = \left(\frac{1}{\mu_x}\frac{d^2E_z}{dydz} - \frac{1}{\mu_x}\frac{d^2E_y}{dz^2} - \frac{1}{\mu_z}\frac{d^2E_y}{dx^2} + \frac{1}{\mu_z}\frac{d^2E_x}{dxdy}\right), \qquad \text{(C.19b)}$$

$$\xi_z = \left(\frac{1}{\mu_y}\frac{d^2E_x}{dxdz} - \frac{1}{\mu_y}\frac{d^2E_z}{dx^2} - \frac{1}{\mu_x}\frac{d^2E_z}{dy^2} + \frac{1}{\mu_x}\frac{d^2E_y}{dydz}\right). \qquad \text{(C.19c)}$$

Taking the dot product of equation C.18 with the $\underline{z}_o$-direction allows us to isolate the E_z component of the magnetic field on the right hand side of the equation in terms of equation C.19c on the left hand side

$$-\frac{1}{\mu_y}\frac{d^2E_z}{dx^2}-\frac{1}{\mu_x}\frac{d^2E_z}{dy^2}+\frac{1}{\mu_y}\frac{d^2E_x}{dxdz}++\frac{1}{\mu_x}\frac{d^2E_y}{dydz}=k_o^2\varepsilon_z E_z. \quad \text{(C.20)}$$

Setting $H_z = 0$, if we differentiate equation C.7c by $d^2 / dxdz$ and equation C.7d by $d^2 / dydz$, keeping in mind that $d / dz = -jk_z$, and plug the results into equation C.20, then we arrive at the following result

$$-\frac{1}{\mu_y}\frac{d^2E_z}{dx^2}-\frac{1}{\mu_x}\frac{d^2E_z}{dy^2}+\frac{k_z^2}{\mu_y\left(k_z^2-k_o^2\mu_y\varepsilon_x\right)}\frac{d^2E_z}{dx^2}+\frac{k_z^2}{\mu_x\left(k_z^2-k_o^2\mu_x\varepsilon_y\right)}\frac{d^2E_z}{dy^2}=k_o^2\varepsilon_z E_z. \quad \text{(C.21)}$$

Combining the $d2E_z/dx^2$ and d^2E_z/dy^2 terms in C.21 gives the following second order differential dispersion equation for E_z

$$\frac{k_o^2\varepsilon_x}{k_o^2\mu_y\varepsilon_x-k_z^2}\frac{d^2E_z}{dx^2}+\frac{k_o^2\varepsilon_y}{k_o^2\mu_x\varepsilon_y-k_z^2}\frac{d^2E_z}{dy^2}+k_o^2\varepsilon_z E_z=0. \quad \text{(C.22)}$$

C.4 Suppression of Birefringence

Birefringence is a characteristic of anisotropic media where a single incident wave on the boundary of an anisotropic medium gives rise to two refracted waves as shown in figure C.1 and figure C.2 [10], [30]. We call these two waves the *a*-wave and the *b*-wave otherwise known as the ordinary wave and the extraordinary wave [31]. This property would greatly complicate the description of the fields at a boundary between an anisotropic medium and free space inside a cavity, and this is the crux of our anisotropic transverse resonance calculation in chapter 5. However, for low order resonances, and especially the first resonance, a rectangular cavity suppresses the birefringence inherent to anisotropic media by suppressing propagation in the vertical direction of the waveguide. This suppression assumes that the dimensions of the waveguide are such that the horizontal dimension is at least twice the size of the vertical dimension. To see how

the geometry of the cavity acts to cancel out the extraordinary wave, we need to solve for k_z from our dispersion equations C.16 and/or C.22.

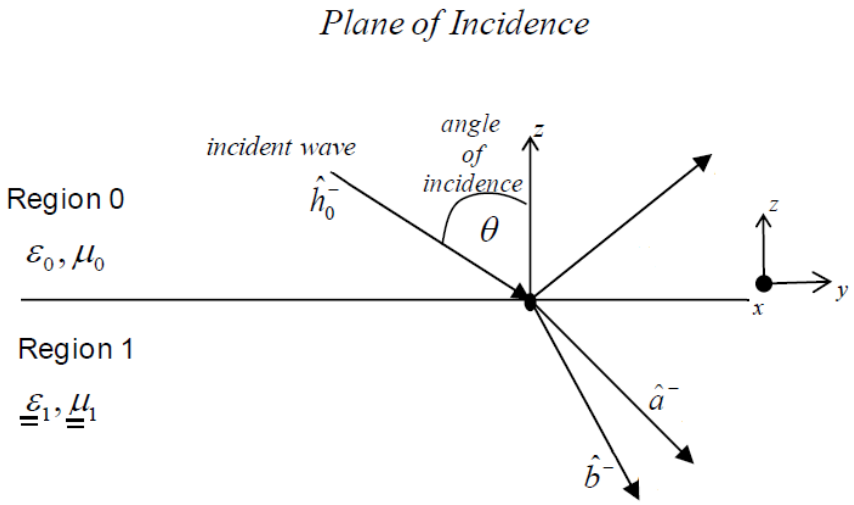

Figure C.1: A plane wave incident from free space on an anisotropic boundary [10].

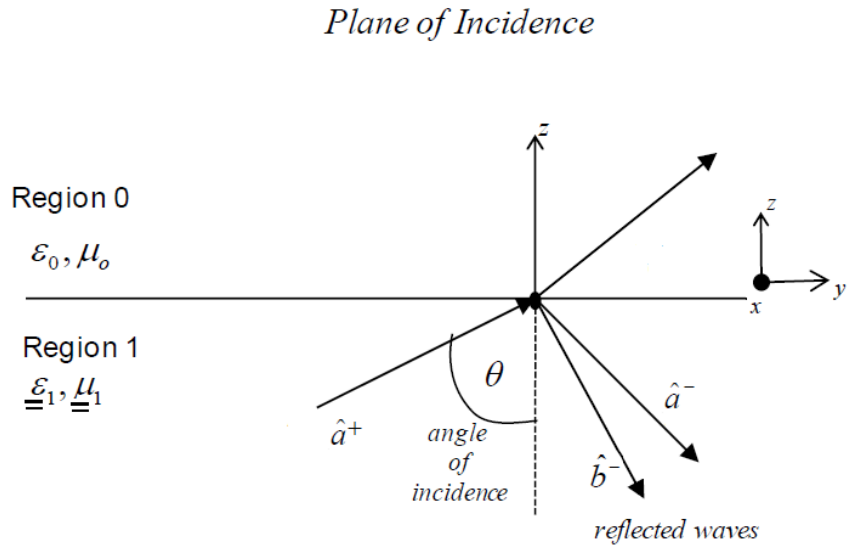

Figure C.2: A plane wave incident from an anisotropic medium on a free space boundary [10].

Equations C.16 and C.22 yield the following solutions in unbounded anisotropic media restricted by the radiation condition in all three dimensions

$$E_z(x,y,z) = E_o e^{-j(k_x x + k_y y + k_z z)}, \tag{C.23a}$$

$$H_z(x,y,z) = H_o e^{-j(k_x x + k_y y + k_z z)}. \tag{C.23b}$$

Plugging equation C.23a into equation C.22 (equivocally we could substitute equation C.23b into equation C.16 allows us to generate a polynomial equation whose solutions give the values of k_z in the anisotropic medium. Noting that $d^2 / dx^2 = -k_x^2$ and $d^2 / dy^2 = -k_y^2$, we arrive at the following equation

$$-\frac{k_o^2 k_x^2 \varepsilon_x}{k_o^2 \mu_y \varepsilon_x - k_z^2} E_z - \frac{k_o^2 \varepsilon_y k_y^2}{k_o^2 \mu_x \varepsilon_y - k_z^2} E_z + k_o^2 \varepsilon_z E_z = 0. \tag{C.24}$$

Dividing out the $k_o^2 E_z$ term and multiplying through by both denominators gives us the following factored polynomial

$$\begin{aligned} -k_x^2 \varepsilon_x \left(k_o^2 \mu_x \varepsilon_y - k_z^2\right) - \varepsilon_y k_y^2 \left(k_o^2 \mu_y \varepsilon_x - k_z^2\right) \\ + \left(k_o^2 \mu_y \varepsilon_x - k_z^2\right)\left(k_o^2 \mu_x \varepsilon_y - k_z^2\right)\varepsilon_z = 0 \end{aligned}. \tag{C.25}$$

Finally, multiplying out equation C.25 yields a fourth order polynomial whose roots yield the four values of k_z describing the ordinary wave and extraordinary wave in the positive and negative propagation directions

$$\begin{aligned} k_z^4 \mu_z + \left[k_x^2 \mu_x + k_y^2 \mu_y - (\varepsilon_x \mu_y + \varepsilon_y \mu_x) k_o^2 \mu_z\right] k_z^2 \\ + \left[k_o^4 \varepsilon_x \varepsilon_y \mu_x \mu_y \mu_z - k_o^2 k_x \varepsilon_x \mu_y \mu_x - k_o^2 \varepsilon_y k_y \mu_x \mu_y\right] = 0 \end{aligned}. \tag{C.26}$$

Equation C.26 is directly responsible for the existence of the second extraordinary wave. In an isotropic medium, the resulting polynomial for k_z is a second order polynomial, which yields only the values for the positive and negative propagation of a

single wave. However, in a rectangular cavity, we assume that the first resonance suppresses the propagation constant in the vertical direction. In other words, $k_y = 0$ and $d^2 / dy^2 = 0$. This simplifies equation C.24 to

$$-\frac{k_o^2 k_x^2 \varepsilon_x}{k_o^2 \mu_y \varepsilon_x - k_z^2} E_z + k_o^2 \varepsilon_z E_z = 0, \tag{C.27}$$

This leads us to the following second order polynomial for k_z

$$k_z^2 = \varepsilon_x \left(k_o^2 \mu_y - \frac{k_x^2}{\varepsilon_z} \right). \tag{C.28}$$

Since equation C.28 yields only two solutions, this indicates the existence of only a single propagating wave. The suppression of the k_y term in the first resonance of the rectangular cavity yields a second order differential equation for the wave number in the propagation direction, thereby eliminating the property of birefringence for this case.

Appendix D
Modal Decomposition Matrix for Determining the Fourier Transform of the Fields at the Aperture of a Radiating Semi-Infinite Waveguide

The analysis of the radiating infinite flange problem has been widely studied and different methods for determining the aperture fields are presented in the published literature [27]-[34]. Flush mounted aperture antennas are widely used and are often approximated by an aperture in an infinite conducting surface (infinite flange). Furthermore, the solutions determined by these methods reasonably approximate those of a radiating waveguide with no infinite conducting surface [35]. Although accurate, these methods require the rigorous calculation of the fields at the aperture of the waveguide. This paper illustrates a more straightforward approach that directly computes the radiated far field eliminating the requirement for the aperture field. This approach uses a modal decomposition matrix (MDM) method based on a sampling of the transverse free space wave number to determine the aperture components of the widely used stationary phase approach. The results determined by our method are compared to the far field radiation patterns achieved by CST Studio Suite for the same problem.

D.1 Modal Decomposition of a Rectangular Waveguide

This section describes the theory of matching the transverse electric and magnetic fields that exist inside a uniform rectangular waveguide to those of the radiated far fields in free space. The modal decomposition described here is based on the theory first published by Marcuvitz [25], [36]. The transverse field inside the guide is assumed to be generated from the dominant propagating mode inside the waveguide. The dominant mode is determined by the lowest cutoff frequency in the waveguide and for a rectangular waveguide the TE_{10} mode is the dominant mode.

By matching to the spectral component of the far radiated field at the aperture, a system of equations is derived that will directly yield the Fourier transform of the transverse aperture field. Based on this we can use the stationary phase approximation to calculate the far field radiation patterns.

Figure D.1a and figure D.1b show two orientations of the same rectangular waveguide. We depict a half space boundary at the aperture ($z = 0$) in Figure D.1a, and the waveguide extends to $-\infty$ in the z-direction. Felsen and Marcuvitz define this as the semi-infinite waveguide approximation [36]. Using this approximation, we can construct the form of the electric and magnetic fields that exist inside the waveguide due to an incident TE_{10} mode.

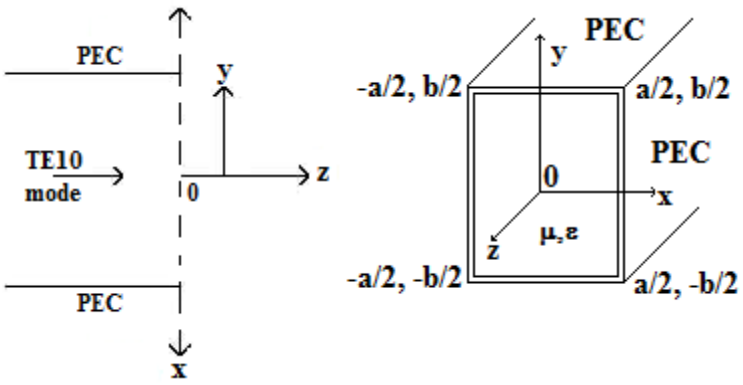

(a) (b)

Figure D.1: (a) Half space boundary between the waveguide aperture and free space.

(b) Transverse (x,y) cross section of the waveguide.

D.1.1 Incident TE_{10} Mode

We assume the incident TE_{10} wave shown in figure D.1a exists inside the waveguide with the following form

$$\underline{E}_{Tinc}(\underline{r}) = \underline{e}''_{N}(x,y)V(z), \tag{D.1a}$$

$$\underline{H}_{Tinc}\left(\underline{r}\right)=\underline{h}''_{N}(x,y)I\left(z\right), \tag{D.1b}$$

where *V(z)* and *I(z)* are the voltage and current at point *z* inside the waveguide, and are defined by solutions to the wave equation. The subscript *N* denotes that this is the incident mode impingent on the aperture ($z = 0$) and the superscript '' denotes that this is a TE mode. Later in this document the superscript ' will denote the transverse magnetic (TM) mode.

We define the mode functions $\underline{e}_{\upsilon}(x,y)$ and $\underline{h}_{\upsilon}(x,y)$ as [36]

$$\begin{aligned}\underline{e}'_{\upsilon}(x,y) &= -\nabla_T\Phi_{\upsilon}(x,y)\\ &= -A'_{\upsilon}\left[\underline{x}_o\frac{m\pi}{a}\cos\left(\frac{m\pi}{a}\left(x+\frac{a}{2}\right)\right)\sin\left(\frac{n\pi}{b}\left(y+\frac{b}{2}\right)\right)\right.\\ &\qquad\left.+\,\underline{y}_o\frac{n\pi}{b}\sin\left(\frac{m\pi}{a}\left(x+\frac{a}{2}\right)\right)\cos\left(\frac{n\pi}{b}\left(y+\frac{b}{2}\right)\right)\right]\end{aligned}, \tag{D.2a}$$

$$\begin{aligned}\underline{h}'_{\upsilon}(x,y) &= \hat{a}_Z\times\underline{e}'_{\upsilon}(x,y)\\ &= A'_{\upsilon}\left[\underline{x}_o\frac{n\pi}{b}\sin\left(\frac{m\pi}{a}\left(x+\frac{a}{2}\right)\right)\cos\left(\frac{n\pi}{b}\left(y+\frac{b}{2}\right)\right)\right.\\ &\qquad\left.-\,\underline{y}_o\frac{m\pi}{a}\cos\left(\frac{m\pi}{a}\left(x+\frac{a}{2}\right)\right)\sin\left(\frac{n\pi}{b}\left(y+\frac{b}{2}\right)\right)\right]\end{aligned}, \tag{D.2b}$$

$$\begin{aligned}\underline{e}''_{\upsilon}(x,y) &= \underline{h}''_{\upsilon}(x,y)\times\hat{a}_Z\\ &= A''_{\upsilon}\left[\underline{x}_o\frac{n\pi}{b}\cos\left(\frac{m\pi}{a}\left(x+\frac{a}{2}\right)\right)\sin\left(\frac{n\pi}{b}\left(y+\frac{b}{2}\right)\right)\right.\\ &\qquad\left.-\,\underline{y}_o\frac{m\pi}{a}\sin\left(\frac{m\pi}{a}\left(x+\frac{a}{2}\right)\right)\cos\left(\frac{n\pi}{b}\left(y+\frac{b}{2}\right)\right)\right]\end{aligned}, \tag{D.2c}$$

$$\begin{aligned}\underline{h}''_{\upsilon}(x,y) &= -\nabla_T \Psi_{\upsilon}(x,y) \\ &= A''_{\upsilon}\left[\underline{x}_o \frac{m\pi}{a}\sin\left(\frac{m\pi}{a}\left(x+\frac{a}{2}\right)\right)\cos\left(\frac{n\pi}{b}\left(y+\frac{b}{2}\right)\right)\right. \\ &\qquad \left. + \underline{y}_o \frac{n\pi}{b}\cos\left(\frac{m\pi}{a}\left(x+\frac{a}{2}\right)\right)\sin\left(\frac{n\pi}{b}\left(y+\frac{b}{2}\right)\right)\right]\end{aligned}, \tag{D.2d}$$

where υ represents the *(m,n)* pair known as the mode number. The two mode number indices can take integer values greater than zero. For instance, the TE_{10} mode has mode indices of $m = 1$ and $n = 0$. A'_{υ} and A''_{υ} are determined by normalizing equations D.2a through D.2d across the transverse (x,y) plane of the waveguide in figure D.1b as

$$A'^{2}_{mn}\int_{-\frac{b}{2}}^{\frac{b}{2}}\int_{-\frac{a}{2}}^{\frac{a}{2}} \underline{e}'_{mn}(x,y)\bullet\underline{e}'_{kl}(x,y)dxdy = \delta_{mk}\delta_{nl}, \tag{D.3a}$$

$$A''^{2}_{mn}\int_{-\frac{b}{2}}^{\frac{b}{2}}\int_{-\frac{a}{2}}^{\frac{a}{2}} \underline{e}''_{mn}(x,y)\bullet\underline{e}''_{kl}(x,y)dxdy = \delta_{mk}\delta_{nl}, \tag{D.3b}$$

where δ_{mk} is defined as $\delta_{mk} = 0$ for $m \neq k$ and $\delta_{mm} = 0$. Solving equations D.3a and D.3b for the normalization constants yields

$$A'_{mn} = \left(\frac{2}{\pi}\right)\frac{\mathrm{P}_{mn}}{\sqrt{m^2\frac{a}{b}+n^2\frac{b}{a}}}, \tag{D.4a}$$

$$A''_{mn} = \left(\frac{\sqrt{\xi_m\xi_n}}{\pi}\right)\frac{\mathrm{P}_{mn}}{\sqrt{m^2\frac{b}{a}+n^2\frac{a}{b}}}, \quad \xi_m,\xi_n = \begin{cases}1;\ m,n=0\\ 2;\ m,n=0\end{cases}, \tag{D.4b}$$

where P_{mn} is the incident mode's amplitude.

Taking equations D.2a, D.2b, D.4a, and D.4b into account we construct the total transverse $\underline{\boldsymbol{E}}_T$ and $\underline{\boldsymbol{H}}_T$ fields inside the waveguide for $z \le 0$

$$\underline{E}_T(\underline{r}) = \underline{e}''_N(x,y)e^{-j\kappa''_N z} + \Gamma''_N(z)\underline{e}''_N(x,y)e^{+j\kappa''_N z} + \sum_{M\neq N}\left[\Gamma'_M(z)\underline{e}'_M(x,y)e^{+j\kappa'_M z} + \Gamma''_M(z)\underline{e}''_M(x,y)e^{+j\kappa''_M z}\right], \tag{D.5a}$$

$$\underline{H}_T(\underline{r}) = Y''_N\,\underline{h}''_N(x,y)e^{-j\kappa''_N z} - Y''_N\Gamma''_N(z)\underline{h}''_N(x,y)e^{+j\kappa''_N z}) - \sum_{M\neq N}\left[Y'_N\Gamma'_M(z)\underline{h}'_M(x,y)e^{+j\kappa'_N z} + Y''_N\Gamma''_M\,\underline{h}''_M(x,y)e^{+j\kappa''_N z}\right], \tag{D.5b}$$

where the subscript M denotes all mode numbers that are not incident on the aperture. Notice that both the incident and non-incident modes are reflected from the aperture at $z = 0$. Z'_υ, Z''_υ, and κ_υ are defined by

$$Z'_\upsilon = \frac{1}{Y'_\upsilon} = \frac{\kappa_\upsilon}{\omega\varepsilon}, \tag{D.6a}$$

$$Z''_\upsilon = \frac{1}{Y''_\upsilon} = \frac{\omega\mu}{\kappa_\upsilon}, \tag{D.6b}$$

$$\kappa_\upsilon = \sqrt{k^2 - k_{T\upsilon}^2}, \tag{D.6c}$$

$$k_{T\upsilon}^2 = k_x^2 + k_y^2 = \left(\frac{m\pi}{a}\right)^2 + \left(\frac{n\pi}{b}\right)^2. \tag{D.6d}$$

Here k is the free space wave number and $k_{T\upsilon}$ is the transverse wave number within the waveguide. The equations for the radiated transverse electric and magnetic fields beyond the aperture ($z \ge 0$) can be defined via a Fourier transform for when $z \ge 0$

$$\underline{E}_T(\underline{r}) = \frac{1}{(2\pi)^2}\int_{-\infty}^{\infty}\int_{-\infty}^{\infty}\tilde{\underline{E}}_T(k_x,k_y)e^{-j\underline{k}\cdot\underline{r}}dk_x dk_y, \tag{D.7a}$$

$$\underline{H}_T(\underline{r}) = \frac{1}{(2\pi)^2}\int_{-\infty}^{\infty}\int_{-\infty}^{\infty}\underline{\tilde{H}}_T(k_x,k_y)e^{-j\underline{k}\cdot\underline{r}}dk_x dk_y\,, \tag{D.7b}$$

where the ~ denotes that these components exist in the spectral domain and $\underline{\boldsymbol{r}} = x\cdot\underline{\boldsymbol{x}}_o + y\cdot\underline{\boldsymbol{y}}_o + z\cdot\underline{\boldsymbol{z}}_o$.

In order to determine the fields at the aperture, we equate equation D.5a to equation D.7a and equation D.5b to equation D.7b. Setting $z = 0$ results in

$$(1+\Gamma''_N)\underline{e}''_N(x,y) + \sum_{M\neq N}\left[\Gamma''_M\,\underline{e}''_M(x,y) + \Gamma''_M\,\underline{e}''_M(x,y)\right] = \frac{1}{(2\pi)^2}\int_{-\infty}^{+\infty}\int_{-\infty}^{+\infty}\underline{\tilde{E}}(k_x,k_y)e^{-j\underline{k}_T\bullet\underline{\rho}}dk_x dk_y\,, \tag{D.8a}$$

$$(1-\Gamma''_N)\frac{\underline{h}''_N(x,y)}{Z''_N} - \sum_{M\neq N}\left[\Gamma''_N\frac{\underline{h}''_N(x,y)}{Z''_N} + \Gamma'_N\frac{\underline{h}'_N(x,y)}{Z'_N}\Gamma'_N\right] = \frac{1}{(2\pi)^2}\int_{+\infty}^{+\infty}\int_{+\infty}^{+\infty}\underline{\tilde{H}}(k_x,k_y)e^{-j\underline{k}_T\bullet\underline{\rho}}dk_x dk_y\,, \tag{D.8b}$$

where $\underline{\boldsymbol{k}}_T = k_x\cdot\underline{\boldsymbol{x}}_o + k_y\cdot\underline{\boldsymbol{y}}_o$, Γ is the reflection coefficient at the aperture, and $\underline{\boldsymbol{\rho}} = x\cdot\underline{\boldsymbol{x}}_o + y\cdot\underline{\boldsymbol{y}}_o$. Notice that on the right side of equations D.8a and D.8b, the $\underline{k}\cdot\underline{r}$ from equations D.7a and D.7b becomes $\underline{\boldsymbol{k}}\cdot\underline{\boldsymbol{\rho}}$ at the aperture due to $z = 0$. The following orthogonality equations

$$\iint_S \underline{e}_k(x,y)\bullet\underline{e}_l(x,y)dxdy = \delta_{kl}\,, \tag{D.9a}$$

$$\iint_S \underline{h}_k(x,y)\bullet\underline{h}_l(x,y)dxdy = \delta_{kl}\,, \tag{D.9b}$$

allow us to simplify equations D.8a and D.8b in terms of the reflection coefficients and spectral components of the $\underline{\boldsymbol{E}}_T$ and $\underline{\boldsymbol{H}}_T$ fields [36]. Here S is the surface dimensions of the transverse (x,y) plane of the rectangular waveguide. By limiting the bounds of

integration in equations D.9a and D.9b, we enforce the boundary condition that $\underline{\boldsymbol{E}}_T(\underline{\boldsymbol{r}}) = 0$ on the surface of the flange. Using the following general substitution

$$\hat{\underline{\tau}}_\upsilon(\underline{k}_T) = \iint_S \frac{e^{-j\underline{k}_T \bullet \underline{\rho}}}{(2\pi)^2} \underline{\tau}_\upsilon(x,y)dxdy, \tag{D.10}$$

we can rewrite equations D.8a and D.8b as the following system of equations

$$(1+\Gamma''_N) = \iint \left(\hat{\underline{e}}''_N(k_x,k_y) \bullet \tilde{\underline{E}}_T(k_x,k_y)\right)dk_x dk_y = \left(\hat{\underline{e}}''_N(k_x,k_y),\, \tilde{\underline{E}}_T(k_x,k_y)\right) \tag{D.11a}$$

,

$$\begin{aligned}(1-\Gamma''_N) = Z''_N \iint \underline{h}''_N(k_x,k_y) \bullet \tilde{\underline{H}}_T(k_x,k_y)dk_x dk_y \\ = Z''_N \left(\underline{h}''_N(k_x,k_y),\, \tilde{\underline{H}}_T(k_x,k_y)\right),\end{aligned} \tag{D.11b}$$

$$\Gamma''_M = \left(\hat{\underline{e}}''_M(k_x,k_y),\, \tilde{\underline{E}}_T(k_x,k_y)\right), \tag{D.11c}$$

$$\Gamma''_M = -Z''_M \left(\underline{h}''_N(k_x,k_y),\, \tilde{\underline{H}}_T(k_x,k_y)\right), \tag{D.11d}$$

$$(1+\Gamma'_N) = \left(\hat{\underline{e}}'_N(k_x,k_y),\, \tilde{\underline{E}}_T(k_x,k_y)\right), \tag{D.11e}$$

$$(1-\Gamma'_N) = Z'_N \left(\underline{h}'_N(k_x,k_y),\, \tilde{\underline{H}}_T(k_x,k_y)\right), \tag{D.11f}$$

$$\Gamma'_M = \left(\hat{\underline{e}}'_M(k_x,k_y),\, \tilde{\underline{E}}_T(k_x,k_y)\right), \tag{D.11g}$$

$$\Gamma'_M = -Z''_M \left(\underline{h}''_N(k_x,k_y),\, \tilde{\underline{H}}_T(k_x,k_y)\right). \tag{D.11h}$$

This set of equations will be used to solve for the spectral components of the fields at the aperture. The solutions to the surface integrals $\hat{\underline{e}}_N(k_x,k_y)$ and $\underline{h}_N(k_x,k_y)$ can be determined in closed form, and solutions are derived in the appendix. In order to get

equations D.11a through D.11f into matrix form we need to combine $\hat{\underline{e}}_N(k_x,k_y)$ and $\underline{h}_N(k_x,k_y)$. By adding like Γ_υ terms together from equations D.11a through D.11f we can rewrite the entire system of equations using the following two expressions

$$\left(\hat{\underline{e}}''_\upsilon(k_x,k_y),\, \tilde{\underline{E}}_T(k_x,k_y)\right)+Z''_\upsilon\left(\underline{h}''_\upsilon(k_x,k_y),\, \tilde{\underline{H}}_T(k_x,k_y)\right)=2\delta_{\upsilon N}, \qquad \text{(D.12a)}$$

$$\left(\hat{\underline{e}}'_\upsilon(k_x,k_y),\, \tilde{\underline{E}}_T(k_x,k_y)\right)+Z'_\upsilon\left(\underline{h}'_\upsilon(k_x,k_y),\, \tilde{\underline{H}}_T(k_x,k_y)\right)=2\delta_{\upsilon N}. \qquad \text{(D.12b)}$$

The impedances Z' and Z''_υ are known quantities given by equations D.6a and D.6b. The terms $\hat{\underline{e}}_\upsilon(k_x,k_y)$ and $\underline{h}_\upsilon(k_x,k_y)$ are surface integrals that are directly calculated as constants based on equation D.10 and equations D.2a through D.2d.

D.2 Formulation of the MDM Method

The basis of the MDM method is the MDM itself. This matrix is based on the system of equations formulated by equations D.12a through D.12b. By representing the integrals in $\underline{k}_T$ space as a Riemann Sum over k_x and k_y, we formulate a matrix equation that we can solve directly.

D.2.1 *Derivation of MDM Equation*

To simplify equations D.12a and D.12b, we write $\tilde{\underline{H}}_T(k_x,k_y)$ in terms of $\tilde{\underline{E}}_T(k_x,k_y)$ leaving a single unknown. Starting with the expression

$$\tilde{\underline{H}}_T(k_x,k_y)=\frac{1}{\omega\mu_o}\left[\left(a_z\times\tilde{\underline{E}}_T(k_x,k_y)\right)k_{z\upsilon}-\left(\frac{\underline{k}_T\times a_z}{k_{z\upsilon}}\right)\left(\underline{k}_T\bullet\tilde{\underline{E}}_T(k_x,k_y)\right)\right], \qquad \text{(D.13)}$$

we can rewrite this as the matrix equation

$$\underline{\tilde{H}}_T(k_x,k_y)=\begin{bmatrix}\tilde{H}_x(k_x,k_y)\\ \tilde{H}_y(k_x,k_y)\end{bmatrix}=\begin{bmatrix}A_{xx} & A_{xy}\\ A_{yx} & A_{yy}\end{bmatrix}\begin{bmatrix}\tilde{E}_x(k_x,k_y)\\ \tilde{E}_y(k_x,k_y)\end{bmatrix}=\underline{\underline{A}}\bullet\underline{\tilde{E}}_T(k_x,k_y), \qquad \text{(D.4)}$$

and then solve for $\underline{\underline{\boldsymbol{A}}}$ using the expression on the right side of equation D.13. Evaluating the cross products of equation D.13 and dot product of equation D.14 yields

$$\begin{aligned}\underline{\tilde{H}}_T(k_x,k_y)&=\frac{1}{\omega\mu_o}\left\{\begin{bmatrix}0 & -\kappa_\upsilon\\ \kappa_\upsilon & 0\end{bmatrix}-\begin{bmatrix}\frac{k_xk_y}{\kappa_\upsilon} & \frac{k_y^2}{\kappa_\upsilon}\\ -\frac{k_x^2}{\kappa_\upsilon} & -\frac{k_xk_y}{\kappa_\upsilon}\end{bmatrix}\right\}\begin{bmatrix}\tilde{E}_x(k_x,k_y)\\ \tilde{E}_y(k_x,k_y)\end{bmatrix}\\ &=\frac{1}{\omega\mu_o\kappa_\upsilon}\left\{\begin{bmatrix}-k_xk_y & -\left(k_o^2-k_x^2\right)\\ k_o^2-k_y^2 & k_xk_y\end{bmatrix}\right\}\begin{bmatrix}\tilde{E}_x(k_x,k_y)\\ \tilde{E}_y(k_x,k_y)\end{bmatrix}=\underline{\underline{A}}\bullet\underline{\tilde{E}}_T(k_x,k_y)\end{aligned}. \qquad \text{(D.15)}$$

Equation D.15 represents a shorthand notation to represent the system of equations that will construct our MDM equation. However, to properly explain how these equations represent a matrix equation, it is better to think of these equations in longhand notation. We now express equations D.12a and D.12b as

$$\int_{-\infty}^{\infty}\int_{-\infty}^{\infty}\left[\underline{\hat{e}}''_\upsilon(k_x,k_y)+Z''_\upsilon\left(\underline{\underline{A}}\bullet\underline{h}''_\upsilon(k_x,k_y)\right)\right]\bullet\underline{\tilde{E}}_T(k_x,k_y)dk_xdk_y=2\delta_{\upsilon N}, \qquad \text{(D.16a)}$$

$$\int_{-\infty}^{\infty}\int_{-\infty}^{\infty}\left[\underline{\hat{e}}'_\upsilon(k_x,k_y)+Z'_\upsilon\left(\underline{\underline{A}}\bullet\underline{h}''_\upsilon(k_x,k_y)\right)\right]\bullet\underline{\tilde{E}}_T(k_x,k_y)dk_xdk_y=2\delta_{\upsilon N}. \qquad \text{(D.16b)}$$

This set of equations allows us to solve for $\underline{\tilde{E}}_T(k_x,k_y)$ explicitly if we can numerically compute the integrals and know the total number of non-incident modes needed to accurately reconstruct the aperture field. If we redefine the integrals as a Riemann sum, then equations D.16a and D.16b become

$$\sum_{k_y}\sum_{k_x}\underbrace{\left[\left(\hat{\underline{e}}''_{\upsilon}\left(k_x,k_y\right)+Z''_{\upsilon}\,\underline{\underline{A}}\bullet\underline{h}''_{\upsilon}\left(k_x,k_y\right)\right)\bullet\tilde{\underline{E}}_T\left(k_x,k_y\right)\right]}_{M''_{\upsilon x}\left(k_x,k_y\right)\underline{x}_o+M''_{\upsilon y}\left(k_x,k_y\right)\underline{y}_o}\Delta k_x\Delta k_y=2\delta_{\upsilon N}\,, \tag{D.17a}$$

$$\sum_{k_y}\sum_{k_x}\underbrace{\left[\left(\hat{\underline{e}}'_{\upsilon}\left(k_x,k_y\right)+Z'_{\upsilon}\,\underline{\underline{A}}\bullet\underline{h}'_{\upsilon}\left(k_x,k_y\right)\right)\bullet\tilde{\underline{E}}_T\left(k_x,k_y\right)\right]}_{M'_{\upsilon x}\left(k_x,k_y\right)\underline{x}_o+M'_{\upsilon y}\left(k_x,k_y\right)\underline{y}_o}\Delta k_x\Delta k_y=2\delta_{\upsilon N}\,, \tag{D.17b}$$

where $M''_{\upsilon x}(k_x,k_y)$, $M''_{\upsilon y}(k_x,k_y)$, $M'_{\upsilon x}(k_x,k_y)$, and $M'_{\upsilon y}(k_x,k_y)$ will represent elements of the MDM. We now write the MDM equation from equations D.17a and D.17b to solve for the spectral transverse aperture field $\tilde{\underline{E}}_T(k_x,k_y)$. In doing so, each value of υ representing a different mode inside the waveguide will represent the MDM row index. Since we need an invertible matrix to obtain a solution, υ also represents the discrete index of k_x and k_y in free space which becomes the column index of our matrix. This creates a square matrix with a total of L samples of k_x and k_y as well as L modes

$$2L\left\{\overbrace{\begin{array}{c}TE\\ \\ \\ \\ TM\\ \\ \\ \end{array}\left[\begin{array}{cccc|cccc}
\multicolumn{4}{c|}{\underline{x}_o-direction} & \multicolumn{4}{c}{\underline{y}_o-direction}\\
M''_{1x}(\underline{k}_{T1}) & M''_{1x}(\underline{k}_{T2}) & \dots & M''_{1x}(\underline{k}_{TL}) & M''_{1y}(\underline{k}_{T1}) & M''_{1y}(\underline{k}_{T2}) & \dots & M''_{1y}(\underline{k}_{TL})\\
M''_{2x}(\underline{k}_{T1}) & M''_{2x}(\underline{k}_{T2}) & \dots & M''_{2x}(\underline{k}_{TL}) & M''_{2y}(\underline{k}_{T1}) & M''_{2y}(\underline{k}_{T2}) & \dots & M''_{2y}(\underline{k}_{TL})\\
\vdots & \vdots & & \vdots & \vdots & \vdots & & \vdots\\
M''_{Lx}(\underline{k}_{T1}) & M''_{Lx}(\underline{k}_{T2}) & \dots & M''_{Lx}(\underline{k}_{TL}) & M''_{Ly}(\underline{k}_{T1}) & M''_{Ly}(\underline{k}_{T2}) & \dots & M''_{Ly}(\underline{k}_{TL})\\
\hline
M'_{1x}(\underline{k}_{T1}) & M'_{1x}(\underline{k}_{T2}) & \dots & M'_{1x}(\underline{k}_{TL}) & M'_{1y}(\underline{k}_{T1}) & M'_{1y}(\underline{k}_{T2}) & \dots & M'_{1y}(\underline{k}_{TL})\\
M'_{2y}(\underline{k}_{T1}) & M'_{2x}(\underline{k}_{T2}) & \dots & M'_{2x}(\underline{k}_{TL}) & M'_{2y}(\underline{k}_{T1}) & M'_{2y}(\underline{k}_{T2}) & \dots & M'_{2y}(\underline{k}_{TL})\\
\vdots & \vdots & & \vdots & \vdots & \vdots & & \vdots\\
M'_{Nx}(\underline{k}_{T1}) & M'_{Nx}(\underline{k}_{T2}) & \dots & M'_{Lx}(\underline{k}_{TL}) & M'_{Ly}(\underline{k}_{T1}) & M'_{Ly}(\underline{k}_{T2}) & \dots & M'_{Ly}(\underline{k}_{TL})
\end{array}\right]}^{2L}\right.\bullet\left[\begin{array}{c}\tilde{E}_x(\underline{k}_{T1})\\ \tilde{E}_x(\underline{k}_{T2})\\ \vdots\\ \tilde{E}_x(\underline{k}_{TL})\\ \hline \tilde{E}_y(\underline{k}_{T1})\\ \tilde{E}_y(\underline{k}_{T2})\\ \vdots\\ \tilde{E}_y(\underline{k}_{TL})\end{array}\right]=\left[\begin{array}{c}2\\0\\ \vdots\\ \vdots\\ \vdots\\ \vdots\\ \vdots\\ \vdots\\ \vdots\\ 0\end{array}\right]. \tag{D.18}$$

The MDM of equation D.18 has four separate quadrants. Quadrant 1 corresponds to the matrix elements that represent the TE modes inside the waveguide in the x-direction, quadrant 2 corresponds to the matrix elements that represent the TE modes inside the waveguide in the y-direction, quadrant 3 corresponds to the matrix elements

that represent the TM modes inside the waveguide in the x-direction, and quadrant 4 corresponds to the matrix elements that represent the TM modes inside the waveguide in the y-direction. We also use ($\underline{k}_{Tv}$) to represent the (k_x,k_y) pair. The reason we separate the x-components and the y-components of the MDM equation is so we can solve for $\tilde{E}_x(k_x,k_y)$ and $\tilde{E}_y(k_x,k_y)$ individually. Each quadrant is L x L in dimension yielding a $2L$ x $2L$ square matrix. The solutions to $\tilde{E}_x(k_x,k_y)$ and $\tilde{E}_y(k_x,k_y)$ are L element vectors. Note that the right hand side vector of equation D.18 is zero except for the first element which corresponds to the incident TE_{10} mode in the waveguide.

As with any numerical approximation to a continuous function, L must be large enough to ensure an accurate representation of the original function. However, a large L means that many more modes must be used in the MDM equation than are truly necessary to accurately determine the electric field inside the waveguide accurately. This can lead to a singular matrix, which by definition is not invertible. Therefore, in solving equation D.18 we must use singular value decomposition (SVD) to determine the inverse of the MDM [37].

D.2.2 *Representation of k_x and k_y when $z \geq 0^+$*

This section describes how to represent the values of k_x and k_y in the MDM equation. Since it is desirable to represent the stationary phase approximation of the far field in spherical coordinates (r,θ,ϕ), we must map k_x and k_y to spherical coordinates to use in the stationary phase. The stationary phase approximation is well known and widely used throughout the literature [36], [38], [39]. We repeat the stationary phase equation from Balanis [38] here for convenience

$$\underline{E}(r,\theta,\phi) \approx j\frac{ke^{-jkr}}{2\pi r}\left[\underline{\theta}_o\left\{\tilde{E}_x\left(k_x,k_y,z=0\right)\cos\phi+\tilde{E}_y\left(k_x,k_y,z=0\right)\sin\phi\right\}\right.$$
$$\left.+\,\underline{\phi}_o\left(-\tilde{E}_x\left(k_x,k_y,z=0\right)\sin\phi+\tilde{E}_y\left(k_x,k_y,z=0\right)\cos\phi\right)\cos\theta\right]. \quad \text{(D.19)}$$

Mapping k_x and k_y to spherical yields

$$k_x = k_o\sin(\theta)\cos(\phi), \quad \text{(D.20a)}$$

$$k_y = k_o\sin(\theta)\sin(\phi). \quad \text{(D.20b)}$$

In order to get a hemispherical mapping of the radiated electric field in the positive propagation direction, we are interested in $-\pi/2 \le \theta \le \pi/2$ and $0 \le \phi \le \pi/2$. After substituting these values of θ and ϕ into equations D.20a and equations D.20b, we get a trajectory of k_x and k_y onto a circle of radius k_o as shown in figure D.2

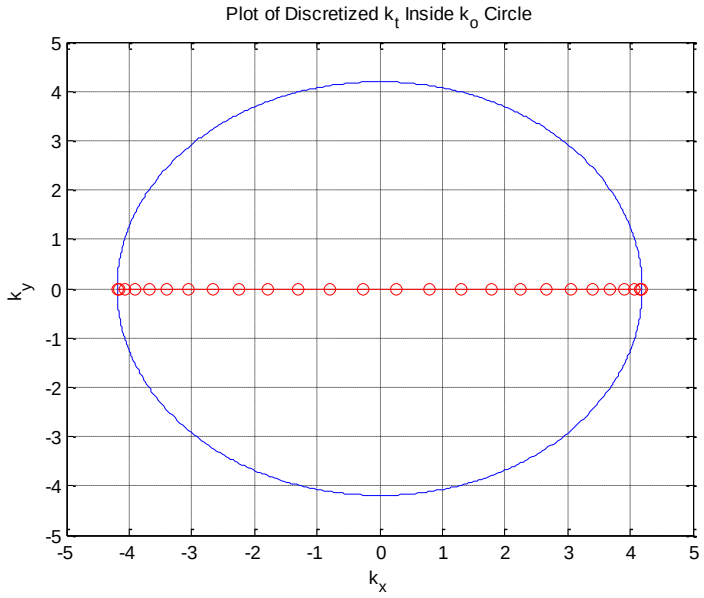

Figure D.2: Plot of the values of k_x and k_y obtained for $\phi = 0$.

Figure D.2 shows all the k_x and k_y values obtained for $\phi = 0$ and $\Delta\theta = 1/L$ where L corresponds to the size of each quadrant in equation D.18. The angle of ϕ is represented in figure D.2 as the angle between the k_x and k_y axes. Since $\phi = 0$, all the k_x and k_y values

fall on the $k_y = 0$ axis. If we use $\phi = \pi/4$ to calculate k_x and k_y as in figure D.3, then we see that the values of k_x and k_y fall on a trajectory that makes an angle of $\pi/4$ with the $k_y = 0$ axis.

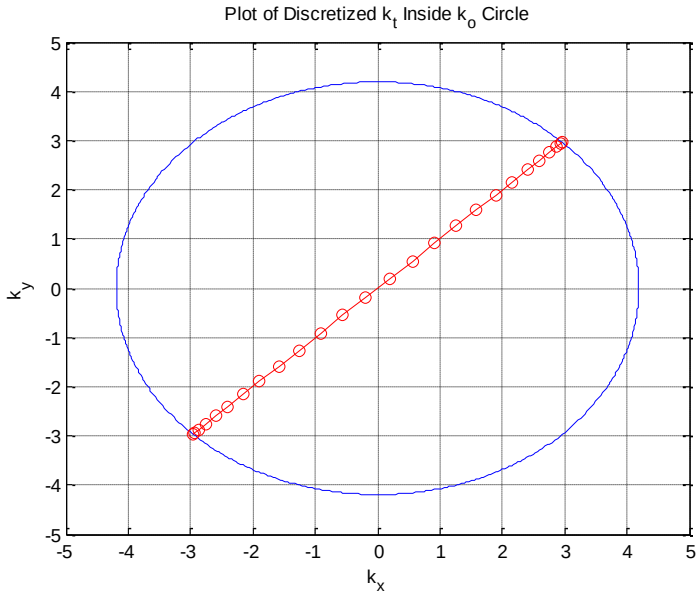

Figure D.3: Plot of the values of k_x and k_y obtained for $\phi = \pi/4$.

Using this technique we can generate the far radiated electric field for any value of $0 \leq \phi \leq \pi/2$. Note that in both figure D.2 and figure D.3 an equal spacing between values of θ does not result in an equal spacing in k_x and k_y. Also, any value of k_x and k_y that falls on the k_o radius yields a value of $|\underline{k}_T| = k_o$ which corresponds to $\kappa = 0$. Any value of k_x and k_y that falls beyond the k_o radius corresponds to an imaginary value of κ. These values represent attenuating modes not and therefore will not be used in the calculations for the incident TE_{10} mode.

D.3 Calculation of Far Field and Comparison to Simulation

This section compares the far field radiation pattern numerically calculated from the MDM method described in section D.2 to those generated using 3D electromagnetic

modeling software. The MDM calculations were performed using Matlab while the numerical simulations were performed with CST Studio Suite 2014 which is a finite-difference time-domain (FDTD) code.

D.3.1 *Description of CST Model*

In order to validate the accuracy of the MDM method, we will compare the analytical results to those generated by a CST Studio Suite 2014 model. Figure D.4 and figure D.5 depict the model we use to simulate the semi-infinite rectangular waveguide with an infinite flange. Figure D.4 gives the transverse dimensions of the waveguide where $a = \lambda/2$ at 200 megahertz (MHz) and $b = a/2.25$. As long as $a \geq 2b$, the dominant mode will be the TE_{10} mode. The cutoff frequency (f_c) for the propagation of the dominant mode is 200 MHz and f_c for the next mode to propagate is 400 MHz. For frequencies below 200 MHz no modes will propagate in the waveguide, and for frequencies above 400 MHz more than one mode will propagate in the waveguide. Since the method described in section D.2 corresponds to a waveguide that is infinite in one direction and ends at a radiating flange aperture at $z = 0$, placing a waveguide port at the end of the waveguide mimics this setup as shown in figure D.5. The waveguide port will absorb any reflections of additional modes at the aperture to ensure that only the propagating TE_{10} mode will be incident at the aperture. The direction of the arrow in figure D.5 shows the direction of propagation for the TE_{10} mode.

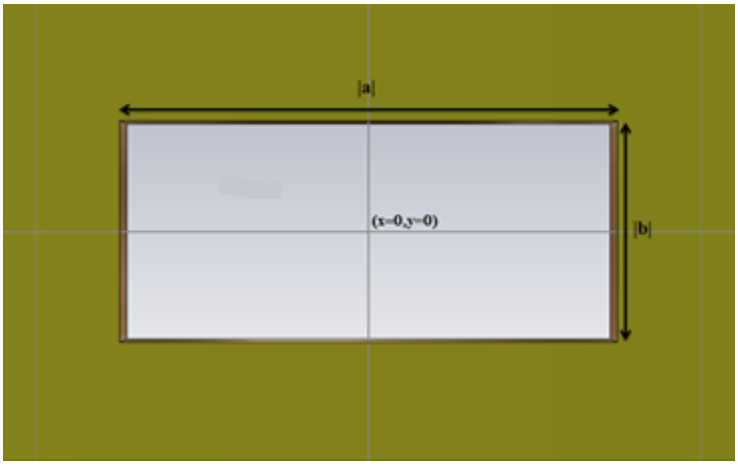

Figure D.4: Transverse (*x*,*y*) plane of a waveguide aperture surrounded by an infinite flange.

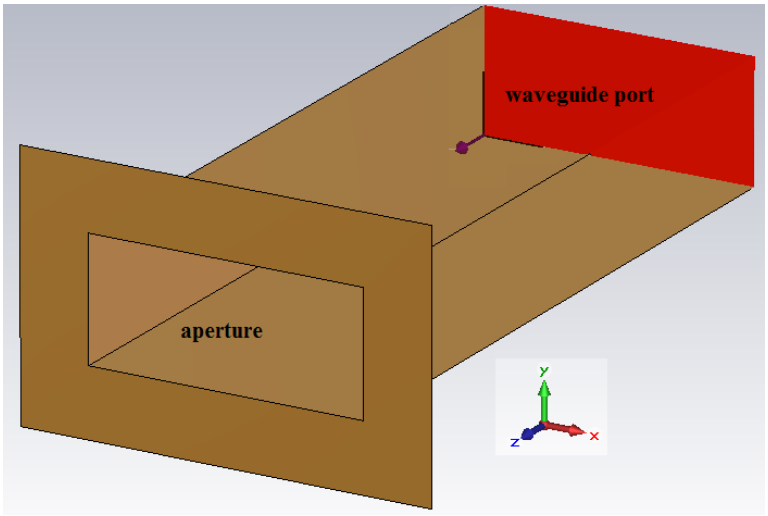

Figure D.5: CST model of the waveguide excited by a matched waveguide port.

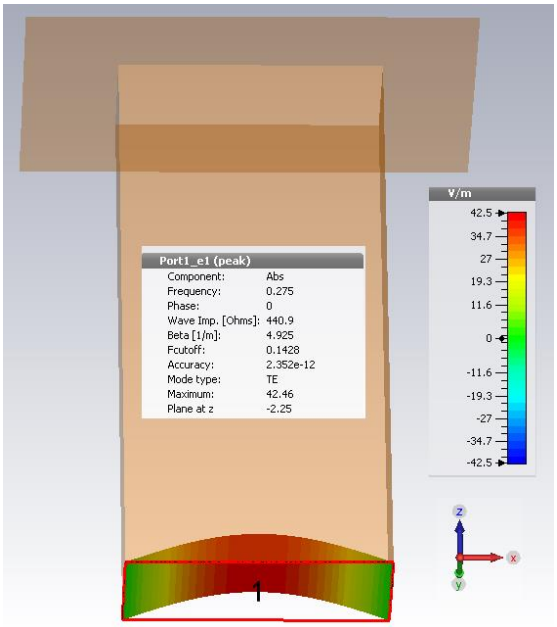

Figure D.6: The cosine TE_{10} mode electric field distribution in the waveguide.

Figure D.6 shows the distribution of the first propagating mode as a cosine distribution across the long dimension of the waveguide aperture and has units of volts/meter (V/m). We expect this mode distribution for the TE_{10} mode [25]. Notice that the mode distribution peaks and is symmetric about $x = 0$ and $y = 0$. The mode distribution does not vary in the z-direction because it is a propagating mode and not an evanescent (attenuating) mode.

D.3.2 *Analysis*

We use a frequency of 300 MHz for the following calculations of the far field radiation pattern. We chose this frequency because it stands equidistant from the f_c that allows the TE_{10} mode to propagate and the first octave that allows multiple modes to propagate. We calculate the far field radiation patterns in the $\underline{\boldsymbol{x}}_o$- and $\underline{\boldsymbol{y}}_o$-directions from equation D.18 as

$$\underline{F}(\theta,\phi) = \underline{\theta}_o\left[\tilde{E}_x\left(k_x,k_y,z=0\right)\cos\phi + \tilde{E}_y\left(k_x,k_y,z=0\right)\sin\phi\right] + \underline{\phi}_o\left(-f_x\sin\phi + f_y\cos\phi\right)\cos\theta \quad \text{(D.21)}$$

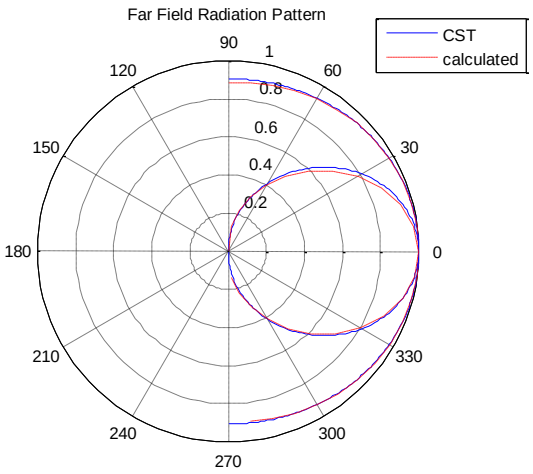

Figure D.7: Polar plot of the normalized far field E_θ and E_ϕ radiation patterns.

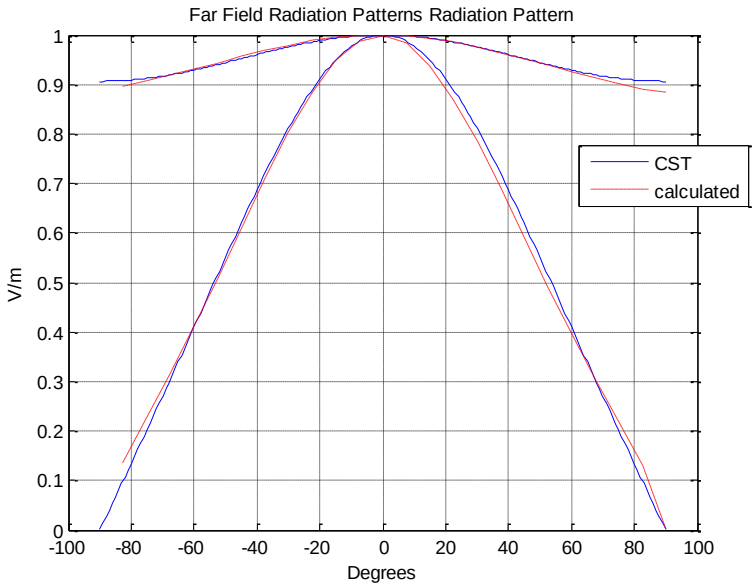

Figure D.8: Linear plot of the normalized far field E_θ and E_ϕ radiation patterns.

Figure D.7 shows the patterns of the far field in the F_θ and F_ϕ directions plotted on a polar graph, whereas figure D.8 shows the patterns of the far field in the F_θ and F_ϕ directions plotted linearly. These plots assume ε_r = 1 and μ_r = 1. We can see from

inspection that the results of solving equation D.18 agree very closely with the results from the simulation using CST Studio Suite 2014.

One thing to note is that when using the SVD method in these computations that the number of singular values used to generate the inverse of the MDM of equation D.18 plays a crucial role. A matrix with dimensions $2L$ x $2L$ will have $2L$ singular values. Many of the singular values will have magnitudes approaching zero. These values should not be used or they will affect the accuracy of the numerical results. On the other hand if you have multiple singular values with useable magnitudes then eliminating any of them from your calculations will also affect the results. Figure D.9 shows a plot of the singular values in descending order for the MDM calculation resulting in the patterns of figure D.7 and figure D.8. The number of singular values we use for this calculation is 4. Generally only the first few singular values are needed.

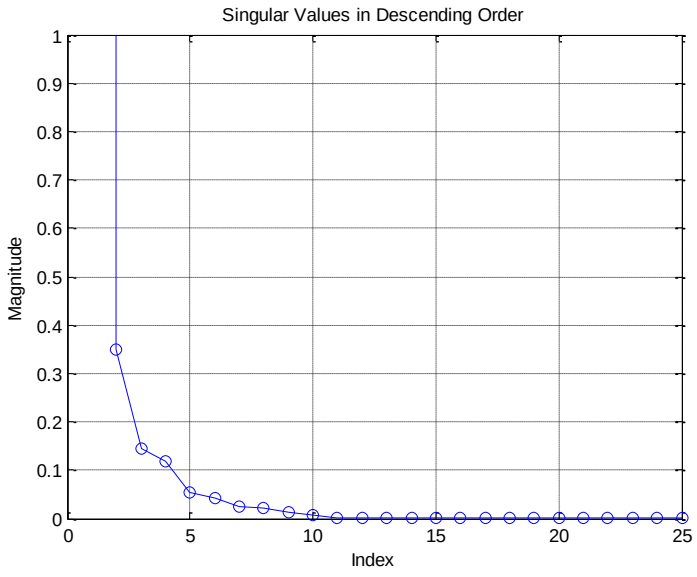

Figure D.9: Plot of the singular values of the MDM in descending order.

Existing methods for analysis of the radiating infinite flange require the computation of the fields at the aperture. We then have to transform these fields to the spectral domain before any far field calculations can be made. This report derives a new approach called the MDM method that allows for the direct computation of the Fourier transform of the electromagnetic fields at the aperture. The result is a matrix equation that directly solves for the spectral components needed for the far field stationary phase approximation. The results of the MDM method were successful compared to the far field radiation patterns of an infinite flange generated with a CST Studio Suite 2014 model.

Appendix E
Description of Simulation Details for CST Models in this Dissertation

This appendix serves to explain some of the finer points of the CST models and simulation parameters used in this dissertation to obtain the results of the various LPA designs. We will highlight various features of the design such as port excitations, mesh cell resolution, and symmetry planes. Since all of our results are based on the results of simulations, we aim to give confidence to the reader that our results reflect real world behavior.

E.1 Port Excitations

First we describe our coaxial port excitations. We model our excitations based on the dimensions of commercial SMA connectors. One typical SMA connector has an inner conductor diameter of 1.27 mm and an outer conductor diameter of 4.25 mm when filled with Teflon. We show a diagram of this coaxial waveguide geometry in figure E.1. We expect this geometry to yield a characteristic impedance of 50 Ω.

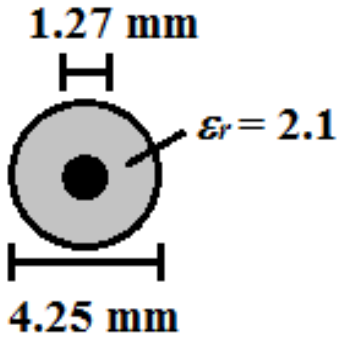

Figure E.1: Geometry of a commercial 50 Ω coaxial line.

We excite our coaxial lines with a waveguide port. In CST Studio Suite, the waveguide port automatically calculates the characteristic impedance and wave impedance of the coaxial line across all simulation frequencies. This ensures accurate

calculation of the fields inside the coaxial line at all simulation frequencies. Figure E.2 shows the field distributions CST calculates for the waveguide geometry depicted in figure E.1.

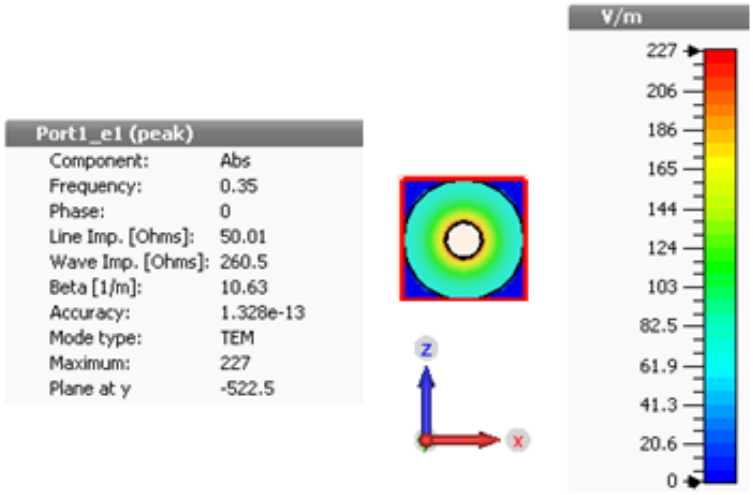

Figure E.2: Field distribution of the TEM mode calculated by the waveguide port in the coaxial line.

The red square boundary represents the bounds of the waveguide port. The inner circle shows the dimensions of the inner conductor. The waveguide port does not calculate fields inside of this volume because we define the conductors as PEC. The scale on the right indicates that the electric field is bound tightly around the inner conductor and dissipates steadily as we move towards the outer conducting wall. The fields beyond the outer conducting wall are identically 0 V/m as we would expect. The list on the left shows that the dominant mode in the coaxial line in the TEM mode and the line impedance is 50.01 Ω. The propagation direction of this geometry is in the $\underline{\boldsymbol{y}}_o$-direction.

E.2 Mesh Cell Resolution and Symmetry Planes

Mesh cell resolution is extremely important in electromagnetic simulations because they define the boundaries of each calculation in the electromagnetic solver. Since the field calculations must be digital, the resolution of the mesh cell defines the accuracy with which the digital calculation will represent the continuous real world result. As such, we define our global mesh for all simulations as $\lambda/20$ at the highest simulation frequency. This is twice the recommended value given by CST. This means the size of the global mesh cell is a twentieth of a wavelength at the highest frequency. Therefore, if we are doing a broadband simulation from 200 MHz to 500 MHz the resolution at the lower frequencies will be even higher than $\lambda/20$ because CST fixes λ at 500 MHz. However, λ is different inside of a high index medium than in free space, but CST utilized an effective λ such that it automatically refines the mesh cell resolution inside of a high index medium versus that of free space.

However, while a global mesh of $\lambda/20$ may be sufficient for electrically large objects, there are some electrically small objects that need an even finer mesh cell resolution. For these objects, CST allows the designer to input a local mesh. This local mesh can be significantly smaller than the global mesh, but limits the application to the dimensions of a single component in the model. Without this feature, to ensure accuracy, we would have to apply the local mesh globally which could potentially greatly increase the simulation time. For example, the dimensions of our coaxial line shown in figure E.1 require a local mesh with higher resolution than our global mesh of $\lambda/20$.

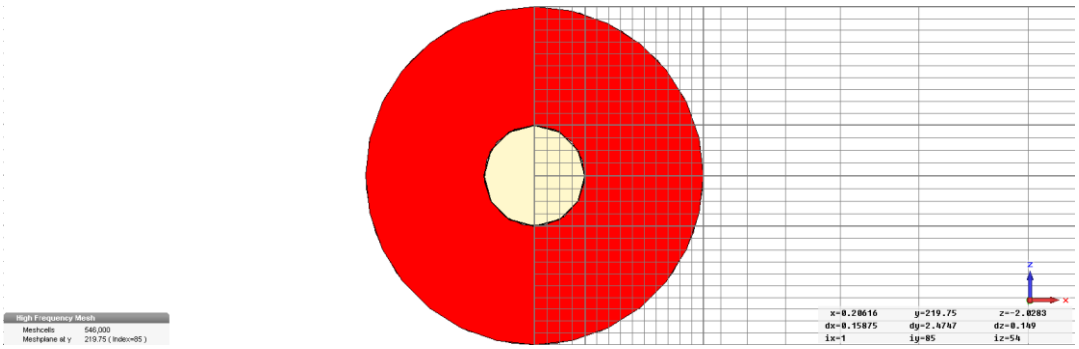

Figure E.3: Mesh cell representation of the transverse (*x*,*y*) plane of the coaxial port geometry.

Figure E.3 shows the local mesh applied to the dimensions of the coaxial line. We define the mesh cell size to be 1/10 the distance between the outer conductor and inner conductor boundaries. We apply this mesh cell resolution across the transverse dimensions of our waveguide port. We know this mesh cell resolution is accurate because of the field distribution we see for the TEM mode in figure E.2, and also by the accuracy of the calculation for the characteristic impedance. This gives an example of how to properly utilize the local mesh feature in CST to yield accurate field results.

Finally, we can define a symmetry plane in the direction of the **E**-field in the cavity to cut the simulation time in half. We are able to do this because our geometric model is perfectly symmetric in the transverse (*x*,*y*) plane. Also, we know from image theory that the image of the electric field vector on one side of a perfect magnetic conductor (PMC) is the mirror image as the electric field vector on the other side. Therefore, defining a PMC boundary at $y = 0$ allows CST to calculate solution for one half of the geometry and then mirror the results for the other side. This essentially cuts solver time down by 50%.

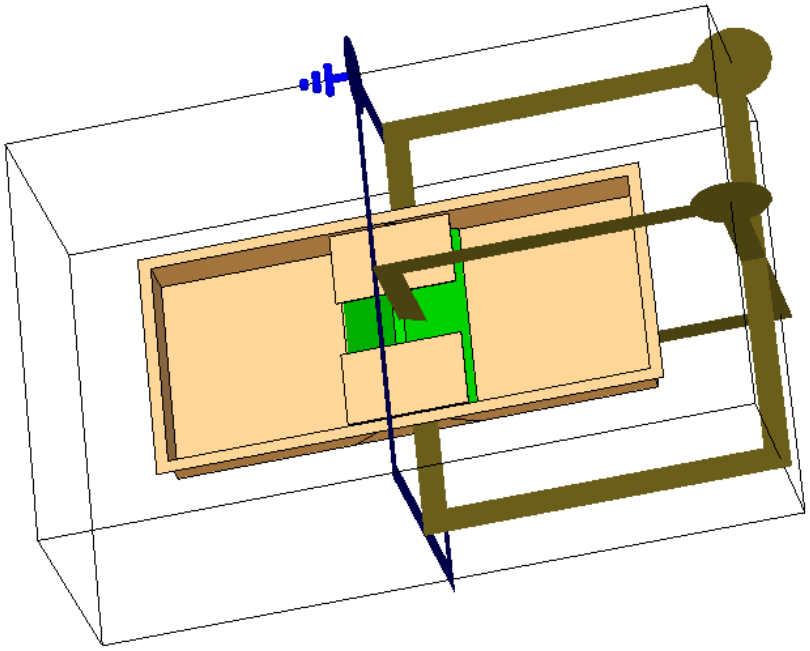

Figure E.4: PMC boundary condition across the symmetric vertical dimension of the LPA model.

Figure E.4 shows the geometry of this artificial PMC boundary condition. The grounded blue boundary signifies the position of the (y,z) plane. The boundaries in the (x,z) and (x,y) planes are grayed out because they have not been activated. We align the PMC boundary along the direction of the E_z in the cavity.